

**ON THE KINETICS
OF STRUCTURAL RELAXATION
IN SOME METALLIC GLASSES**

ON THE KINETICS OF STRUCTURAL RELAXATION IN SOME METALLIC GLASSES

PROEFSCHRIFT

ter verkrijging van de graad van doctor aan
de Technische Universiteit Delft, op gezag van
de Rector Magnificus, Prof. Drs. P.A. Schenck,
in het openbaar te verdedigen
ten overstaan van een commissie
aangewezen door het College van Decanen
op maandag 10 juni 1991 te 16.00 uur

door

Gerhardus Wilhelmus Koebrugge

geboren te Goor
doctorandus in de chemie

Dit proefschrift is goedgekeurd door de promotor
Prof. dr. ir. A. van den Beukel

Dr. ir. J. Sietsma heeft als begeleider in hoge mate bijgedragen aan het
totstandkomen van het proefschrift.

'Morfografisch amorf,' mompelde hij al schrijvend. 'Der fenomeen is niet uit kristallijnen opgebouwd en kan deswegen niet bestaan. Toont echter ener buitenordentelijk accommodatievermogen, dat nader studeerd worden moet...'

'Het leek maar even zo!' riep heer Ollie overspannen op de achtergrond. 'Kijk zelf maar. Het kwam van de schok, heel gewoon!'

Maar de hoogleraar liet zich niet afleiden.

Toen hij klaar was met zijn aantekeningen, greep hij zijn valies en stak een hand uit om Konstantijn te grijpen.

'Ik neem dezer amorfer knaap mede naar mijner laboratorium,' verklaarde hij. 'Daarmede ik hem studeren kan in ener wetenschappelijker omgeving. U zult dat verstaan.'

*Uit: Marten Toonder, De Kon Gruwer
uit de bundel: "Daar kan ik niet tegen"
De Bezige Bij, Amsterdam 1985.*

*voor mijn ouders
voor Anja*

CONTENTS

1	INTRODUCTION	9
	References	13
2	STRUCTURAL RELAXATION IN METALLIC GLASSES	15
2.1	<i>Introduction</i>	15
2.2	<i>The kinetics of structural relaxation</i>	17
2.2.1	Free volume model	17
2.2.2	Activation Energy Spectrum model	20
2.2.3	The mixed model	22
2.3	<i>The CSRO range for $Fe_{40}Ni_{40}B_{20}$</i>	26
2.4	<i>Scope of this thesis</i>	29
	References	30
3	EXPERIMENTAL DETAILS	33
3.1	<i>Materials</i>	33
3.2	<i>Young's modulus measurements</i>	34
3.3	<i>Electrical resistivity measurements</i>	36
3.4	<i>Anelastic strain measurements</i>	41
3.5	<i>Differential Scanning Calorimetry measurements</i>	42
	References	43
4	REVERSIBLE AND IRREVERSIBLE PROCESSES DURING STRUCTURAL RELAXATION	45
4.1	<i>Introduction</i>	45
4.2	<i>Positron lifetime measurements</i>	45
4.2.1	Introduction	45
4.2.2	Experiments	46
4.2.3	Results and discussion	48
4.2.4	Conclusion	51
4.3	<i>Electrical resistivity measurements</i>	51
4.3.1	Introduction	51
4.3.2	Experimental details	52
4.3.3	Results	54

4.3.3.a	As quenched samples	54
4.3.3.b	Cycling experiments	61
4.3.4	Discussion and conclusion	63
4.4	<i>Discussion</i>	66
4.5	<i>Conclusions</i>	68
	References	69
5	DIFFUSION AND FLOW DEFECTS IN AMORPHOUS MATERIALS	71
5.1	<i>Introduction</i>	71
5.2	<i>Results</i>	74
5.2.1	Fe ₄₀ Ni ₄₀ B ₂₀	74
5.2.1.a	Chemical Short Range Ordering	74
5.2.1.b	Stress induced ordering	81
5.2.2	Pd ₄₀ Ni ₄₀ P ₂₀	86
5.2.3	Scaling diffusion coefficient and viscosity	89
5.3	<i>Discussion</i>	92
5.4	<i>Conclusions</i>	95
	References	95
6	STRUCTURAL RELAXATION IN AMORPHOUS Pd₄₀Ni₄₀P₂₀	97
6.1	<i>Introduction</i>	97
6.2	<i>Kinetics of defect annihilation and production</i>	98
6.3	<i>Experimental results</i>	102
6.3.1	As quenched samples	102
6.3.2	DSC experiments	110
6.3.3	Cycling experiments	113
6.3.4	Chemical Short Range Ordering	116
6.4	<i>Discussion</i>	121
6.5	<i>Conclusions</i>	125
	References	125
	SUMMARY	127
	SAMENVATTING	131

CURRICULUM VITAE

135

NAWOORD

136

CHAPTER 1

INTRODUCTION

Metallic glasses or amorphous metals are metallic alloys in the solid state without (translational) long range atomic order. The most widely used technique to produce metallic glasses is rapid quenching from the liquid or gaseous phase. In this rapid solidification process the atoms are frozen in a "liquid-like" structure. The similarity in structure between liquid metals and metallic glasses is shown by broad maxima in the diffraction patterns.

Various preparation techniques have been developed [1]:

- Quenching techniques, like splat quenching, spray deposition and melt spinning.
- Deposition techniques, like sputtering, evaporation, chemical deposition, electrodeposition.
- Irradiation techniques, like ion implantation.
- Diffusion techniques, like solid state amorphisation in multilayers and ball milling.

For the applicability of quenching techniques the composition of the alloys is limited to a smaller range than for the other techniques. However, the amorphous alloys obtained by the quenching techniques have been used more frequently, since this technique produces long filaments, ribbons or tapes [2] instead of the powders and thin (surface) layers produced by the other techniques. Some of the melt spun glasses are commercially available.

The first three forementioned techniques have in common that the thickness of the product hardly ever exceeds 100 μm . This restricts the applications of these materials. It is hoped that one time a bulk amorphous material will be produced by a solid state reaction, *e.g.* diffusion in a compositionally modulated alloy [3]. A completely amorphous NiZr alloy that exceeds the dimensions obtained by the first three production techniques by about a factor 10 has already been produced in this way [4].

With respect to composition metallic glasses can be divided into three classes: the metal-metalloid glasses, the metal-metal glasses and

the glasses based on the group II elements. The alloys of the first class, among which the materials this thesis is dealing with, consist mostly of 75% to 85% transition metal and 25% to 15% metalloid.

Metallic glasses have remarkable magnetic, mechanical, electrical and corrosion properties, directly related to their structure and enhanced by the right choice of composition:

- They are magnetically very soft [5,6].
- They are exceptionally hard, have an extremely high tensile strength, are wear resistance and posses a large fracture toughness [7-10].
- The electrical resistivity of metallic alloys is three to four times higher than that of the crystalline alloys of the same composition [11,12].
- Metallic glasses are exceptionally corrosion resistant [13].

On the other hand, metallic glasses have a relatively low resistance to fatigue under tension [14].

The magnetic properties have been used to produce recording heads, magnetic transducers and transformer cores. The latter application will lead to a reduction of energy losses in transformers. However, due to the high production costs application of metallic glasses is still very limited.

Amorphous materials also have a scientific interest. They present the possibility to study a system that is thermodynamically not in equilibrium. Many groups all over the world do research on this subject, resulting in many papers dealing with preparation techniques, stability, structure and structural relaxation.

The scope of this thesis is to describe processes of structural relaxation. Low temperature annealing of metallic glasses causes changes in a large number of physical properties. This is attributed to atomic rearrangements in the amorphous state and the term structural relaxation is generally used to indicate these processes. Structural relaxation must be clearly distinguished from crystallisation, the phase transition from the amorphous to the crystalline state.

The aim of studying structural relaxation is to obtain information on the kinetics of ordering and the stability of the amorphous material during heat treatments. Since most of the properties of amorphous

materials change during structural relaxation, the utility of the amorphous material depends strongly on the kinetics of structural relaxation at the application temperature.

In general two kinds of processes are involved in structural relaxation [15]. The first introduces changes in the chemical composition of the local surroundings of the atoms. The second is the densification of the metallic glass due to the annealing out of excess free volume.

A general problem in the interpretation of relaxation studies is the insufficient knowledge of the amorphous structure. Due to the absence of long range periodicity the amorphous structure can only be described statistically. There are no unit cells, there is no translational symmetry and the environment of chemically identical atoms will vary. This indicates the difficulty in determining and describing the structure of metallic glasses.

A diffraction experiment with either neutrons or X-rays results in a scattering curve from which the Radial Distribution Function (RDF) can be derived. The procedure to obtain the RDF is meticulously described by Thijsse [16]. The RDF gives the average number of atoms at a distance r from the origin atom. However, the RDF is only a one dimensional projection of the amorphous structure and as yet no direct method has been developed to determine the three dimensional structure from the RDF.

In figure 1.1 typical RDFs from an amorphous sample are given [17]. The height of the peaks decreases with increasing peak number. Characteristic for the amorphous structure is the split second peak. Further a sharp first peak is present, which means that the nearest neighbour distance is rather well defined.

In the literature many RDFs have been reported, which are the starting point for modelling of the amorphous structure. Different strategies have been used to find a model for the amorphous structure:

- Dense random packing of hard spheres (DRPHS), performed by physical models [18] or by computers [19].
- Models based on crystal modifications, like the microcrystalline model [20], disordered packing of structure units like trigonal prisms [21], para-crystals [22] and para-para-crystals [23].
- Molecular dynamics [24].

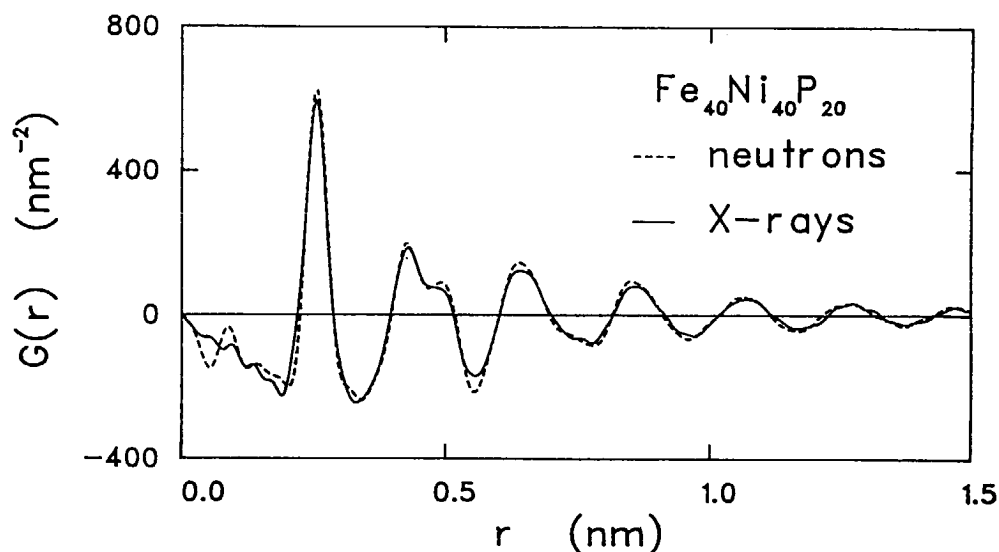


figure 1.1 Radial Distribution Functions for $\text{Fe}_{40}\text{Ni}_{40}\text{P}_{20}$, obtained by neutron and X-ray diffraction [17].

In spite of the limited information on the actual amorphous structure, several models were developed to describe the kinetics of structural relaxation. The main models are the free volume model [25], the activation energy spectrum (AES) model [26], the two level system model [27] and the mixed model [28]. Most of these models will be described in chapter 2.

The kinetics of structural relaxation can be studied by measuring the change of physical properties during annealing. Electrical resistivity, Young's modulus, internal energy and viscosity are very popular physical properties for the study of structural relaxation. Chapter 3 deals with the experimental details for the measurements of some of these properties. The experiments for this thesis were performed in order to further clarify

- reversible and irreversible processes during structural relaxation in amorphous $\text{Fe}_{40}\text{Ni}_{40}\text{B}_{20}$ (chapter 4)
- the dependence of the reversible ordering rate on the amount of free volume (chapter 5), and

- the kinetics of structural relaxation in $\text{Pd}_{40}\text{Ni}_{40}\text{P}_{20}$.

References

- 1 H.H. Liebermann, in Amorphous Metallic Alloys, F.E. Luborsky ed., Butterworths, London, 1983, p. 26.
- 2 H.A. Davies, in Proc. 3rd Int. Conf. on Rapidly Quenched Metals, Brighton, 1978, B. Cantor ed., Metals Society, London, 1978, vol. 1, p. 1.
- 3 R.B. Schwartz and W.L. Johnson, Phys. Rev. Lett. 51, 415 (1983).
- 4 J. Eckert and L. Schultz, Colloque de Phys. C4, 229 (1990).
- 5 T. Masumoto, in Proc. Int. Conf. on Metallic Glasses: Science and Technology, Budapest, 1980, Kultura, Budapest, 1981, vol. 1, p. 121.
- 6 C.D. Graham and T.Egami, Ann. Rev. Mat. Sci., R.A. Huggins, R.H. Bube and R.W. Roberts eds., Annual Reviews Inc., Palo Alto, CA, 8 (1979), 423.
- 7 C.A. Pampillo, J. Mater. Sci. 10, 1194 (1975).
- 8 L.A. Davis in Metallic Glasses, Proc. Sem. on Metallic Glasses, 1976, H.L. Leamy and J.J. Gilman eds., ASM, Ohio, 1978, p. 190.
- 9 T. Masumoto, Sci. Rep. RITU A26, 246 (1977).
- 10 J.C.M. Li, Treatise on Material Science and Technology, H. Herman ed., Academic Press, N.Y., 20, 326 (1981).
- 11 P.J. Cote and L.V. Meisel, in Glassy Metals I, H.-J. Güntherodt and H. Beck eds., Springer, Berlin, 1981, p. 144.
- 12 K.V. Rao, in Amorphous Metallic alloys, F.E. Luborsky ed., Butterworths, London, 1983, p. 401.
- 13 T. Masumoto and K. Hashimoto, in Proc. 3rd Int. Conf. on Rapidly Quenched Metals, Brighton, 1978, B. Cantor ed., Metals Society, London, 1978, vol. 1, p. 435.
- 14 L.A. Davis, J. Mater. Sci. 11, 711 (1976).
- 15 T. Egami, J. Mater. Sci. 13, 2587 (1978).
- 16 B.J. Thijsse, J. Appl. Cryst. 17, 61 (1984).
- 17 J. Sietsma, Ph.D. Thesis, Delft University of Technology, 1987.
- 18 J.D. Bernal, Proc. Roy. Soc. A284, 299 (1964).
- 19 J.L. Finney, Proc. Roy. Soc. A319, 479 (1970).
- 20 J. Dixmier and K. Doi, Compt. Rend. 257, 2451 (1963).
- 21 P.H. Gaskell, J. Non-Cryst. Sol. 32, 207 (1979).

- 22 G. Faigel and E. Svab, in Proc. 5th Int. Conf. on Rapidly Quenched Metals, Würzburg, 1984, S. Steeb and H. Warlimont eds., North-Holland Physics Publishing, Amsterdam 1985, vol. 1, p. 487.
- 23 J. Sietsma and B.J. Thijsse, J. Non-Cryst. Sol. 101, 135 (1988).
- 24 F. Yonezawa, S. Nose and S. Sakamoto, in Proc. 6th Int. Conf. on Liquid and Amorphous Metals, Garmisch-Partenkirchen, 1986, W. Gläser, F. Hensel and E. Lüscher eds., Z. für Phys. Chemie Neue Folge 1, München, 1987, vol. 1, p.77.
- 25 F. Spaepen, Acta Metall. 25, 407 (1977).
- 26 M.R.J. Gibbs, J.E. Evetts and J.A. Leake, J. Mater. Sci. 18, 278 (1983).
- 27 H. Kronmüller and N. Moser, in Proc. 3rd Int. Conf. on the Structure of Non-Crystalline Materials, Ch. Janot and F. Wright eds., Grenoble, 1985 p. 391.
- 28 A. van den Beukel, S. van der Zwaag and A.L. Mulder, Acta Metall. 32, 1895 (1984).

CHAPTER 2

STRUCTURAL RELAXATION IN METALLIC GLASSES

2.1 Introduction

Metallic alloys can be obtained in an amorphous state by rapidly quenching the liquid. Several techniques have been developed to attain a sufficiently high cooling rate [1]. The obtained product has a liquid-like structure and since both production process and structure show resemblance with glass (used for, for instance, in window panes), these materials are called metallic glasses.

During slow cooling, the liquid normally solidifies to the crystalline state at or slightly below the melting temperature T_m . However, during rapid quenching the time at temperatures just below T_m is too short to obtain the crystalline material. The liquid becomes undercooled and will be frozen in as a glass.

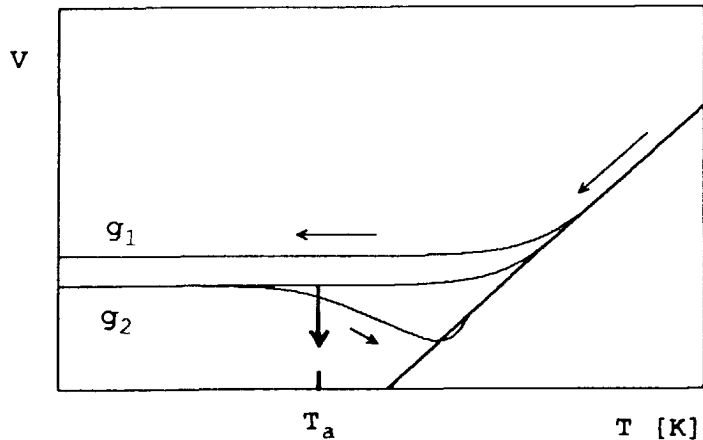


figure 2.1 Schematic behaviour of the specific volume V during rapidly quenching for two cooling rates, resulting in glasses g_1 and g_2 , and thereafter annealing of glass g_2 under isothermal conditions at $T = T_a$ and during linear heating.

The physical properties of the material will change during the glass formation. In figure 2.1 an example is given. In this figure the specific

volume V during cooling is schematically plotted versus temperature. During rapid cooling in the liquid state V decreases linearly with temperature (thick line in figure 2.1). The specific volume of the glass deviates from this undercooled liquid state when the atomic movements become too slow to follow the equilibrium that is changing with temperature. If the cooling rate is lower, the liquid can follow the undercooled liquid line longer. This is demonstrated for two cooling rates in figure 2.1, resulting in two metallic glasses g_1 and g_2 .

Metallic glasses are not in equilibrium. Therefore a metallic glass will always try to reach a more stable configuration. The processes by which the metallic glass relaxes towards the metastable undercooled liquid are called *structural relaxation*. The processes involved are thermally activated, which means that structural relaxation evolves faster at higher temperatures. At room temperature these processes are so slow that the changes during prolonged storing at room temperature are negligibly small for most metallic glasses.

A large number of properties changes during structural relaxation. For instance, the structure densifies during annealing, which is shown in figure 2.1 for both isothermal and isochronal conditions. Isothermal annealing is annealing during a certain time t_a at a fixed temperature T_a . For an as quenched glass this will result in a decrease in volume, as indicated in the figure by the vertical arrow at T_a . Isochronal annealing means that annealing is performed during a fixed time at, generally, increasing temperatures. The solid line in figure 2.1 shows the effect of a special case of isochronal heating, viz. linear heating. The volume decreases with temperature until metastable equilibrium is reached and then increases because the equilibrium volume increases. At a certain moment, when the temperature becomes very high the glass will crystallise, i.e. reach its equilibrium structure. For many glasses this will happen before the metastable equilibrium of the undercooled liquid is reached.

Changes in electrical resistivity [2-5], Young's modulus [6-8], viscosity [9-12], length [13,14], magnetic properties [15,16], mechanical properties [17-19] and internal energy [20-24] have been used frequently to study the kinetics of structural relaxation. Both isothermal and isochronal experiments have been performed. The observed changes in the

physical properties are due to changes in the structure of the amorphous alloy, caused by the structural relaxation processes.

It has been shown several times in the literature that part of the changes in the physical properties of amorphous alloys is irreversible upon temperature changes, while the other part appears to be reversible *i.e.* in a temperature range with sufficient atomic mobility properties can be changed reversibly with temperature [25]. Egami [26] compared the reversible changes to order-disorder phenomena in crystalline materials and called it Chemical Short Range Ordering (CSRO). The irreversible changes were ascribed to the annealing out of excess free volume. This process is called Topological Short Range Ordering (TSRO). Although changes in atomic positions can not unambiguously be detected by direct measurements (like X-ray diffraction or Mössbauer spectrometry), the suggestion that these two processes play a major role in structural relaxation is widely accepted.

2.2 The kinetics of structural relaxation

The description of the relaxation kinetics has been subject of much theoretical debate. A few phenomenological models have been developed and will be discussed in the next sections. First a description of the free volume model will be given, after which the Activation Energy Spectrum (AES) model will be described. Finally, a mixed model of these two will be presented.

2.2.1 Free volume model

The free volume model describes the atomic mobility in terms of the volume available for the atoms [27]. Four assumptions form the basis of this model:

- (1) Around every atom a cell can be defined, of which the volume is given by v . The volume of the cell is determined by the neighbouring atoms. The Wigner-Seitz construction, for instance, can be used to determine this cell.
- (2) If the volume of the cell is larger than a certain amount v_c , $v - v_c$ can be considered as free volume v_f .

- (3) Atomic transport is only possible in the case of the presence of a critical amount of free volume v^* . This volume is on the order of one atomic volume. The area in which this amount of free volume is present is called a *defect*.
- (4) Redistribution of free volume over the atoms takes place without change in free energy.

Cohen and Turnbull [27] calculated the distribution function of the free volume defined by the four points mentioned above. Essential for these calculations is the statistical character of the free volume distribution; no fixed cells with holes of about v^* , like in the Frenkel theory for liquids [28], are assumed. The distribution function $P(v_f)$ for the free volume is given by

$$P(v_f) = \frac{\gamma}{\langle v_f \rangle} \exp \left(-\frac{\gamma v_f}{\langle v_f \rangle} \right), \quad (2.1)$$

where $\langle v_f \rangle$ is the mean free volume and γ is a constant between 0.5 and 1. A defect is found if $v > v^*$, so the probability for a defect is

$$P^*(\langle v_f \rangle) = \int_{v^*}^{\infty} P(v) dv = \exp \left(-\frac{\gamma v^*}{\langle v_f \rangle} \right). \quad (2.2)$$

This probability is called the defect concentration c_f :

$$c_f = \exp \left(-\frac{\gamma v^*}{\langle v_f \rangle} \right). \quad (2.3)$$

This means that $N_{av} \cdot c_f$ is the number of defects per mole atoms, where N_{av} is the Avogadro number.

Already in 1913 Batschinski [29] introduced the concept that the resistance to flow in a liquid should depend on the relative free volume per molecule. In 1951 Doolittle [30] provided satisfactory evidence for this proposal; his measurements disclosed a logarithmic relation between the viscosity η and the mean free volume:

$$\eta = K \exp \left(\frac{L v_m}{\langle v_f \rangle} \right). \quad (2.4)$$

In this equation K and L are constants and v_m is the molecular volume at 0 K. This empirical equation was elucidated by Spaepen [31] who, from a model on stress assisted jumping of atoms into defects, derived that

$$\eta = \frac{kT\Omega}{c_f k_f (\gamma_0 v_0)^2}, \quad (2.5)$$

where k_f is the shear unbiased jump frequency of a defect, γ_0 is the shear strain per jump of a defect, v_0 is the volume a defect and Ω is the atomic volume. In eq. (2.5) the free volume term in eq. (2.4) is represented by c_f .

Viscosity measurements on metallic glasses during structural relaxation have been performed many times [e.g. 9-12]. It was found that the viscosity increases linearly with time during annealing. This means that the annihilation of defects follows second order kinetics:

$$\frac{d\eta}{dt} = \text{Const.} \Rightarrow \frac{dc_f^{-1}}{dt} = k_r \Rightarrow \frac{dc_f}{dt} = -k_r c_f^2, \quad (2.6)$$

where k_r is a rate constant.

Taub and Spaepen [32] suggested that the occurrence of second order kinetics means that the annihilation of defects takes place at special relaxation sites, the concentration of which is proportional to c_f as suggested by Spaepen [31].

Integration of eq. (2.6) results in:

$$c_f^{-1} - c_{f,0}^{-1} = C_0 t \exp\left(-\frac{E_f}{RT}\right), \quad (2.7)$$

with $k_r = C_0 \exp(-E_f/RT)$, E_f the activation energy of defect annihilation, C_0 a constant and $c_{f,0}$ the concentration of defects at $t = 0$. After substituting eq. (2.3) in eq. (2.7), we get

$$\exp(x^{-1}) - \exp(x_0^{-1}) = C_0 t \exp\left(-\frac{E_f}{RT}\right). \quad (2.8)$$

In this latter equation x equals $\langle v_f \rangle / \gamma v^*$, the reduced free volume, and x_0 is the reduced free volume at $t = 0$.

As mentioned previously (eq. (2.5)), the viscosity of metallic glasses is connected to the concentration of defects. For some metallic glasses a saturation of the viscosity was measured during annealing close to the glass transition temperature, indicating that the metallic glass reaches

equilibrium [33]. The equilibrium viscosity, η_{eq} , depends on the annealing temperature as described by the empirically obtained Fulcher-Vogel equation [34,35]:

$$\eta_{eq} = \eta_0 \exp\left(\frac{B}{T-T_0}\right). \quad (2.9)$$

In this equation η_0 , B and T_0 are constants. In view of the free volume model the equilibrium defect concentration $c_{f,eq}$ is then given by

$$c_{f,eq} = \exp\left(-\frac{B}{T-T_0}\right). \quad (2.10)$$

Typical values for B are between 3000 and 7000 K, for T_0 values between 300 and 600 K have been reported [33,36].

Equation (2.7) does not account for an equilibrium concentration $c_{f,eq}$ that differs from zero. In chapter 6 of this thesis the equilibrium will extensively be discussed and adaptations of eq. (2.7), accounting for the approach towards equilibrium, will be introduced.

2.2.2 Activation Energy Spectrum Model

It was realised in the early stages of research on metallic glasses that the temperature and time range of structural relaxation is much too wide to be accounted for by a single thermally activated process. Structural relaxation seems to consist of a series of relaxation processes with a continuous distribution of activation energies. This suggestion forms the basic idea used by Gibbs *et al.* [37] in the development of their Activation Energy Spectrum (AES) model. This theory is based on previous work by Primak [38].

In the AES model a process is considered as a thermally activated rearrangement of atoms or clusters of atoms. The structure is characterised by a short range order parameter, varying locally throughout the specimen. During annealing the local order parameter can reach equilibrium. As the associated activation energy should be related to the local structure, there is a distribution of relaxation processes. If q is the total density of ordering processes available for relaxation, the kinetics obey a general differential equation of the kind

$$\frac{dq}{dt} = -kq^n. \quad (2.11)$$

In this equation n is the order of "reaction", t is the time and k is a rate constant. In general, q cannot be measured directly. If a property $P(t)$ measured during structural relaxation, changes from the value $P(0)$ to $P(\infty)$, and the property change $p(t) = P(\infty) - P(t)$ is proportional to q , eq. (2.11) changes to

$$\frac{dp}{dt} = f \frac{dq}{dt} = -kf \left(\frac{p}{f}\right)^n, \quad (2.12)$$

where f is the change in property accompanying the occurrence of a kinetic process (termed the importance factor). It is usually assumed that the Arrhenius expression can be used for the rate constant k , involving the activation energy E . Then

$$\frac{dp}{dt} = -Af \left(\frac{p}{f}\right)^n \exp\left(-\frac{E}{RT}\right), \quad (2.13)$$

where A is a constant. In the case of isothermal annealing and $n \neq 1$, this equation can be integrated to

$$p(t) = p_0 [1 - (1-n)\nu t \exp\left(-\frac{E}{RT}\right)]^{1/(1-n)}, \quad (2.14)$$

where $p_0 = P(\infty) - P(0)$. The quantity $\nu (=A(f/p_0)^{(1-n)})$ has the dimension of a frequency for all orders of reaction. If, instead of a single activation energy, a spectrum of activation energies must be considered, the change in the measured value of the property $\Delta P(t)$ is the integral of $p(t)$ over the range of activation energies E :

$$\Delta P(t) = \int_0^{\infty} p_0 [1 - (1-n)\nu t \exp\left(-\frac{E}{RT}\right)]^{1/(1-n)} dE \quad (2.15)$$

or

$$\Delta P(t) = \int_0^{\infty} p_0(E) \Theta(E, T, t) dE. \quad (2.16)$$

ΔP is the observed change in the value of the measured property and $\Theta(E, T, t)$ is called the characteristic annealing function.

For first order kinetics ($n=1$), equation (2.11) gives rise to the characteristic annealing function

$$\Theta(E, T, t) = 1 - \exp\{-vt \exp(-\frac{E}{RT})\}. \quad (2.17)$$

The point of inflection of the characteristic annealing function for all n (in a graph of Θ versus E) is termed the characteristic activation energy and is indicated as E_0 . Independent of n , E_0 is given by

$$E_0 = RT \ln(vt). \quad (2.18)$$

Since it was shown by Primak [38] that for $n=1$ $\Theta(E, T, t)$ changes in a small energy range (width $\approx 6RT$) from 0.99 to 0.01, $\Theta(E, T, t)$ can be approximated, if the AES is wide compared to $6RT$, by the step function

$$\begin{aligned} \Theta &= 1 \text{ for } E \leq E_0 \\ \Theta &= 0 \text{ for } E > E_0. \end{aligned}$$

In this approximation $\Theta(E, T, t)$ expresses the fact that, at time t , all ordering processes with $E \leq E_0$ have contributed to the relaxation and have reached the equilibrium value at that temperature.

The measured change in a property P is then given by

$$\Delta P(t) = \int_0^{E_0(t)} p(E, T) dE \quad (2.19)$$

or, if $p(E, T)$ is constant with respect to E , it follows from (2.18) and (2.19) that

$$\Delta P(t) = p_0(T) RT \ln(vt). \quad (2.20)$$

The activation energy spectrum in this case is a box distribution.

2.2.3 The mixed model

In the previous two models no distinction has been made between the kinetics of the two different kinds of processes (CSRO and TSRO). Both the free volume model and the AES model were developed to describe the whole observed effect during structural relaxation. However, these models are insufficient to describe all the experimental data. For instance, the AES model predicts $\log(\text{time})$ kinetics, whereas the

viscosity changes linearly with time. Also, the occurrence of both reversible and irreversible processes is not accounted for.

Van den Beukel and coworkers [39,40] have developed the so called mixed model, in which aspects of both models described before are incorporated. According to them CSRO can be described by the AES model and TSRO by the free volume model with a single activation energy. In the next part more details of this mixed model will be given with the help of some experimental data reported previously [10,40-42].

As explained earlier, in section 2.2.1, the concentration of defects determines the viscosity of the metallic glass. Therefore, the kinetics of defect annihilation can be studied by measuring the change in viscosity during annealing. Van den Beukel *et al.* [10] reported isoconfigurational and isothermal viscosity measurements on $\text{Fe}_{40}\text{Ni}_{40}\text{B}_{20}$. Analysis of the data showed different behaviour in two temperature ranges.

In range I (520 - 600 K) the observed changes of the viscosity could be described consistently in terms of the annealing out of flow defects. The activation energy for the annihilation of flow defects was found to be $E_f = 250$ kJ/mole. The temperature dependence of the viscosity is given by $\eta \propto \exp(Q_\eta/RT)$ with $Q_\eta = 304$ kJ/mole. The reason for the difference between the activation energy for the viscosity Q_η and E_f stems from the temperature dependence of the activation volume $\gamma_0 v_0$ in eq. (2.5), in accordance with the conclusions of Taub and Spaepen [32].

In range II ($T < 520$ K) the isoconfigurational viscosity yields an activation energy of about 250 kJ/mole, close to the value found for the annihilation of flow defects. The initial increase of the viscosity in this range was ascribed to an increase of chemical order.

Fitting the viscosity as a function of time during annealing in range I with eqs. (2.5) and (2.7) yields values for C_0 and x_0 equal to $1.63 \cdot 10^{25} \text{ s}^{-1}$ and 0.079, respectively.

The results of this analysis have been used to describe the isothermal change of several other physical properties like Young's modulus, length and electrical resistivity [13,40-42] in $\text{Fe}_{40}\text{Ni}_{40}\text{B}_{20}$. In figure 2.2 the change in Young's modulus is given for five temperatures. A pulse-echo technique was used to measure the longitudinal wave velocity v , and Young's modulus E is given by $E = \rho v^2$, where ρ is the density. In this

figure changes in E are presented as changes in v^2 , as the corresponding change in ρ was found to be negligible.

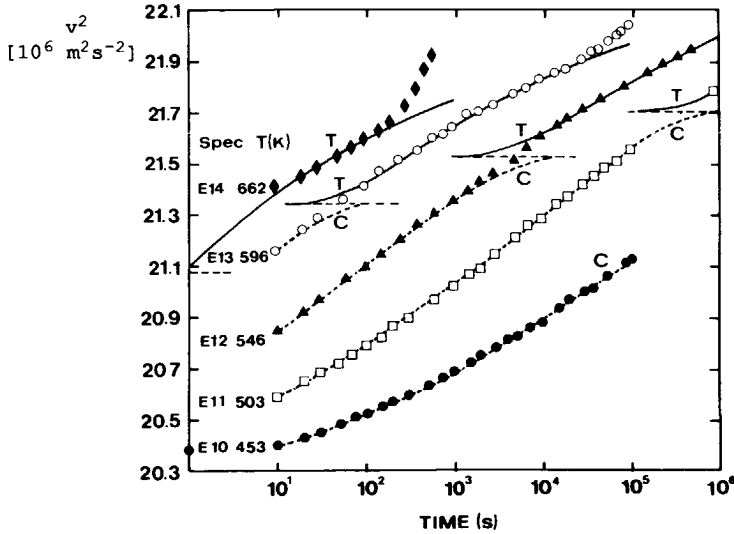


figure 2.2 Isothermal change of v^2 of as quenched $\text{Fe}_{40}\text{Ni}_{40}\text{B}_{20}$ specimens at the temperature indicated. Calculated TSRO and CSRO contributions are indicated by T and C, respectively [13].

The mixed model assumes that the changes in v^2 are due to two kinds of processes. One of them is the annealing out of free volume. It is shown by the solid lines T in figure 2.2 that the final part of the isotherms can be well described by eq. (2.8), assuming a linear dependence between the change in v^2 and the change of free volume:

$$\Delta v^2 = A_E \Delta x. \quad (2.21)$$

A_E is a constant of the value $-24 \cdot 10^6 \text{ m}^2 \text{ s}^{-2}$. The x_0 value resulting from these fits was 0.07527, slightly different from the value found from the viscosity data.

The reason for the assumption of linear behaviour between Δv^2 and Δx and not between Δv^2 and c_f is given by the following. During viscosity measurements it was observed that the viscosity changes linearly with

annealing time. However, in Young's modulus measurements it was observed that v^2 changes about linearly with logarithm of time. It is an essential aspect of the free volume model that it gives a plausible explanation for the different behaviour of these properties.

The remaining part of the isotherms, indicated by the dashed lines C in figure 2.2, is due to the other group of processes, CSRO. According to van den Beukel [40] this can be described by the AES model using a box distribution. The spectrum contains activation energies between 133 and 243 kJ/mole. The highest energy is close to the activation energy E_f for the annealing out of free volume (250 kJ/mole).

The frequency factor v ranges from 10^{12} to 10^{19} s^{-1} . Following Berry [43], van den Beukel [40] suggested a relation between v and E :

$$v = v_0 \exp\left(\frac{\beta E}{R}\right), \quad (2.22)$$

where β and v_0 are constants, $9.7 \cdot 10^{-4} \text{ K}^{-1}$ and $6.6 \cdot 10^6 \text{ s}^{-1}$ for $\text{Fe}_{40}\text{Ni}_{40}\text{B}_{20}$, respectively. Inserting eq. (2.22) in eq. (2.18) we find the relation

$$E_0 = \frac{RT}{(1-\beta T)} \ln(v_0 t). \quad (2.23)$$

The frequency factor v_0 is smaller than the Debye frequency. However, van den Beukel and Radelaar [39] argued that the kinetics of CSRO depends on the amount of free volume. Taking this into account, we obtain

$$v_0 = v_d \exp(-x^{-1}), \quad (2.24)$$

where v_d is expected to be the Debye frequency. The physical meaning of this is the following. Since CSRO must be a diffusion process, the kinetics of this process is controlled by defects. In the free volume model [31], it is assumed that both diffusion and viscous flow are controlled by the same defects, the concentration of which is given by $\exp(-x^{-1})$. If the initial value for x ($= 0.07527$) is inserted in eq. (2.24), v_d equals $4 \cdot 10^{12} \text{ s}^{-1}$, which is indeed close to the Debye frequency.

2.3 The CSRO range for $\text{Fe}_{40}\text{Ni}_{40}\text{B}_{20}$.

The above presented model has been used successfully to describe structural relaxation data for $\text{Fe}_{40}\text{Ni}_{40}\text{B}_{20}$. Electrical resistivity [44] and length measurements [41] were two additional properties to test the mixed model. All experimental data could be described with a single set of parameters for both TSRO and CSRO.

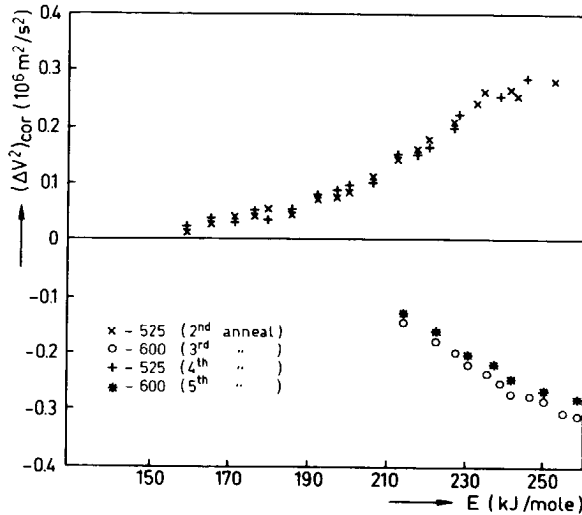


figure 2.3 Change of v^2 upon sequential annealing at the indicated temperatures for an $\text{Fe}_{40}\text{Ni}_{40}\text{B}_{20}$ specimen preannealed at 600 K for 600 seconds [45].

The reversibility of CSRO was tested by cycling experiments [13,45]. A typical result for Young's modulus measurements is given in figure 2.3. In this figure the change in Young's modulus (Δv^2) is plotted versus the activation energy E_0 , calculated with eq. (2.23). After an annealing treatment at 600 K sufficiently long to obtain complete chemical order at this temperature (600 seconds), the temperature has been cycled between 525 K and 600 K, as indicated in the figure. From the change in v^2 the calculated changes due to free volume annihilation have already been subtracted.

The reversibility of the CSRO processes is clear from the isotherms of figure 2.3. For instance, a measurement at 600 K after preannealing at

525 K shows a decrease of v^2 due to disordering, whereas a measurement at 525 K after preannealing at 600 K shows the reverse behaviour.

Huizer *et al.* [41] and Kokmeijer *et al.* [44] have reported a more detailed study of the non-TSRO part of the isotherms. To this end, length measurements and electrical resistivity measurements were performed. Huizer reported a reversible length change during cycling experiments which was smaller than expected from as quenched measurements. This gave rise to the idea that, apart from TSRO and CSRO, a third, irreversible effect occurs.

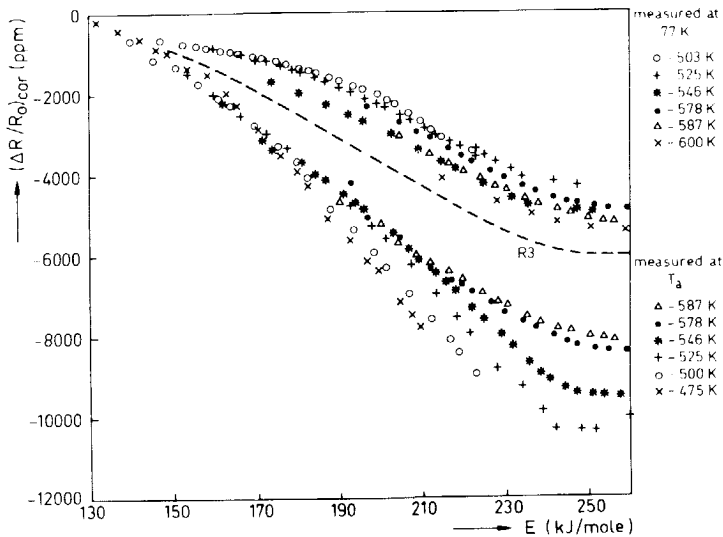


figure 2.4 Change of resistance of as quenched $\text{Fe}_{40}\text{Ni}_{40}\text{B}_{20}$, measured at 77 K and measured at T_a , versus the activation energy. The data have been corrected for the calculated TSRO contribution. E is calculated with equation (2.23) [45].

The existence of a third effect was confirmed by electrical resistivity measurements [44]. Kokmeijer *et al.* reported the change in electrical resistivity during annealing at temperatures T_a , measured at both the annealing temperature itself and in liquid nitrogen. Both as quenched and cycling experiments were performed. In figure 2.4 the as quenched isotherms are presented. The change in electrical resistivity

due to the annealing out of free volume has been subtracted from the measured change in electrical resistivity, assuming a linear relation between the electrical resistivity and Δx . Therefore all isotherms saturate to an equilibrium value near 250 kJ/mole.

In figure 2.4 all isotherms, measured at both measuring temperatures, continuously decrease. It is also shown that for the measurements performed at T_a the equilibrium value becomes more negative for lower annealing temperatures. The measurements performed in liquid nitrogen also show a continuous decrease, but the equilibrium value seems to become less negative for lower T_a .

Cycling experiments also show a different behaviour for the two measuring temperatures. The measurements performed at the annealing temperature show the behaviour as expected from the as quenched experiments: ordering gave rise to a decrease of the electrical resistivity, where disordering results in an increase.

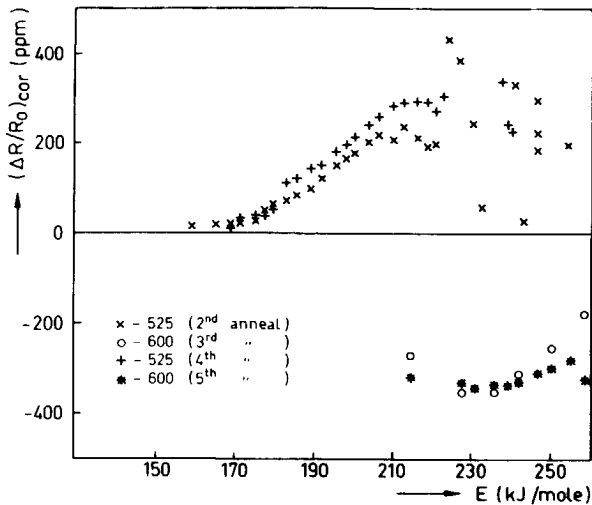


figure 2.5 Change of resistance for an $\text{Fe}_{40}\text{Ni}_{40}\text{B}_{20}$ specimen identically heat treated as in figure 2.3. The change in resistance is measured at 77 K [45].

In figure 2.5 the change in electrical resistivity as measured in liquid nitrogen is plotted versus the time during cycling experiments. The annealing treatments were identical to that of figure 2.3. After

preannealing at 600 K, the temperature was cycled between 525 K and 600 K. The effect due to the annealing out of free volume was subtracted from the experimental data.

In these measurements ordering gives rise to an increase in electrical resistivity and disordering results in a decrease. The combined data could only be explained by a third effect, which is irreversible and results in a decrease of the electrical resistivity. Huizer [45] assumed further that this third effect is measuring temperature independent and that the kinetics can be described by the AES model. Under these assumptions the dashed line in figure 2.4, indicated with R3, represents the irreversible change in electrical resistivity. Huizer finally concluded that the initial part of the activation energy spectrum behaves irreversibly, because no reversible effect was observed where, according to the as quenched isotherms, reversible effects should have been observed. This irreversible effect can also be the cause for the unexpectedly small reversible length changes [41].

2.4 Scope of this thesis

In the previous sections the usefulness of the mixed model has been demonstrated with the help of some experimental data. The data on structural relaxation in amorphous $\text{Fe}_{40}\text{Ni}_{40}\text{B}_{20}$ can consistently be described with the mixed model. However, there still remain some questions which need to be investigated. In this section a few of these matters, which are topics of this thesis, will be formulated.

The introduction of irreversible processes during the non-TSRO part is, as yet, unexplained and need to be investigated further.

In all experimental data presented previously, no clear transition between CSRO and TSRO has been observed, since the changes due to both processes have the same sign in the observed physical properties. The separation in a CSRO and TSRO component can only be performed in an indirect way. The mixed model will become more credible if for one physical property a clear transition between CSRO and TSRO is observed.

It is expected that changes in the local surroundings of an atom occurs by diffusion. In crystalline solids ordering takes place by means of atomic jumps into vacancies and the relaxation time of ordering is proportional to c_v^{-1} , where c_v is the concentration of vacancies. This

means that when quenched-in vacancies anneal out, the relaxation time of ordering increases. If there are similarities between the ordering processes in crystalline and in amorphous solids, one can expect that free volume has an effect on the relaxation time for CSRO. It seems obvious to put the relaxation time for CSRO in amorphous materials proportional to c_f^{-1} , the concentration of flow defects. This proportionality should be tested experimentally.

Finally, the mixed model has been mainly applied on structural relaxation data for amorphous $\text{Fe}_{40}\text{Ni}_{40}\text{B}_{20}$. The mixed model has to be tested for other metallic glasses to provide a strong support for the generality of this model.

References

- 1 H.H. Liebermann, in *Amorphous Metallic Alloys*, F.E. Luborsky ed., Butterworths, London, 1983, p. 26.
- 2 M. Barricco, G. Riontino, P. Allia and F. Vinai, in *Proc. 6th Int. Conf. on Rapidly Quenched Metals*, Montreal, 1987, R.W. Cochrane and J.O. Ström-Olsen eds., *Mat. Sci. Eng.* **97**, 537 (1988).
- 3 M. Balanzat, *Scripta Metall.* **14**, 1245 (1980).
- 4 J.R. Cost and J.T. Stanley, *Scripta Metall.* **15**, 407 (1981).
- 5 E. Balanzat, J.T. Stanley, C. Mairy and J. Hillairet, *Acta Metall.* **33**, 785 (1985).
- 6 A.L. Mulder, S. van der Zwaag and A. van den Beukel, in *Proc. 5th Int. Conf. on Liquid and Amorphous Metals*, Los Angeles, 1983, C.N.J. Wagner and W.L. Johnson eds., *J. Non-Cryst. Sol.* **61&62**, 979 (1984).
- 7 E. Huizer and A. van den Beukel, in *Proc. 3th. Int. Conf. on the Structure of Non-Crystalline Materials*, Grenoble, 1985, Ch. Janot and A.F. Wright eds., *J. de Phys. Coll.* **C8**, 561 (1985).
- 8 H.G. Scott and A. Kursumovic, *Metal Sci.* **15**, 583 (1981).
- 9 S.S. Tsao and F. Spaepen, *Acta Metall.* **33**, 881 (1985).
- 10 A. van den Beukel, E. Huizer, A.L. Mulder and S. van der Zwaag, *Acta Metall.* **34**, 483 (1986).
- 11 A.R. Bhatti and B. Cantor, in *Proc. 6th Int. Conf. on Rapidly Quenched Metals*, Montreal, 1987, R.W. Cochrane and J.O. Ström-Olsen eds., *Mat. Sci. Eng.* **97**, 479 (1988).

- 12 A. Bouali and C. Tete, in in Proc. 6th Int. Conf. on Rapidly Quenched Metals, Montreal, 1987, R.W. Cochrane and J.O. Ström-Olsen eds., Mat. Sci. Eng. 97, 493 (1988).
- 13 A. van den Beukel, S. van der Zwaag and A.L. Mulder, Acta Metall. 32, 1895 (1984).
- 14 H.R. Sinning, L. Leonardson and R.W. Cahn, Int. J. Rapid Solidification, 1, 175 (1985).
- 15 Ch. Cunat, H.R. Hilzinger and G. Herzer, in Proc. 6th Int. Conf. on Rapidly Quenched Metals, Montreal, 1987, R.W. Cochrane and J.O. Ström-Olsen eds., Mat. Sci. Eng. 97, 497 (1988).
- 16 T. Egami and T. Jagielinski, in Proc. 5th Int. Conf. on Rapidly Quenched Metals, Würzburg, 1984, S. Steeb and H. Warlimont eds., North-Holland Physics Publishing, Amsterdam, 1985, vol.1, p. 667.
- 17 J. Piller and P. Haasen, Acta Metall. 30, 1 (1982).
- 18 R. Gerling, F.P. Schimansky and R. Wagner, Scripta Metall. 17, 203 (1983).
- 19 D. Deng and A.S. Argon, in Proc. 5th Int. Conf. on Rapidly Quenched Metals, Würzburg, 1984, S. Steeb and H. Warlimont eds., North-Holland Physics Publishing, Amsterdam, 1985, vol.1, p. 771.
- 20 M.G. Scott, Scripta Metall. 15, 1073 (1981).
- 21 J.W. Drijver, A.L. Mulder and S. Radelaar, in Proc. 4th Int. Conf. on Rapidly Quenched Metals, Sendai, 1981, T. Masumoto and K. Suzuki eds., Japan Inst. Met., Sendai, 1982, vol.1, p. 535.
- 22 I. Majewska-Glabus and B.J. Thijsse, in Proc. 5th Int. Conf. on Rapidly Quenched Metals, Würzburg, 1984, S. Steeb and H. Warlimont eds., North-Holland Physics Publishing, Amsterdam, 1985, vol.1, p. 635.
- 23 Z. Althounian, in Proc. 6th Int. Conf. on Rapidly Quenched Metals, Montreal, 1987, R.W. Cochrane and J.O. Ström-Olsen eds., Mat. Sci. Eng. 97, 461 (1988).
- 24 Ch. Görlitz and H. Ruppertsberg, in Proc. 5th Int. Conf. on Rapidly Quenched Metals, Würzburg, 1984, S. Steeb and H. Warlimont eds., North-Holland Physics Publishing, Amsterdam, 1985, vol.1, p. 631.
- 25 M.R.J. Gibbs, in in Proc. 5th Int. Conf. on Rapidly Quenched Metals, Würzburg, 1984, S. Steeb and H. Warlimont eds., North-Holland Physics Publishing, Amsterdam, 1985, vol.1, p. 643.
- 26 T. Egami, J. Mater. Sci. 13, 2587 (1978).
- 27 M.H. Cohen and D. Turnbull, J. Chem. Phys. 31, 1164 (1959).

- 28 J. Frenkel, Kinetic theory of liquids, Clarendon Press, Oxford, 1946
- 29 A. Batschinski, Z. Phys. Chem. 84, 644 (1913).
- 30 A. Doolittle, J. Appl. Phys. 22, 1471 (1951).
- 31 F. Spaepen, Physics of Defects, in Les Houches Lectures XXXV, J.P. Poirier and M. Klemm eds., North Holland, Amsterdam 1981, p. 136.
- 32 A.I. Taub and F. Spaepen, Acta Metall. 28, 1781 (1980).
- 33 C.A. Volkert and F. Spaepen, in Proc. 6th Int. Conf. on Rapidly Quenched Metals, Montreal, 1987, R.W. Cochrane and J.O. Ström-Olsen eds., Mat. Sci. Eng. 97, 449 (1988).
- 34 G. Fulcher, J. Amer. Ceram. Soc. 6, 339 (1925).
- 35 H. Vogel, Z. Phys. 22, 645 (1921).
- 36 P.A. Duine, J. Sietsma and A. van den Beukel, in Proc. 7th Int. Conf. on Rapidly Quenched Materials, Stockholm, 1990, in press.
- 37 M.R.J. Gibbs, J.E. Evetts and J.A. Leake, J. Mater. Sci. 18, 278 (1983).
- 38 W. Primak, Phys. Rev. 100, 1677 (1955).
- 39 A. van den Beukel and S. Radelaar, Acta Metall. 31, 419 (1983).
- 40 A. van den Beukel, J. Non-Cryst. Sol. 83, 134 (1986).
- 41 E. Huizer and A van den Beukel, Acta Metall. 35, 2843 (1987).
- 42 E. Huizer, J. Melissant and A van den Beukel, in Proc. 6th Int. Conf. on Liquid and Amorphous Metals, Garmisch Partenkirchen, 1983, W. Gläser, F. Hensel and E. Lüscher eds., Z. für Phys. Chem. (neue Folge), 1 (1988) vol 2 p. 335.
- 43 B.S. Berry, Scripta Metall. 16, 1407 (1982).
- 44 E. Kokmeijer, E. Huizer, B.J. Thijsse and A. van den Beukel, Phys. Stat. Sol. (a), 105, 235 (1988).
- 45 E. Huizer, Ph.D. Thesis, Delft University of Technology, Delft, 1987.

CHAPTER 3

EXPERIMENTAL DETAILS

3.1 Materials

All materials used for the experiments in this thesis were amorphized by the rapid quenching technique of melt spinning. A schematic representation of the set-up for this quenching technique is given in figure 3.1. A molten alloy is ejected on a fastly rotating copper wheel, which cools down the liquid alloy very rapidly. A typical quenching rate for this technique is 10^5 K/s. The result of this cooling technique is a thin ribbon (30-60 μm) with a dull (the wheel side) and a shiny side.

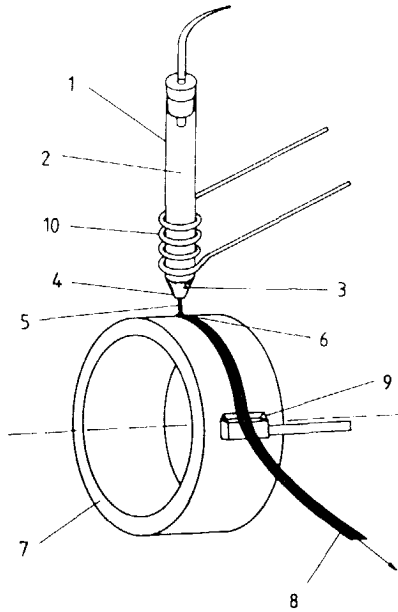


figure 3.1 Schematic drawing of the melt spinning set-up.

1 quartz tube	2 pressure gas
3/5 molten alloy	4 tube opening
6 puddle	7 fastly rotating wheel
8 ribbon	9 scraper
10 high frequency coil	

The alloys for which the results are presented in this thesis, are $\text{Fe}_{40}\text{Ni}_{40}\text{B}_{20}$ and $\text{Pd}_{40}\text{Ni}_{40}\text{P}_{20}$. The first glass has been produced by Vacuumschmelze and is known by the name Vitrovac 0040. The reproducibility of this glass is good: no remarkable differences in the properties of several batches have been found. The second glass has been produced in our own laboratory. In vacuum small sheets of Pd (Highways, 99.9%) have been dissolved in molten Ni_2P (Alpha products, 99.9%). After several remelts to homogenize the alloy, 10 g was used to produce a ribbon with a length of approximately 15 m. In the obtained product no crystalline phase could be detected by X-ray diffraction.

3.2 Young's modulus

Changes in Young's modulus E were measured by measuring changes in the longitudinal wave velocity v with the pulse-echo technique. The modulus is related to v as $E = \rho v^2$, where ρ is the density. Since changes in ρ were expected to be relatively small [1], changes in E will be presented as changes in v^2 . The technique and the set-up have been extensively described in the references [2-5]. In this section a brief description will be given.

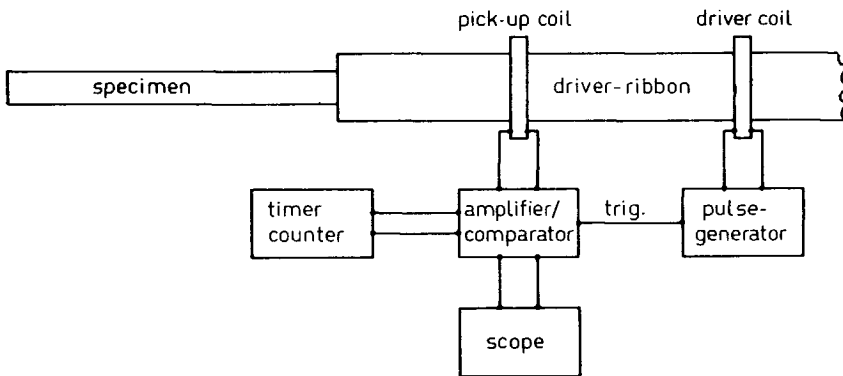


figure 3.2 Schematic drawing of the set-up for the pulse-echo technique used for measuring the longitudinal wave velocity.

A schematic representation of the set-up is shown in figure 3.2. A specimen with a length of about 100 mm and a width of about 1 mm is

spot-welded onto a strongly magnetostrictive ribbon. For this ribbon, the driver ribbon, $\text{Fe}_{40}\text{Ni}_{40}\text{B}_{20}$ (Vitrovac 0040) was used. A longitudinal wave is generated in the driver ribbon with a pulsed magnetic field. The driver coil used to generate the wave is powered by a Philips PM5770 pulse generator. The duration of the pulse is 3 μs and the repetition time is 10 ms.

At 120 mm from the driver coil a second, similar coil is placed. This pick-up coil is used to detect the passing wave by induction through an inverse magnetostrictive effect. The induction of this pick-up coil was enhanced by keeping the driver ribbon partially magnetised by a small permanent magnet.

The principle of the measurements is simple. Being introduced by the driver coil, the wave travels in both directions through the ribbon. The wave of interest travels towards the junction between the specimen and the driver ribbon, passing the pick-up coil for the first time and inducing a first pulse. At the junction the wave is partially reflected which induces a second pulse in the pick-up coil. The part of the wave which travels through the specimen will, after reflection at the end of the specimen, induce a third pulse in the pick-up coil. The wave velocity in the specimen can be obtained by measuring the time difference Δt between the second and third pulse and the length ℓ of the specimen:

$$v = 2\ell/\Delta t. \quad (3.1)$$

The induced wave that travels in the opposite direction (to the right in figure 3.2) will be reflected at the free end of the driver ribbon. The length of the ribbon is such that the reflected wave does not disturb the measurements.

In order to measure the time interval Δt , the signal from the pick-up coil is fed to a fast amplifier and comparator. The comparator is synchronised with the pulse generator, preventing triggering on the first pulse. The output signal of the comparator starts and stops a Hewlett Packard 5308A 75 MHz timer/counter at the positive slope of resp. the second and third peak.

In order to avoid disturbances of magnetic origin (like domain wall motion), the specimen was kept in a saturating magnetic field during the measurements. The measurements were performed at room temperature.

The time interval Δt is of the order of 50 μs and is obtained with an accuracy of $\pm 0.01 \mu\text{s}$ for $\text{Fe}_{40}\text{Ni}_{40}\text{B}_{20}$ and $\pm 0.02 \mu\text{s}$ for $\text{Pd}_{40}\text{Ni}_{40}\text{P}_{20}$. The length of the specimen is on the order of 100 mm with an accuracy of 0.5 mm. The non-systematic error in Δv^2 is $\pm 0.01 \cdot 10^6 \text{ m}^2\text{s}^{-2}$ for both $\text{Fe}_{40}\text{Ni}_{40}\text{B}_{20}$ and $\text{Pd}_{40}\text{Ni}_{40}\text{P}_{20}$. The mean as quenched values for v^2 are $(20.20 \pm 0.14) \cdot 10^6 \text{ m}^2\text{s}^{-2}$ and $(10.10 \pm 0.09) \cdot 10^6 \text{ m}^2\text{s}^{-2}$ for $\text{Fe}_{40}\text{Ni}_{40}\text{B}_{20}$ and $\text{Pd}_{40}\text{Ni}_{40}\text{P}_{20}$, respectively. Between different isotherms systematic deviations of 0.5% can occur due to the accuracy of the length measurements.

The specimens are annealed under flowing helium gas in a tube furnace. Because of the easy specimen access to this furnace, fast specimen handling is possible and the annealing treatments are well defined. The warming up period of the specimen was only a few seconds and so was the cooling down time to room temperature after extracting the specimen from the furnace. When the periods of annealing between two measurements are taken much larger than 1 second, the interruption of the isothermal annealing caused by the measuring procedure will have negligible consequences.

3.3 Electrical resistivity measurements

Electrical resistivity measurements were performed by measuring the change of electrical resistance during annealing. Since changes in ρ were expected to be relatively small [1], changes in the electrical resistance were mainly determined by changes in electrical resistivity.

In figure 3.3 a schematic drawing of the set-up is given. The most important parts of this set-up are the furnace (13), the measuring rod (15) and the guidance tube (1) and the specimen holder (8).

The furnace consists of two plates of aluminium, in which pipes of alumina are mounted, containing thermocoax heating wire. The specimen can be placed between the aluminium plates from below. The furnace is controlled by a Rex C1000 temperature controller and a chromel/alumel thermocouple.

The measuring rod and the guidance tube allow vertical transport of the specimen. Therefore it is possible to measure the change in electrical resistance at different conditions, for instance in liquid nitrogen. It also offers the possibility to remove the specimen from the furnace during

temperature changes. The time to bring the sample at the annealing temperature is determined to be about 7 seconds.

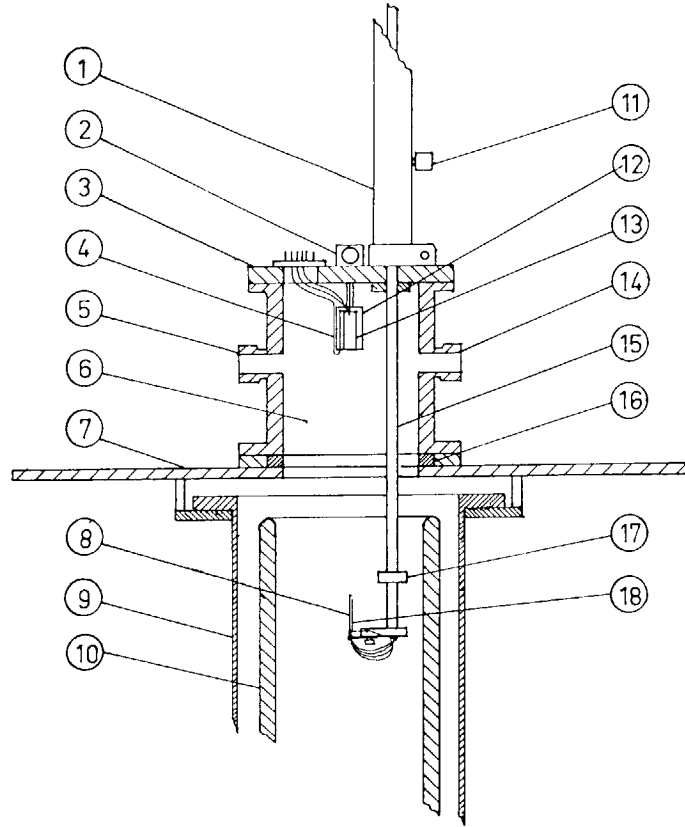


figure 3.3 Drawing of the set-up for the electrical resistivity measurements. For details see text.

The specimen is mounted horizontally on the specimen holder, which is shown schematically in figure 3.4, by butt welding onto the points A. Two platina wires are butt welded between points B and D and act as the potential wires in the resistivity measurements. The points D are joined to copper wires which connect the specimen with the Thomson bridge. Near the specimen a chromel/alumel thermocouple is mounted to monitor the temperature during the measurements.

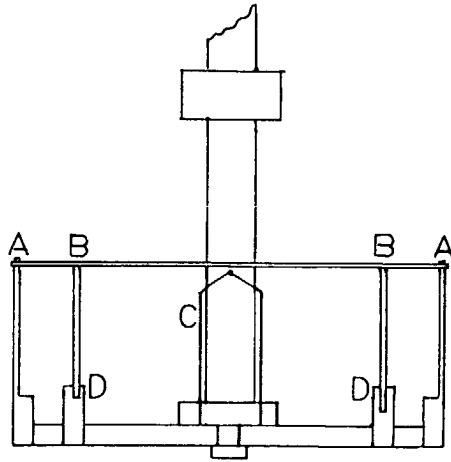


figure 3.4 Detailed drawing of the specimen holder
 A-A specimen
 C thermocouple
 A,B,D butt welds.

The electrical resistance is measured with a computer controlled AC Thomson (Kelvin) bridge. The AC method has been chosen because thermal electromotive forces are canceled. The main advantage of a Thomson bridge is that influences of the wires are in principle compensated. A frequency of 280 Hz is used to suppress the influence of the 50 Hz power line. A complete description of the bridge is given in ref. [6].

The bridge diagram is shown in figure 3.5. In this figure R_1 and R_2 are adjustable resistances, R_3 and R_4 are resistances of 100 Ω , C and C' are adjustable capacitors, R_p is the sample, R_r is a reference resistance (1 Ω) and R_s is a resistance. An isolating transformer is used to separate the current supply from the bridge. All resistances and capacitors, with the exception of R_p , are placed in a box at a constant temperature of 308 K.

The current is supplied by the internal oscillator of the lock-in amplifier (U). The electrical potential between X and Y is transferred to the lock-in amplifier (M), which amplifies only the part of the signal

with the same frequency as the supplied current. Before a measurement the bridge is balanced. Changes in R_p during annealing cause changes in the potential between X and Y. This potential can therefore be used to monitor R_p . The capacitors are used to balance the imaginary part of the electrical resistance.

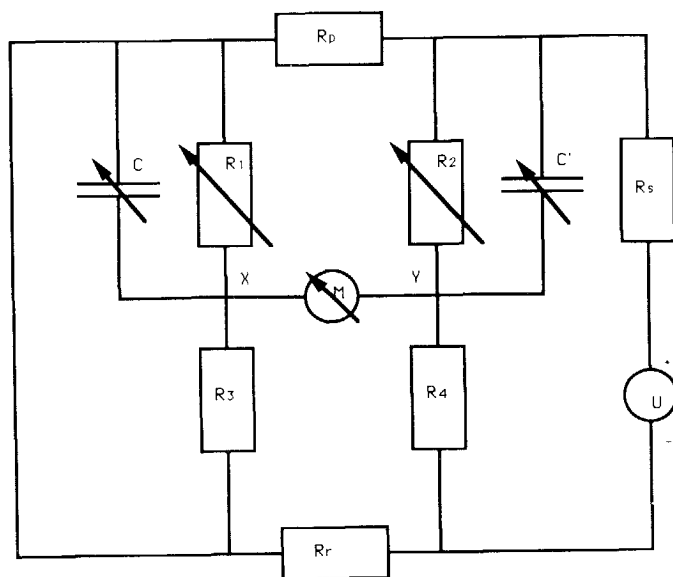


figure 3.5 Block diagram of the Thomson bridge. For details see text.

The measurements are controlled by a DEC Professional computer working under the operating system UNIX. The interfacing between the computer and the set-up is supplied by a PEP microprocessor which allows data collection in a buffer. The computer programs controlling the measurements are developed in the programming language C. Listings of these programs are given in ref. [6].

The accuracy of the observed change of the electrical resistance is partly determined by the corrections for temperature fluctuations (± 0.5 K). The temperature coefficient (390 ± 10 ppm/K for $\text{Fe}_{40}\text{Ni}_{40}\text{B}_{20}$) is obtained for temperatures between room temperature and 473 K and must

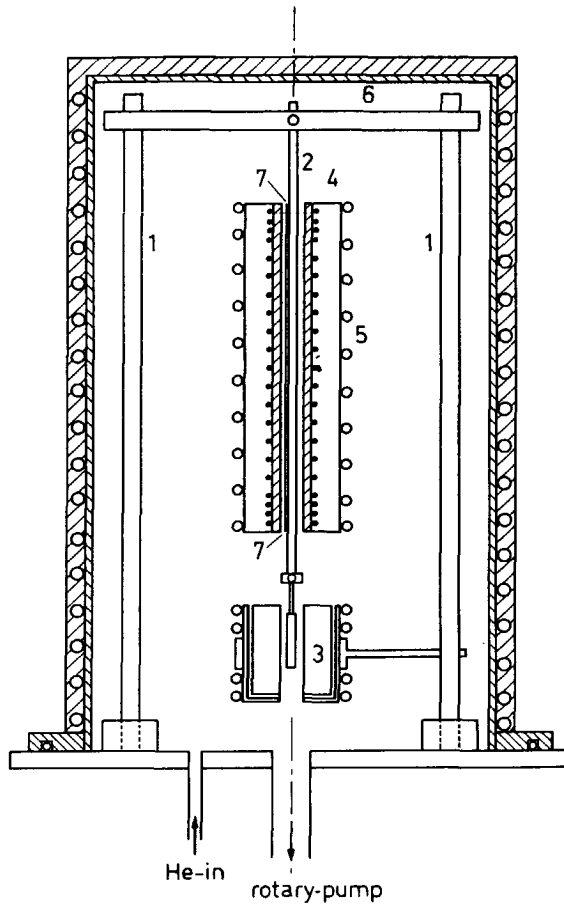


figure 3.6 Schematic drawing of the length measurement set-up.

- 1 quartz rods
- 2 specimen
- 3 LVDT
- 4 furnace
- 5 water cooled heat shield
- 6 bell-jar
- 7 thermocouple.

be extrapolated to the annealing temperatures, typically between 500 and 600 K. The estimated inaccuracy in the data due to temperature fluctuations amounts to 25 ppm. The inaccuracy of resistances used in the bridge and wiring also causes an inaccuracy of 25 ppm. Therefore an

approximation for the inaccuracy in resistivity changes is 50 ppm. It should be mentioned that the absolute value of the resistivity cannot be determined with such a small inaccuracy, but in our investigations only the *changes* matter.

3.4 Anelastic strain measurements

Anelastic strain measurements were performed with the apparatus that was previously used for viscosity and length measurements [7,8]. The apparatus is presented schematically in figure 3.6.

The specimen, with a length of approximately 300 mm, is placed at the centre of the apparatus, attached at the upper end to the aluminium traverse between two vertical quartz rods. Quartz is used for the vertical rods because of its small temperature coefficient of expansion. At the lower end of the specimen the core of a Linear Variable Displacement Transducer (LVDT, Hewlett Packard type 6 DCDT 100) is attached. The coil of the LVDT is fixed onto one of the quartz rods. The temperature in the coil is kept constant by a water cooled housing.

Part of the specimen is surrounded by a vertical furnace. It consists of a copper pipe on which spirally wound thermocoax cable is soldered. The density of the turns increases at both ends of the furnace, compensating for heat losses. The furnace is surrounded by a vertical water-cooled cylinder which acts as a heat shield for the quartz rods. The temperature in the furnace is homogenised by a number of "heat leaks". These leaks establish thermal contact between the furnace and the water cooled tube, transporting heat from the furnace to the tube. Consequently a homogeneous (within 1 K) temperature profile is obtained over a length of about 180 mm and a sharp drop in temperature over about 30 mm at both ends of the furnace (≥ 1.5 K/mm). The length of the specimen that is actually annealed at the given temperature is not exactly known. In the calculations of the relative length changes $\Delta \ell / \ell_0$ a value of $\ell_0 = 200$ mm is used. This introduces an inaccuracy in the absolute value of the strain ϵ . However, this was not important because only *changes* in strain were considered. The absolute scale does not play a role in the interpretation of the data.

The set-up is covered by an insulated water cooled bell-jar filled with He. Since the temperature profile depends very much on the helium pressure inside the bell-jar, the He pressure is kept constant, at 16 Pa.

The temperature is measured with a chromel/alumel thermocouple, mounted inside the furnace, near the specimen. The temperature in the furnace is controlled by a West 2071 P.I.D. temperature controller which keeps the temperature within ± 0.5 K from the set point. During heating the furnace from room temperature, after 15 minutes the temperature is within 2 K from the set point and the overshoot is at most 4 K. With the help of a cooling water circuit the temperature outside the furnace is kept at 308 K.

The LVDT signal is measured with two Keithley 195A multifunction meters, one for the ingoing and one for the outcoming potential. The ratio of these two values is calibrated to changes in length. Length changes as small as 1.10^{-2} mm can be detected yielding an accuracy of 50 ppm.

The measurements are computer controlled by an IBM PC equipped with a IEEE interfacing card. It monitors the temperature and the ingoing and outcoming signal of the LVDT at regular time intervals. In order to check for irregularities inside the bell-jar during the time consuming measurements, the computer displays graphically the length changes versus the annealing time.

The anelastic strain measurements were performed by stress cycling. Stresses can be applied to the specimen by placing weights on the core holder, which is especially constructed for this purpose. More details on this specific type of length measurements will be given in chapter 5.

3.5 Differential Scanning Calorimetry measurements

Differential Scanning Calorimetry was performed with a DSC-2 and a DSC-7 Delta as supplied by Perkin Elmer. A DSC registrates the difference in heat flow from or to two identical sample holders, one containing the sample and the other a reference. The holders are heated electrically and kept at the same temperature. The temperature can either be changed linearly in time at rates between 0.31 K/min and 320 K/min or kept constant.

The samples used in the DSC experiments were small, often not more than 20 mg. In the experiments described in this thesis the crystalline form of the amorphous alloy was always used as a reference, because it is expected that the amorphous and crystalline alloy have nearly the same specific heat c_p , resulting in a nearly constant baseline at $dH/dt=0$.

If processes occur in the sample which consume or produce heat (endo- or exothermic processes) the heat flow to the sample holder must be changed to keep the temperature equal to that of the reference holder. The consumed or produced heat is equal to the change in internal energy of the sample.

References

- 1 R. Gerling, F.P. Schimansky and R. Wagner, *Acta Metall.* 35, 1001 (1987).
- 2 G.J. Curtis, in *Ultrasonic Testing*, ed. J. Szilard, Wiley & Sons, 1982, p. 579.
- 3 J.F.W. Bell, *Phil. Mag.* 2, 1113 (1957).
- 4 H.G. Scott and A. Kursumovic, *Metal Sci.* 15, 583 (1981).
- 5 S. van der Zwaag, A.L. Mulder and J.A. Snijders, Internal Report, Lab. of Metallurgy, Delft University of Technology, 1984.
- 6 H. van der Zee, Internal report, Lab. of Metallurgy, Delft University of Technology, 1987.
- 7 A. van den Beukel, E. Huizer, A.L. Mulder and S. van der Zwaag, *Acta Metall.* 34, 483 (1986).
- 8 E. Huizer and A. van den Beukel, *Acta Metall.* 35, 2843 (1987).

CHAPTER 4

REVERSIBLE AND IRREVERSIBLE PROCESSES DURING
STRUCTURAL RELAXATION4.1 *Introduction*

In chapter 2 a review of data interpretation in terms of the mixed model was given. It was found that the experimental data on structural relaxation in amorphous $\text{Fe}_{40}\text{Ni}_{40}\text{B}_{20}$ can be successfully described in terms of Chemical Short Range Ordering (CSRO) and Topological Short Range Ordering (TSRO) with respectively the Activation Energy Spectrum (AES) model and the free volume model. Nevertheless, in the observed changes of physical properties the transition from CSRO to TSRO was never directly visible; it only appeared after data interpretation.

In order to test the validity of the model, positron lifetime measurements and electrical resistivity measurements were performed. The positron lifetime measurements were used to check the CSRO-TSRO transition point, the electrical resistivity measurements were used to study the CSRO part of the isotherms in more detail.

4.2 *Positron lifetime measurements*4.2.1 *Introduction*

Positron lifetime measurements in amorphous metals have been the subject of a number of papers [1-11]. In most experiments that have been reported on the change in lifetime τ during structural relaxation (2-3 ps) and crystallisation (about 7 ps), isochronal annealing was applied. In general the accuracy was about 0.5-1 ps. Both negative and positive changes in τ during structural relaxation have been reported.

In previously reported sets of data on different properties of amorphous $\text{Fe}_{40}\text{Ni}_{40}\text{B}_{20}$ the separation between CSRO and TSRO was not visible because the sign of the changes in the observed property was the same for the two processes. In search of a directly visible transition from CSRO to TSRO, a positron annihilation study was started, measuring the change in the positron lifetime τ after annealing treatments. It was

expected that during TSRO the lifetime would decrease due to an increase of the density, analogous to the observed decrease of τ in crystalline material when excess vacancies anneal out [12]. The sign of CSRO could not be predicted but if the lifetime would increase due to CSRO, a maximum would be observed at the CSRO-TSRO transition point.

In this chapter positron lifetime measurements after isothermal annealing treatments of the metallic glass $\text{Fe}_{40}\text{Ni}_{40}\text{B}_{20}$ will be presented. The same glass (Vitrovac 0040) was used in previously reported studies of changes of physical properties during structural relaxation. The data are analysed in terms of the mixed model as presented in chapter 2.

This work was done in cooperation with dr. ir. J. de Vries of the Interfaculty Reactor Institute Delft.

4.2.2 Experiments

The positron annihilation technique is a nuclear method used in solid state physics and materials science. Positron lifetime is, beside angular correlation and Doppler broadening, one of the three techniques used to investigate the annihilation characteristics. The positron lifetime depends on the electron density in the sample. An increase of the chance that a positron meets an electron decreases the positron lifetime. The lifetime is obtained by measuring the difference in time between the detection of a photon with an energy of 1275 keV, emitted at the moment the positron is "born" in a ^{22}Na source, and the detection of one of the two photons of 511 keV, emitted at the moment the positron is annihilated. For a general overview of the positron lifetime technique and details about the equipment, see references [11,13,14].

In order to obtain samples of the necessary thickness of about 0.1 mm, four small pieces of the amorphous material were spot welded upon each other. The samples were annealed during a time t_a (between 100 and 10^5 seconds) at a temperature T_a (475 - 600 K). For each $\tau(T_a, t_a)$ a different sample had to be used. The samples were positioned with the dull side of the ribbon to the source.

Two different spectrometers and source constructions were used during the measurements. The first measurements (525 K, 575 K, 600 K and most of the 550 K measurements) were performed with a positron lifetime spectrometer with a resolution of 195 ps FWHM and a $^{22}\text{NaCl}$ -on-mylar source. The 475 K series and the remaining points of the 550 K

series were measured with a spectrometer with a resolution of 150 ps FWHM [13] and a $^{22}\text{NaCl}$ -on-kapton source. The kapton source was used because it was nearly twice as thick as mylar and it was hoped to be mechanically stronger.

The spectra were analysed with the computer program POSITRONFIT [15]. This program considers the obtained spectra (an example is given in figure 4.1) to be the result of at most three lifetime intensity functions convoluted with the resolution function, which was assumed to be gaussian. The contribution of a lifetime τ_i in this spectrum, represented by the intensity I_i , is given by the function $I_i = I_{0,i} \exp(-t/\tau_i)$, where $I_{0,i}$ is a constant. The fit parameters for the program are the intensities and the lifetimes.

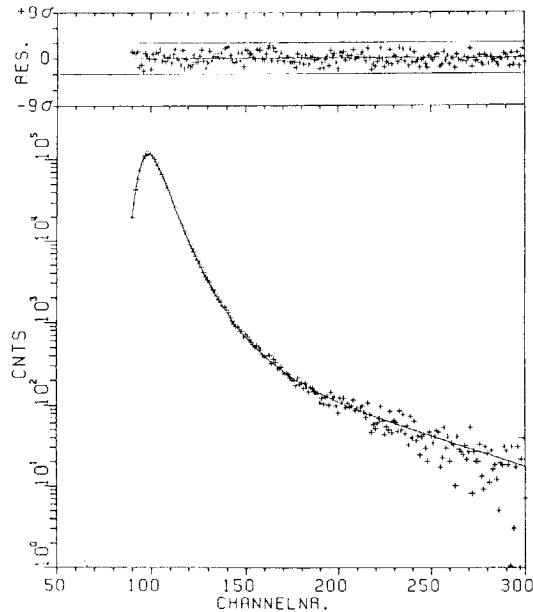


figure 4.1 A typical positron lifetime spectrum of $\text{Fe}_{40}\text{Ni}_{40}\text{B}_{20}$ metallic glasses. The drawn line in the figure is the result of a fit. The residual plot of the fit is given in the upper part of the figure. The time scale is proportional to the channel number (1 channel = 20 ps) and $t=0$ is at channel 100.

Both mylar and NaCl exhibit positron lifetimes in the region of 350 ps and 1.4 ns. To minimize the influence of the source lifetime components, the ratio of the intensities of these two components was obtained from fits of all measured spectra, in which all parameters were free to vary. In the final fits this ratio and the values of the source lifetimes were kept constant, reducing the free fit parameters to the intensities for $\tau = 1.4$ ns and for the sample lifetime, and the sample lifetime itself.

For the measurements performed with the $^{22}\text{NaCl}$ -on-kapton source such a procedure could not be used. Kapton exhibits a single lifetime component of about 380 ps and therefore the intensity of the 1.4 ns lifetime is only representing NaCl and has a very low value. Consequently, the intensities of both the source and sample lifetimes had to be fitted, which was possible because of the good resolution of the spectrometer.

In figure 4.1 a typical spectrum is given. The horizontal axis is given in channel numbers, which are proportional to time. The solid line in this figure is the result of a fit. In the upper part of figure 4.1 the differences between the data points and the fit are given on a linear scale, based on the standard deviation σ . Since the spectrum is obtained by counting γ -photons, σ is equal to the square root of the number of counts. All data points fall within 3σ from the fit and no systematic differences are present.

During these measurements the stability of the source was monitored by measuring an 'as quenched' sample before each measurement of an annealed specimen. Due to the variations in the measuring and analysis procedure (caused by the different sources) variations of a few ps were found between the two series of measurements. To compensate for this the as quenched values were fixed to a value of 147.2 ps, being the average of all as quenched lifetimes, and the points measured in different series were corrected correspondingly. The variation of the lifetime in the as quenched sample was found to be ± 0.6 ps.

4.2.3 Results and discussion

In figure 4.2 the positron lifetime τ is plotted versus the annealing time for five different annealing temperatures. Each point in this figure was obtained by annealing a specimen during the time and at the temperature indicated in the figure. The estimated error in the positron

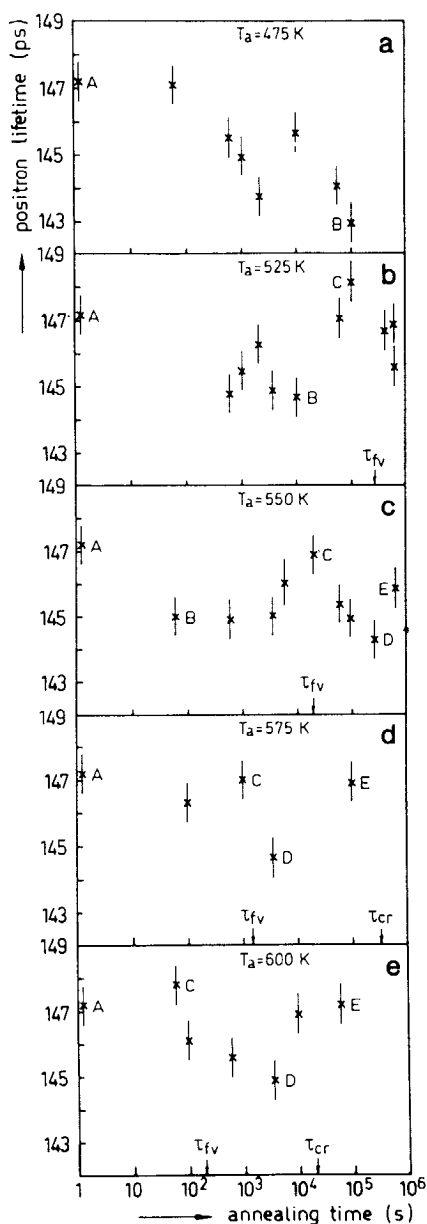


figure 4.2 Positron lifetime in Fe₄₀Ni₄₀B₂₀ as a function of the annealing time at several annealing temperatures. The characters in the figure indicate corresponding points in the different isotherms.

lifetime (± 0.6 ps) is represented in the figure by an error bar in each point. The as quenched value is marked by A at $t_a=1$ second.

The changes in τ are too small for a quantitative interpretation, but qualitatively the following interpretation can be given.

In all figures, on the time axis the time τ_{fv} is indicated. This is the time at which, according to previous analysis of structural relaxation in amorphous $\text{Fe}_{40}\text{Ni}_{40}\text{B}_{20}$ (chapter 2), TSRO becomes important. In all isotherms τ_{fv} corresponds with the onset of a decrease in positron lifetime (part CD in the figure). This means that the preceding part of the τ isothermals (ABC) covers the range previously identified as the CSRO range. It consists of two parts, a decrease (AB) and an increase (BC) of τ . This is in contrast with most previous measurements on the change of other physical properties, where the change was monotonous in the whole CSRO range.

Finally, before τ_{cr} , the time of the onset of crystallisation [16], the positron lifetime increases again, shown by part DE. This somewhat unexpected result has been observed earlier by Tanigawa *et al.* [3] and was ascribed by them to positron trapping at the surface of the small crystalline nuclei. Due to this trapping the lifetime of the positrons increases. With the growth of the nuclei the relative importance of the crystalline bulk increases, and τ consequently decreases. This means that after part DE a new maximum should be observed. This was found by Schiltz *et al.* [5] in $\text{Fe}_{40}\text{Ni}_{40}\text{B}_{20}$ during isochronal annealing. They found a maximum before a strong decrease in lifetime (about 7 ps) due to crystallisation. This maximum is not visible in our experiments because the annealing time was too short to reach it.

The increase of positron lifetime in part DE of the isotherms consistently starts before $t_a = \tau_{cr}$ which means that the onset of crystallisation can be observed earlier by positron lifetime than, for instance, by electrical resistivity, DSC or Young's modulus measurements [17]. This is not unreasonable because in case of the latter, the volume of the crystallites is determining, whereas for positron trapping also the surface plays an important role.

It is clearly shown in figure 4.2 that the whole pattern shifts to shorter times when the temperature increases. At 475 K only the AB and at 600 K only the CDE part of the isotherm can be observed. The most complete picture is the one at 550 K (figure 4.2.c).

The observed change of the positron lifetime can be compared with isochronal data reported in the literature [3,5]. The presented results are

similar to those of Tanigawa *et al.* [3] in $\text{Pd}_{80}\text{Si}_{20}$, where also the CSRO-TSRO subdivision could be made. The only difference was found in part AB, which was constant for PdSi, where in our data a decrease in τ was observed. The data of Schiltz *et al.* [5] on $\text{Fe}_{40}\text{Ni}_{40}\text{B}_{20}$ also show similarities with the present data, although they show less detail than our data. On the other hand, a continuous increase of lifetime for the region ABC in various metallic glasses has been reported by Chen and Chuang [4]. It seems therefore, that changes in positron lifetime are very sensitive to changes in composition.

4.2.4 Conclusion

The present isothermal data of the change of positron lifetime during structural relaxation can directly be compared with results obtained by other techniques on the same glass. This comparison the identification of the annealing out of free volume (TSRO).

The onset of crystallisation is observed earlier by positron lifetime than with other techniques, probably due to an enhanced positron lifetime at the surface of the small crystalline nuclei.

In the regime ascribed to chemical short range ordering (CSRO) a minimum in the lifetime was observed. In the following sections (4.3 and 4.4) the CSRO range will be discussed in more detail with the help of electrical resistivity measurements.

4.3 Electrical resistivity measurements

4.3.1 Introduction

Electrical resistivity measurements have frequently been used to study structural relaxation in amorphous materials [18-26]. Balanzat *et al.* [23] presented a comprehensive study of electrical resistivity for many metallic glasses. They measured the change of electrical resistivity during isochronal annealing, quenching down after the annealing treatment ($T=T_a$) to 4.2 K (liquid helium). For nearly all the as quenched samples an increase of the electrical resistivity was found at low T_a , followed by a decrease at higher T_a .

On the other hand, many studies have been presented, in which the electrical resistivity continuously decreases in both isothermal and

isochronal experiments [24,25]. In these cases the resistivity was measured at the annealing temperature. This suggests, in comparison with the measurements presented by Balanzat *et al.*, that the change of the electrical resistivity during structural relaxation depends strongly on the measuring temperature.

In this study electrical resistivity measurements are presented on $\text{Fe}_{40}\text{Ni}_{40}\text{B}_{20}$, performed at 77 K (liquid nitrogen), 293 K (room temperature) and between 500 and 600 K (annealing temperature). Especially the CSRO part of the isotherms is considered in order to find a confirmation for the existence of two processes in this part of the isotherms as was indicated by the positron annihilation measurements. Preliminary measurements have been reported by Kokmeyer *et al.* [26].

4.3.2 Experimental details

The electrical resistivity measurements were performed with the set-up described in chapter 3. After each annealing treatment the sample was quenched into liquid nitrogen, and the electrical resistance was monitored during 5 minutes. Then the sample was held at room temperature to measure the electrical resistance at that temperature (also during 5 minutes).

The relative change of the electrical resistance during a given annealing treatment was calculated by

$$\frac{\Delta R}{R_N} = \frac{R(t, T_m) - R(0, T_m)}{R_N}, \quad (4.1)$$

where $R(t, T_m)$ is the electrical resistance after an annealing treatment during a time t , measured at the measuring temperature T_m (77 K, room temperature or annealing temperature) and R_N is the electrical resistance of an as quenched sample, measured at 77 K. The division by R_N was performed in order to correct for geometrical differences between different samples.

The value $R(0, T_m)$ at the annealing temperature was obtained by measuring the electrical resistance at $T_1=313$ K and then calculating $R(0, T_m)$ at the annealing temperature by applying the equation

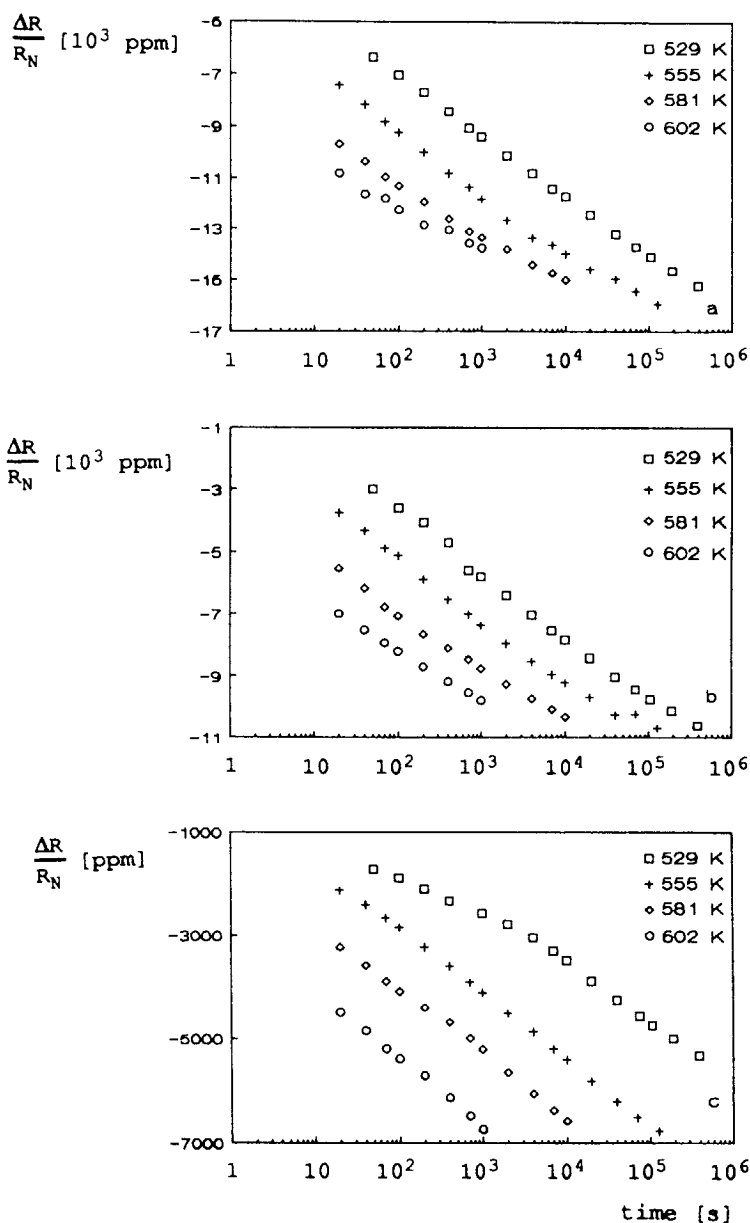


figure 4.3

Isothermal change of the electrical resistivity during annealing at the temperature indicated versus the annealing time, measured at (a) the annealing temperature, (b) room temperature and (c) 77 K.

$$\frac{R(0, T_m)}{R(0, T_1)} = \frac{1 + a(T_m - T_0) + b(T_m - T_0)^2}{1 + a(T_1 - T_0) + b(T_1 - T_0)^2} \quad (4.2)$$

where a and b are the temperature coefficients of the quadratic equation (resp. $3.814 \cdot 10^{-4} \text{ K}^{-1}$ and $1.113 \cdot 10^{-7} \text{ K}^{-2}$) and $T_0 = 273 \text{ K}$. The coefficients were obtained by measuring the resistance between room temperature and 473 K for one sample.

4.3.3 Results

4.3.3.a As quenched samples

In figure 4.3 the change of the electrical resistivity $\Delta R/R_N$, measured at resp. annealing temperature (figure 4.3.a), room temperature (figure 4.3.b) and in liquid nitrogen (figure 4.3.c), is plotted versus time. The isotherms are corrected for small fluctuations in the temperature, as monitored by the chromel/alumel thermocouple. The isotherms measured at room temperature and in liquid nitrogen are also corrected for small differences in the mean measuring temperature between the isotherms. Both observed fluctuations are $\pm 0.5 \text{ K}$.

In figure 4.3 a continuous decrease of the electrical resistivity can be observed for all isotherms. The change of the electrical resistivity is caused, according to the mixed model, by both CSRO and TSRO. No transition point between CSRO and TSRO can be observed, which is in accordance with earlier presented electrical resistivity measurements in liquid nitrogen and at the annealing temperature [26]. However, in some isotherms a small bend can be observed where TSRO becomes important (at 100, 500 and 5500 seconds at resp. 602, 581 and 555 K).

The changes due to TSRO can be obtained by plotting the observed change in electrical resistivity versus the calculated change of the reduced free volume x , where x is given by

$$\exp(x^{-1}) - \exp(x_0^{-1}) = C_0 \exp(-E_f/RT), \quad (2.8)$$

as presented in chapter 2. In this equation $x_0 = 0.07527$, $C_0 = 1.63 \cdot 10^{25} \text{ s}^{-1}$ and $E_f = 250 \text{ kJ/mole}$. The change of the electrical resistivity due to TSRO is taken proportional to Δx , according to Woldt *et al.* [20].

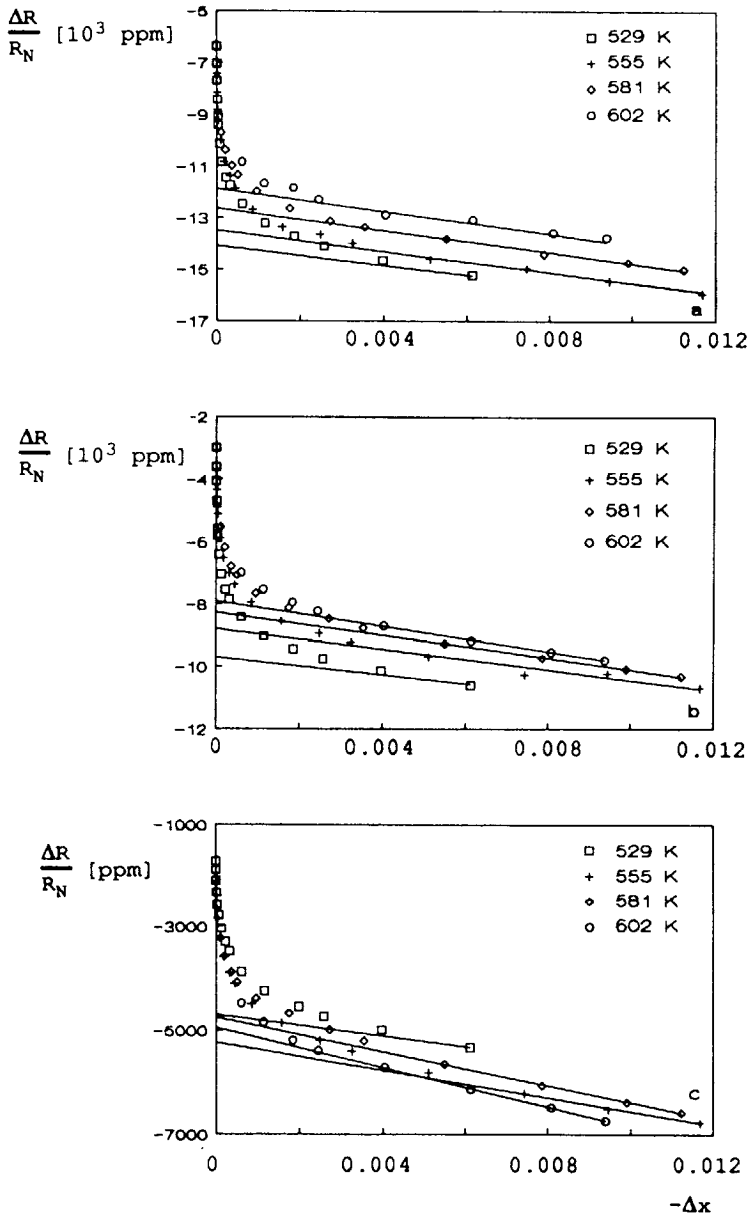


figure 4.4 The isotherms of figure 4.3, now plotted versus the calculated change in reduced free volume $-\Delta x$. The measuring temperatures are (a) annealing temperature, (b) room temperature and (c) 77 K.

TABLE 4.1

Slope (A_R) and intercept $(\Delta R/R_N)_{eq}$ of the straight lines in figure 4.4. T_m and T_a are resp. the measuring and annealing temperature.

T_m [K]	T_a [K]	A_R	$(\frac{\Delta R}{R_N})_{eq}$ [ppm]
529	529	0.189	-14100
555	555	0.204	-13500
581	581	0.216	-12600
602	602	0.222	-11700
293	529	0.143	-9700
	555	0.165	-8800
	581	0.184	-8300
	602	0.203	-7900
77	529	0.101	-4700
	555	0.133	-5200
	581	0.164	-4800
	602	0.191	-4900

In figure 4.4 the change of the electrical resistivity is plotted versus the calculated Δx . It is shown that in all isotherms $\Delta R/R_N$ is linear with Δx for $-\Delta x > 0.004$. This is in agreement with earlier results on Young's modulus measurements [27]. The solid lines in figure 4.4 are results of linear regression fits. In table 4.1 the slopes A_R are given. The intersection of these lines with the $\Delta x=0$ axis yields the value of $\Delta R/R_N$ due to CSRO only, which will be called $(\Delta R/R_N)_{eq}$.

For $T_a = 529$ K it was not possible to determine A_R in the way described before, because at the end of the experiment TSRO has only just started. However, at constant T_m (77 and 293 K) the obtained A_R values show an increase with increasing T_a for $T_a = 555, 581$ and 602 K. As demonstrated in figure 4.5, the $A_R(T_a)$ relation at constant T_m is linear for both $T_m = 77$ K and 293 K. Therefore A_R at 529 K was determined from extrapolation of the straight lines in figure 4.5. The results are represented in table 4.1.

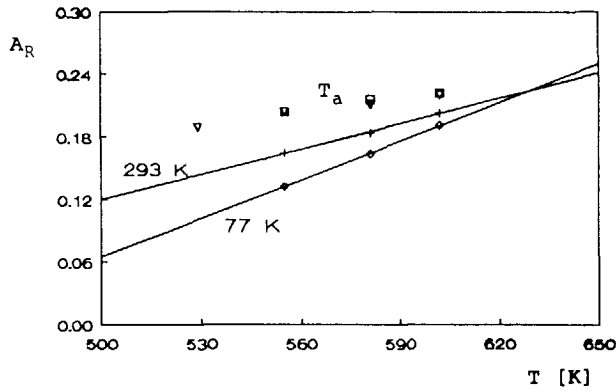


figure 4.5 The slopes of the lines in figure 4.4 plotted versus the annealing temperature. The squares, crosses and diamonds represent the slopes of resp. annealing temperature, room temperature and 77 K. The solid lines are the results of least squares fits. The triangles are the calculated slopes at the annealing temperature, using the procedure described in the text.

Assuming that the relation $A_R(T_m)$ at constant T_a is also linear, the A_R values for the series $T_a = T_m$ can be obtained by extrapolation. The results are given by triangles in figure 4.5. The A_R values obtained by the direct fits of figure 4.4.a (see table 4.1) are represented by squares. The agreement is reasonable.

From the isotherms of figure 4.3 the changes of the electrical resistivity due to CSRO can be obtained by

$$\left(\frac{\Delta R}{R_N}\right)_{\text{CSRO}}(t) = \left(\frac{\Delta R}{R_N}\right)(t) - A_R \Delta x(t), \quad (4.3)$$

where $\Delta x(t)$ is the change of the reduced free volume after an annealing time t . The results are given in figure 4.6. In this figure it is clearly shown that the isotherms saturate. The equilibrium value is the $(\Delta R/R_N)_{\text{eq}}$

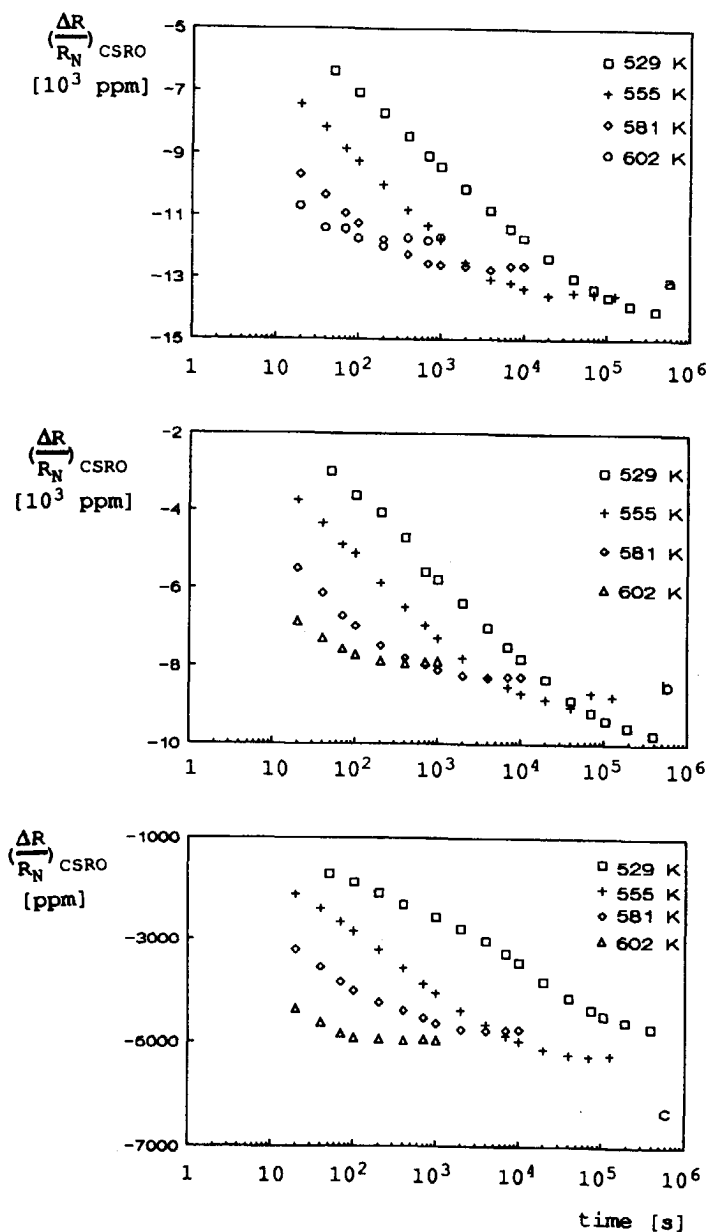


figure 4.6 The isothermal change of the electrical resistivity, after subtraction of the contribution of free volume annihilation, plotted versus the annealing time. The measuring temperatures are (a) annealing temperature, (b) room temperature and (c) 77 K.

as given in table 4.1. The estimated error of these values is ± 200 ppm for the measurements at room temperature and in liquid nitrogen and ± 400 ppm for the measurements at the annealing temperature, due to the fluctuations in the temperature and the experimental error in the observed resistivity.

The quantity $(\Delta R/R_N)_{eq}$ reflects the difference in equilibrium short range order at T_a and the short range order in the as quenched specimens, represented by the fictive temperature T_f . For $T_m = T_a$ and $T_m = 293$ K it can be seen that the absolute value of this quantity decreases with increasing T_a , as expected because the difference in equilibrium short range order between T_f and T_a decreases with increasing T_a . However, for $T_m = 77$ K the values $(\Delta R/R_N)_{eq}$ show a slight increasing tendency. To this surprising result we shall come back in the discussion.

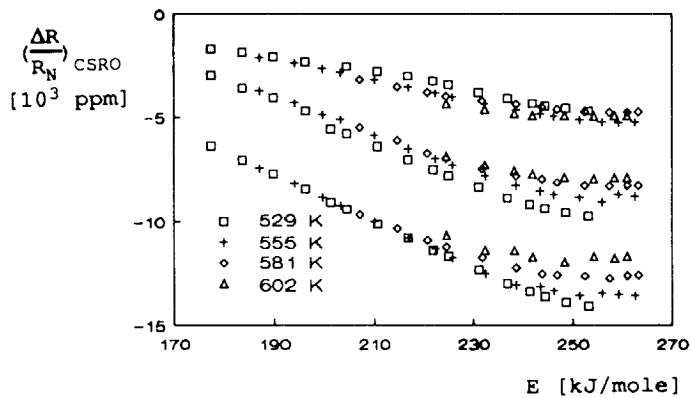


figure 4.7 The isotherms of figure 4.6 plotted versus the activation energy as calculated with equation (4.4).

A different representation of the results is obtained when the CSRO isotherms are plotted versus the activation energy E :

$$E = \frac{RT}{(1-\beta T)} \left\{ -\frac{0.5}{x} + \ln(vt) \right\} \quad (4.4)$$

where β is a constant ($9.7 \cdot 10^{-4} \text{ K}^{-1}$), v is a frequency ($5.1 \cdot 10^9 \text{ s}^{-1}$) and $0.5/x$ involves the effect of the amount of free volume on the ordering kinetics. The background of equation (4.4) which is derived from eqs.

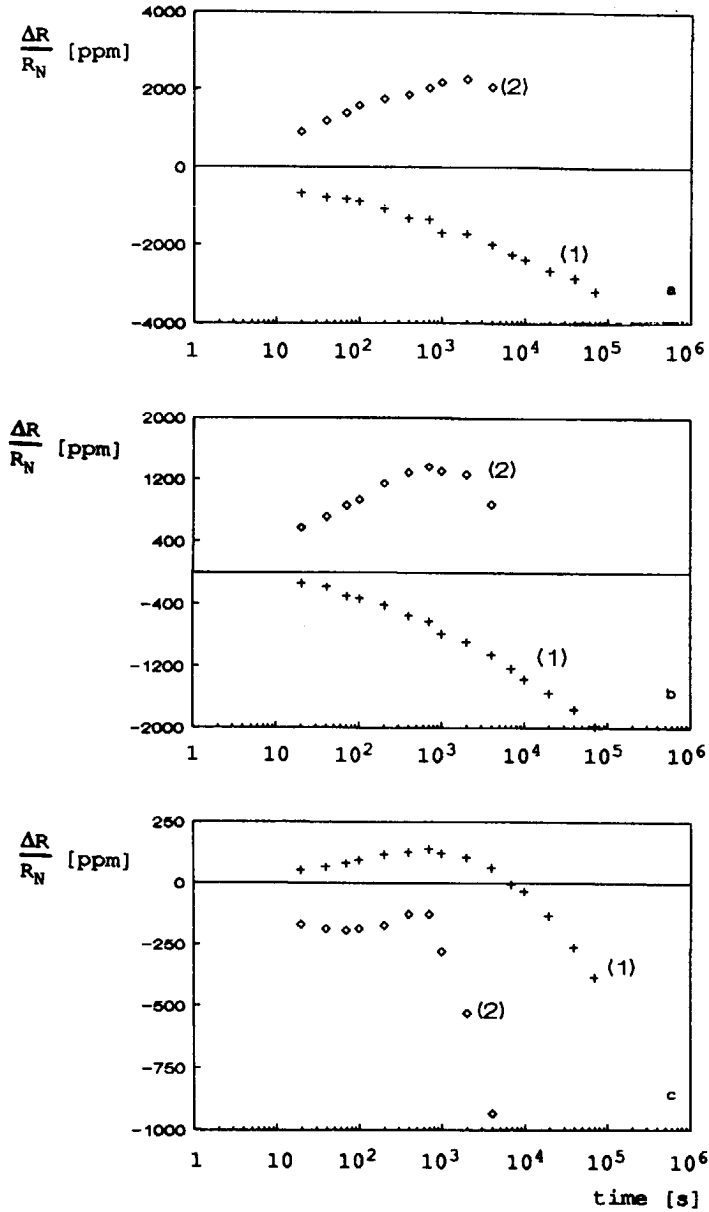


figure 4.8 The isothermal change of the electrical resistivity after preannealing at 602 K versus the annealing time. Annealing was performed first at 555 K (curve (1)) and subsequently at 602 K (curve (2)). The measuring temperatures are (a) annealing temperature, (b) room temperature and (c) 77 K.

(2.23) and (2.24) will be extensively discussed in section 5.2.1.a, including the value of v .

In figure 4.7 all CSRO isotherms are plotted versus the activation energy E . All isotherms saturate to the equilibrium value near the activation energy of 250 kJ/mole. It is remarkable that the initial parts of the isotherms of each measuring temperature nearly coincide. This indicates that this part is only slightly dependent on the annealing temperature.

4.3.3.b Cycling experiments

A specimen was preannealed during 10^3 s at 602 K, which, according to the results of the previous section, is sufficient to establish equilibrium chemical order at that temperature. Then the specimen was annealed at 555 K, during which $\Delta R/R_N$ was measured as a function of time. The results are shown in figure 4.8, curves (1). The measuring temperature was T_a (fig. 4.8.a), 293 K (fig. 4.8.b) and 77 K (fig. 4.8.c). After the 555 K anneal the specimen was again annealed at 602 K; $\Delta R/R_N$ versus time is represented in figure 4.8, curves (2).

Part of the changes in resistivity in figure 4.8 is due to the annihilation of free volume. The CSRO contributions can be obtained by the procedure described before for the as quenched isotherms. The result is shown in figure 4.9, where the CSRO change of the resistivity is plotted versus the activation energy as given by equation (4.4).

In figure 4.9 it is shown that for the isotherms measured at the annealing temperature and at room temperature the electrical resistivity decreases during ordering (annealing at 555 K, curve 1) and increases during disordering (annealing at 602 K, curve 2). This is agreement with the as quenched isotherms, where a decrease in electrical resistivity was found during ordering (figure 4.7). The magnitude of the change in electrical resistivity for the 555 K and 602 K isotherms is resp. -2500 and 2800 ppm at the annealing temperature and -1500 and 1700 ppm at room temperature, which, within the accuracy of the experiments, can be considered as fully reversible behaviour.

The results at 77 K show a more irregular pattern. The reason for this might be the very small reversible contribution (about 150 ppm) compared to the inaccuracy of the set-up. However, the sign of the changes shows that during ordering the electrical resistivity increases,

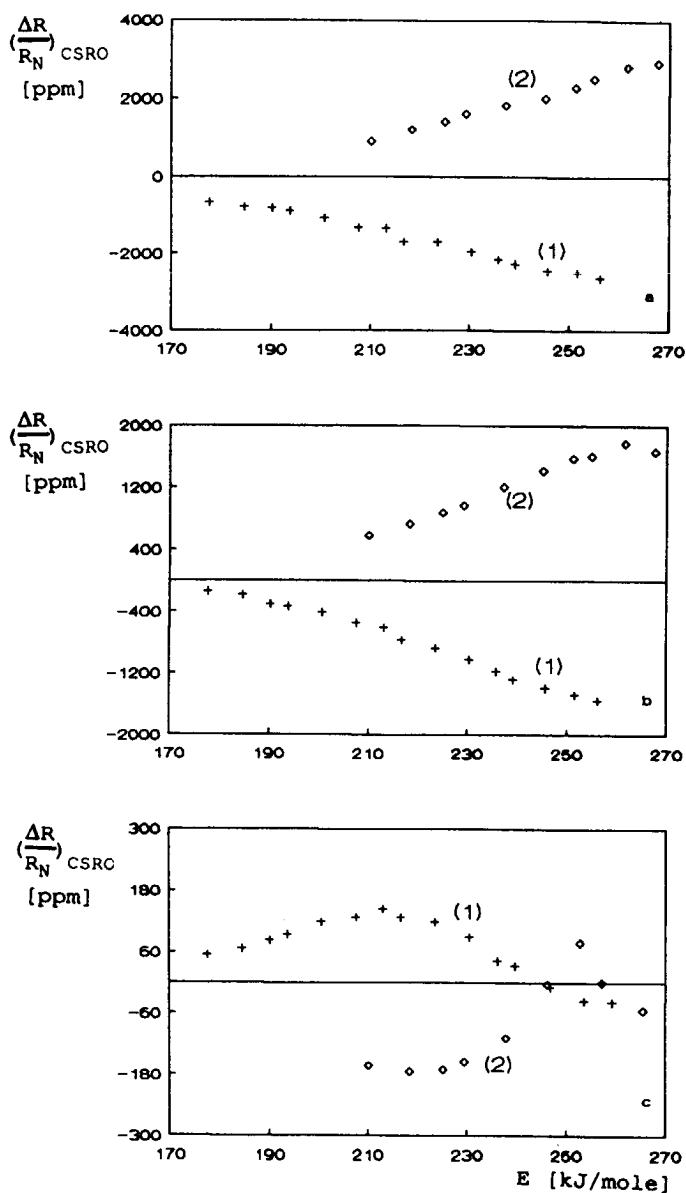


figure 4.9 The isothermal change of the electrical resistivity (data from figure 4.8), after subtraction of the contribution due to free volume annihilation, plotted versus the activation energy calculated with equation (4.4). The measuring temperatures are (a) annealing temperature, (b) room temperature and (c) 77 K.

in contrast with measurements at 293 K and T_a , but in agreement with the slight increasing tendency in $(\Delta R/R_N)_{eq}$ with decreasing T_a (table 4.1). Therefore, during disordering the electrical resistivity is expected to decrease, as can be found in figure 4.9.c (curve 2).

Both isotherms in figure 4.9.c show an extreme around $E = 210$ kJ/mole. The 602 K isotherm also seems to exhibit a maximum at 240 kJ/mole. We do not have a complete explanation for these details in the effect of the reversible processes.

4.3.4 Discussion and conclusion

In figure 4.7 it was shown that for the as quenched specimens the electrical resistivity at all measuring temperatures decreased during annealing due to CSRO processes. The change in electrical resistivity increased with increasing T_m : the observed change in electrical resistivity was larger in the case of the measurements at the annealing temperature than for the measurements at room temperature or at liquid nitrogen temperature. It was also demonstrated that for the isotherms measured at the annealing temperature and at room temperature, $(\Delta R/R_N)_{eq}$ became larger at lower annealing temperature. An opposite tendency is observed for the measurements at 77 K: it seems that the change of electrical resistivity becomes smaller at lower annealing temperature.

As for the cycling experiments, the results could be divided into two groups: the first consists of the isotherms measured at the annealing temperature and at room temperature; the second of the isotherms measured at 77 K. For the first group it was demonstrated that during chemical ordering (annealing at 555 K after preannealing at 602 K) the electrical resistivity decreases. This is in agreement with the as quenched isotherms.

In liquid nitrogen however, the electrical resistivity was found to increase during ordering. This is not compatible with the as quenched results, for which a continuous decrease in electrical resistivity was observed during annealing. Since during this first anneal ordering should occur, the only explanation is a contribution of irreversible processes. The same conclusion was reached by Kokmeyer *et al.* [26] (see also section 2.3). These irreversible processes result in a decrease of electrical resistivity during annealing.

For this reason one should no longer use the name CSRO for the part preceding TSRO, because CSRO was defined to be reversible. Therefore all changes in the observed property in $\text{Fe}_{40}\text{Ni}_{40}\text{B}_{20}$, that are not due to TSRO, will from now on be called pre-TSRO: it consists of reversible CSRO plus irreversible processes, the nature of which is unknown.

Since the observed reversible contribution at 77 K was found to be small, it is expected that most of the pre-TSRO changes in electrical resistivity for the as quenched samples at $T_m = 77$ K are due to irreversible processes. This means that, because the resistivity changes monotonously in the pre-TSRO range and exhibits no clear change in slope (due to a transition from irreversible to CSRO), these processes contribute over the entire pre-TSRO range.

In figure 4.9 the reversible changes of the electrical resistivity were given as a function of the activation energy. From these figures it can be concluded that the reversible processes have activation energies between 170 and 250 kJ/mole. In figure 4.7 however, it is demonstrated that the change of the electrical resistivity is not zero up to 170 kJ/mole for the as quenched isotherms. Therefore, these changes, connected with the first part of the CSRO spectrum presented in chapter 2, must be due to irreversible processes.

In a previous study on the change of the electrical resistivity during structural relaxation [26], it was assumed that the irreversible part of the pre-TSRO, named R3, was independent of the measuring temperature. However, the result that the first part of the as quenched isotherms is irreversible and dependent on the measuring temperature, shows that the irreversible change in electrical resistivity does depend on the measuring temperature. Extrapolation of the isotherms of figure 4.7 to 170 kJ/mole gives an illustration of this dependency.

The magnitude of the reversible changes in the electrical resistivity, as observed in the cycling experiments, was about 2600 and 1600 ppm for resp. the measurements at the annealing temperature and at 293 K. These values were larger than the differences in electrical resistivity obtained from table 4.1 (1800 and 900 ppm between 555 and 602 K for resp. annealing and room temperature). For the measurements at room temperature, this difference is significant. For the measurements at the annealing temperature however, a correction is necessary because the changes of the electrical resistivity depend on T_m . Assuming that

$(\Delta R/R_N)_{eq}$ is linear with T_m between room and annealing temperature, a reversible change of the electrical resistivity of about 2300 ppm between 555 and 602 K is expected. This procedure implicitly corrects for the T_m dependence of the irreversible processes.

The reversible change of the electrical resistivity was expected to saturate at about 250 kJ/mole when these changes were plotted versus the activation energy. In figure 4.9 however, this is not clearly the case. This may be due to an insufficient correction of the electrical resistivity for free volume annihilation, partially due to the inaccuracy in A_R .

From table 4.1 it is clear that the A_R values at constant T_m depend on T_a . This might be due to the different states of CSRO at the various annealing temperatures. However, this was never observed in, for instance, Young's modulus measurements, where the proportionality factor A_E was found to be independent of the annealing temperature.

Mihara *et al.* [2] have measured the change of the electrical resistivity during structural relaxation after isochronal annealing for $Fe_{40}Ni_{40}P_{14}B_6$ both at liquid nitrogen temperature and at room temperature. They found that the electrical resistivity increases after low temperature annealing and then decreases upon further annealing at higher temperatures. The magnitude of the changes in the electrical resistivity decreases with increasing T_m . Balanzat [28] reported isochronal electrical resistivity measurements on the same metallic glass, performed in liquid helium. He found a similar pattern as was reported by Mihara *et al.*. Isochronal electrical resistivity studies in liquid helium on an $Fe_{40}Ni_{40}B_{20}$ metallic glass [23] have shown that for the as-quenched metallic glass the electrical resistivity slightly increases. According to the reported isothermal changes in electrical resistivity, this might be due to an increase in electrical resistivity due to chemical ordering and a decrease due to the irreversible processes, which effects could cancel each other completely. The initial increase in the electrical resistivity in the $Fe_{40}Ni_{40}P_{14}B_6$ metallic glass is, according to the presented model, also due to chemical ordering and the irreversible processes in the pre-TSRO region. Because a clear initial increase in electrical resistivity was observed in the isochronal measurements, it can be concluded that the irreversible processes are less important for the changes in the electrical resistivity of this

metallic glass but their contribution increases with increasing measuring temperature.

4.4 Discussion

In the previous sections it was found that in structural relaxation for amorphous $\text{Fe}_{40}\text{Ni}_{40}\text{B}_{20}$ three types of processes play a role: one is reversible, the other two irreversible. One irreversible process is Topological Short Range Order (TSRO), as reported earlier. It was found in section 4.2 that the positron lifetime starts to decrease at $t = \tau_{iv}$ when, according to previously reported data, TSRO becomes important. In section 4.3 a small change of the slope in the as quenched resistivity isotherms was reported at $t = \tau_{iv}$, corresponding to the onset of TSRO.

The pre-TSRO part of the isotherms could be divided in two types of processes, reversible and irreversible. The reversible processes are known as Chemical Short Range Ordering (CSRO). It was found that the spectrum of activation energies for CSRO is less wide than reported in chapter 2. Only processes with an activation energy between 170 and 250 kJ/mole showed reversible behaviour. The processes that evolve before CSRO are irreversible and so is part of the processes in the activation energy range between 170 and 250 kJ/mole.

The conclusion that only the final part of the spectrum contains reversible processes was based on cycling experiments. It was found that reversible changes of the electrical resistivity started with processes with an activation energy of about 170 kJ/mole (figure 4.9). This is in agreement with analogous experiments on Young's modulus [29], as shown in figure 4.10. In this figure the change of Young's modulus, represented by Δv^2 , during cycling experiments is plotted versus the activation energy. After a preanneal at 600 K the annealing temperature was changed to 525 K and the change of the modulus was measured. Then, the temperature was changed to 600 K and the change of the modulus was measured again. The procedure of cycling between 525 and 600 K was repeated in the 4th and 5th anneal. In figure 4.10 the reversible changes of the modulus can be observed. This figure clearly demonstrates that the changes in Young's modulus start at $E=170$ kJ/mole.

For the change of the positron lifetime it was found that the pre-TSRO part (ABC) of the isotherms exhibits a minimum in the lifetime, at an activation energy of between 180 and 220 kJ/mole. It seems

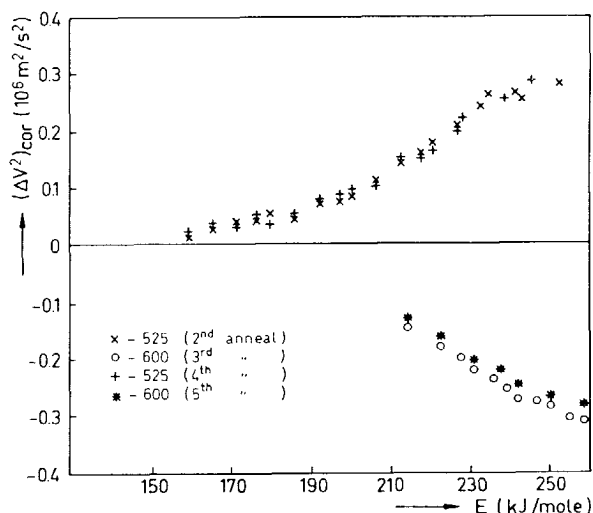


figure 4.10 The isothermal change of v^2 , after subtraction of the contribution due to free volume annihilation, upon sequential annealing at the indicated temperatures for a specimen preannealed at 600 K for 600 seconds [29].

reasonable to conclude that the initial decrease in positron lifetime is due to the irreversible processes, because the first part of pre-TSRO in electrical resistivity was found to be irreversible. The subsequent increase in lifetime (BC) is then attributed to reversible CSRO.

Huizer *et al.* [30] have also reported an irreversible process in the pre-TSRO part in amorphous $\text{Fe}_{40}\text{Ni}_{40}\text{B}_{20}$. They measured the length changes during cycling experiments and found that only a small part of the observed length changes in the pre-TSRO range for an as quenched sample was reversible. Therefore, they concluded that the spectrum of activation energies could be divided into two regions, a lower energy part describing the irreversible process and a higher energy part describing the reversible processes. The activation energy for which the first part passes into the second was about 200 kJ/mole. This activation energy agrees very well with the activation energy belonging to the minimum (B) in the positron lifetime measurements. However, it disagrees with the $E = 170$ kJ/mole as found for Young's modulus and electrical resistivity measurements. An explanation for this discrepancy cannot be given at the moment.

The interpretation of the irreversible processes in the pre-TSRO part is still uncertain. Model calculations often show that small metalloid atoms could be enclosed by cages of larger metal atoms. However, Sietsma and Thijssse [31] have concluded that boron atoms in as quenched $\text{Ni}_{80}\text{B}_{20}$ might very well be on "substitutional" positions, which means that there is no principal difference between metal and metalloid positions. It is possible that during the first anneal of an as quenched glass the metalloid atoms migrate into "holes" surrounded by metal atoms and remain there, independent of the annealing temperature. This process can then be considered irreversible. The structure densifies during this process, which results in a decrease of the length, in accordance with Huizer's observations [30] and a decrease of the positron lifetime (section 4.2). The validity of this picture should be investigated by molecular dynamics studies.

4.5 Conclusions

- 1 The final part of structural relaxation (TSRO) as monitored by measurements of the electrical resistivity can be described by the formalism of the free volume model, with the same parameters as derived earlier from other types of experiments.
- 2 The positron lifetime measurements marked, for the first time, a clear transition between the TSRO and the pre-TSRO region.
- 3 In contrast to earlier analysis, the pre-TSRO region (activation energy spectrum between $E = 130$ kJ/mole and $E = 250$ kJ/mole) contains both reversible and irreversible processes. This follows from the changes of the electrical resistivity as measured at three different measuring temperatures (77 K, 293 K and the annealing temperature) in combination with temperature cycling experiments. According to resistivity (section 4.3) and Young's modulus data [29] the reversible processes start at about $E = 170$ kJ/mole. Length [30] and positron lifetime (section 4.2) data seem to indicate that reversible processes start at about $E = 200$ kJ/mole.

- 4 The reversible processes are ascribed to chemical short range ordering (CSRO). The nature of the irreversible processes in the pre-TSRO range is as yet unknown.

References

- 1 R.H. Howell and R.W. Hopper, *Scripta Metall.* 13, 367 (1979).
- 2 T. Mihara, S. Otake, H. Fukushima and M. Doyama, *Journ. Phys F: Metal Physics* 11, 727 (1981).
- 3 S. Tanigawa, K. Shima. and T. Masumoto, in *Proc. 4th Int. Conf. on Rapidly Quenched Metals*, Sendai, 1981, eds. T. Masumoto and K. Suzuki, Japan Inst. Met., Sendai, 1982, p. 501.
- 4 H.S. Chen and S.Y. Chuang, *Appl. Phys. Lett.* 31, 255 (1977).
- 5 A. Schiltz, A. Liolios, C. Elefteriades, M. Chardales, S. Dedoussis and S. Charamlambois, in *Proc. 7th Int. Conf. on Positron Annihilation* (1984), eds. P.C. Jain, R.M. Singru and K.P. Gopinathan, Singapore 1985, p. 122.
- 6 S. Tanigawa, K. Hinode, R. Nagai, K. Kanbe, M. Doyama and N. Shiotani, *Phys. Stat. Sol. (a)* 51, 249 (1979).
- 7 H.S. Chen and S.Y. Chuang, *Journ. of Electr. Mat.* 4, 783 (1975).
- 8 H.S. Chen and S.Y. Chuang, *Phys. Stat. Sol. (a)* 25, 581 (1974).
- 9 J. Filipecki, G. Antosik, B. Calusinski and D. Gaudyn, *Phys. Lett. (a)* 122, 195 (1987).
- 10 H.S. Chen, *Phys. Stat. Sol. (a)* 34, K127 (1976).
- 11 P. Hautojärvi and J. Yli-Kauppila, *Nucl. Instr. and Meth.* 199, 75 (1982).
- 12 K. Petersen, N. Thrane and R.M.J. Cotterill, *Phil. Mag.* 29, 9 (1974).
- 13 J. de Vries, Ph.D. Thesis, Delft University of Technology, Delft 1987.
- 14 K. Petersen, Ph.D. Thesis, Technical University of Denmark, Lyngby 1979.
- 15 P. Kirkegaard and M. Eldrup, *Comp. Phys. Comm.* 23, 307 (1981).
- 16 F.F. Luborsky, *Mat. Sci. Eng.* 28, 139 (1977).
- 17 J. van der Stel, H.B. van Veldhuizen, G.W. Koebrugge, J. Sietsma and A. van den Beukel, *Phys. Stat. Sol. (a)* 112, 35 (1989).
- 18 K.F. Kelton and F. Spaepen, *Phys. Rev. B* 30, 5516 (1984).
- 19 G. Riontino and F. Marino, *Scripta Metall.* 18, 13 (1984).

- 20 E. Woldt and J.A. Leake, in Proc. 5th Int. Conf. on Rapidly Quenched Metals, Würzburg, 1984, eds. S. Steeb and H. Warlimont, North-Holland Physics Publishing, Amsterdam 1985, p 687.
- 21 J.R. Cost and J.T. Stanley, Scripta Metall. 15, 407 (1981).
- 22 T. Komatsu and K. Matusita, Journ. of Mat. Sci. 21, 1693 (1986).
- 23 E. Balanzat, J.T. Stanley, C. Mairy and J. Hillairet, Acta Metall. 33, 785 (1985).
- 24 E. Huizer, H. Melissant, A. van den Beukel in Proc. 6th Int. Conf. on Liquid and Amorphous Metals, Garmisch-Partenkirchen, 1986, eds. W. Gläser, F. Hensel and E. Lüscher, Z. für Phys. Chemie (neue Folge) 1, München 1987, vol. 2 p. 335.
- 25 T. Komatsu, R. Yokota, T. Shindo and K. Matusita, Journ. of Non-Cryst. Sol. 65, 63 (1984).
- 26 E. Kokmeijer, E. Huizer, B.J. Thijsse and A. van den Beukel, Phys. Stat. Sol. (a) 105, 235 (1988).
- 27 A. van den Beukel in "Rapidly Quenched Materials", eds. P.W. Lee and A.S. Carbonera, San Diego 1986, p.193.
- 28 M. Balanzat, Scripta Metall. 14, 173 (1980).
- 29 E. Huizer, Ph.D. Thesis, Delft University of Technology, Delft 1987.
- 30 E. Huizer and A. van den Beukel, Acta Metall. 35, 2843 (1987).
- 31 J. Sietsma and B.J. Thijsse, J. Non-Cryst. Sol. 101, 135 (1988).

CHAPTER 5

DIFFUSION AND FLOW DEFECTS IN METALLIC GLASSES

5.1 Introduction

Atomic transport in amorphous materials can be studied in the most direct way by measurements of the diffusion coefficient and the viscosity [1]. More indirect methods are the study of processes that are assumed to be related to diffusion.

Diffusion experiments in metallic glasses are hard to perform because the diffusion lengths that can be attained are very short, often not more than about 10 nm. The reason for this is that the diffusion measurements are limited in time and temperature. At low temperature the diffusion rate is very small, which means that long annealing times are required to attain a sufficiently long diffusion length. At higher temperatures the time is limited because of the onset of crystallisation. Another problem is the change in the amorphous state due to structural relaxation. The amorphous state is not stable and will relax to a more stable one during annealing. Therefore the diffusion coefficient in principle changes during annealing.

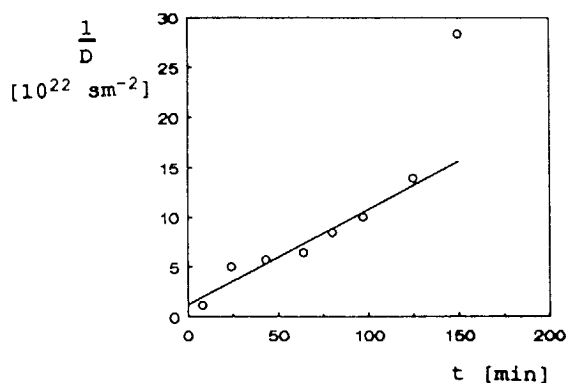


figure 5.1 The interdiffusion coefficient D in amorphous FeB/PdSi multilayers during annealing at 573 K, plotted versus the annealing time. Data obtained from ref. [9].

Many groups have tried to describe the influence of structural relaxation on diffusion [2-11]. Tracers and impurities, like Au, were used to study the diffusion behaviour. Generally no or a small decrease of the diffusion coefficient during structural relaxation was observed. Perhaps the largest effect of structural relaxation on D reported is shown in figure 5.1 [9]. In this figure, the Pd-Fe interdiffusion coefficient D for an PdSi/FeB multilayer is plotted as $1/D$ versus the annealing time.

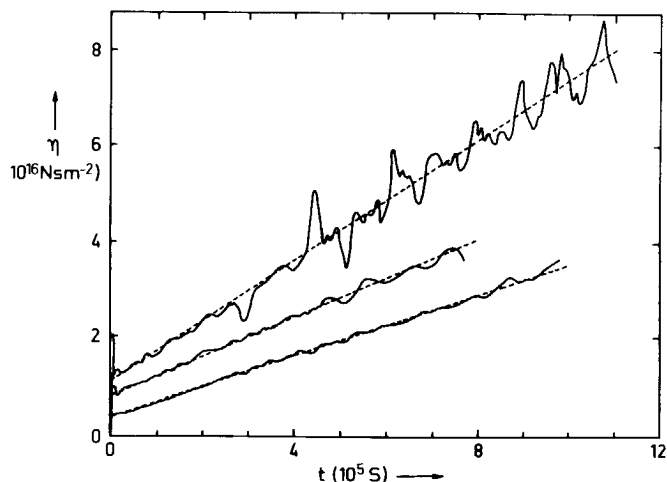


figure 5.2 The isothermal change of the viscosity of $\text{Fe}_{40}\text{Ni}_{40}\text{B}_{20}$ for one sample during subsequent annealing at 543 K, 563 K and 583 K after preannealing at 523 K [12].

The above mentioned difficulties do not occur when the change of the *viscosity* η is measured during structural relaxation in amorphous materials, because η , unlike D , can be determined instantaneously. When a stress is applied on an amorphous ribbon the length of the ribbon continuously increases due to flow. The ratio between the shear stress and the flow rate is the viscosity η . It was found [12], as shown in figure 5.2 for $\text{Fe}_{40}\text{Ni}_{40}\text{B}_{20}$, that the viscosity increases linearly with time during annealing, as long as the glass under investigation is far from its metastable equilibrium state. Near equilibrium the viscosity saturates to a constant value (see chapter 6).

In the free volume theory of structural relaxation the decrease in D and increase in η are ascribed to the annealing out of defects that build

up the free volume (chapter 2), which densifies the material and decreases the atomic mobility. It is assumed that $D \propto c_d$ and $\eta \propto c_f^{-1}$, where c_d and c_f are the concentration of resp. diffusion and flow defects. If viscosity and diffusion are governed by the same defect, as is generally assumed, the Stokes-Einstein equation

$$\eta D = \text{constant}, \quad (5.1)$$

which is well obeyed in liquids, is expected to hold. However, studies of both viscosity and diffusion during structural relaxation give rise to the conclusion that the Stokes-Einstein relation probably does not hold [13].

The assumption that the Stokes-Einstein relation is valid is used in the literature, e.g. [14]. The observation that $1/D$ (figure 5.1) and η (figure 5.2) are linear with time are the basic assertions for this. However, when deriving the proportionality factor in the expression for the Stokes-Einstein relation from the experimental data, which is on the order of one atomic radius in liquids, unrealistic values (wrong by a factor up to 600) were found.

It is possible to study the influence of structural relaxation on the diffusion coefficient in an indirect way. Chemical Short Range Ordering (CSRO) is assumed to be a diffusion process. The process is assumed to take place by a few jumps per atom. It is expected that diffusion defects play an important role in this process. If the number of defects decreases, the ordering kinetics is expected to slow down.

In this chapter experiments are described to study the change of the ordering kinetics due to prolonged annealing. To this end both chemical ordering and stress induced ordering experiments have been performed. The results will be described in terms of the decrease of the concentration of flow defects. The findings are used to analyse the change of the diffusion coefficient during structural relaxation as presented in the literature. The related consequences for the validity of the Stokes-Einstein relation will be discussed.

5.2 Results

5.2.1 Fe₄₀Ni₄₀B₂₀

5.2.1.a Chemical Short Range Ordering

Young's modulus measurements were performed to measure the change of chemical ordering kinetics in amorphous Fe₄₀Ni₄₀B₂₀ during cycling experiments. A description of the set-up is given in section 3.2.

TABLE 5.1

Annealing program and calculated reduced free volume x at the end of each anneal

T [K]	t [s]	x
600	250	0.07107
550	40000	0.06794
600	7000	0.05913
550	715220	0.05688

In order to follow the change of the ordering kinetics, the modulus was measured by cycling between two annealing temperatures, 600 and 550 K. The annealing history and the calculated reduced free volume after each annealing treatment, as calculated by use of the equation

$$\exp(x^{-1}) - \exp(x_0^{-1}) = C_0 \exp(-E_f/RT), \quad (2.8)$$

are given in table 5.1. In equation (2.8) C_0 and E_f are $1.63 \cdot 10^{25} \text{ s}^{-1}$ and 250 kJ/mole, respectively, whereas $x_0 = 0.07527$ for the as quenched samples.

The first anneal, 250 sec. at 600 K, was performed to attain equilibrium order at 600 K. This means that after this anneal only reversible chemical ordering and irreversible TSRO will occur (see chapter 4). The observed v^2 is represented in figure 5.3. After the

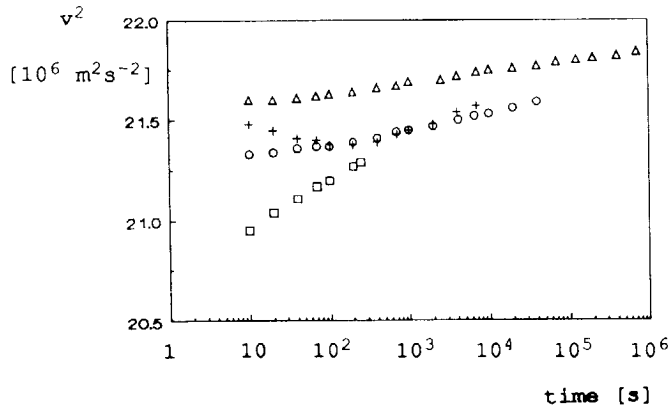


figure 5.3 The isothermal change of Young's modulus in $\text{Fe}_{40}\text{Ni}_{40}\text{B}_{20}$, represented by v^2 , after subsequently annealing at 600 K (\square), 550 K (o), 600 K (+) and again at 550 K (Δ).

preanneal at 600 K, the samples were subsequently annealed at 550 K (40000 seconds), 600 K (7000 seconds) and again at 550 K (715220 seconds). The observed v^2 for these annealing treatments is also plotted versus the logarithm of time in figure 5.3.

The increase of v^2 during annealing at 550 K is due to two processes. The first is, due to lowering the temperature from 600 K to 550 K, the increase of the degree of chemical order. This gives rise to an increase in v^2 . The second process is the annealing out of free volume (TSRO), which starts when chemical short range ordering is completed. This also gives rise to an increase in v^2 . Because the kinetics of annealing out of free volume is known, the effect of the two processes on v^2 can be separated. The change in v^2 due to annealing out of free volume is given by $\Delta v_{\text{TSRO}}^2 = A_E \Delta x$ [15], where A_E is a constant ($24 \cdot 10^6 \text{ m}^2\text{s}^{-2}$), and can be subtracted from the total change measured. The result is the change in v^2 due to CSRO.

In figure 5.4 the change in v^2 due to chemical ordering is given for the two isotherms at 550 K. The presented isotherms are an average result of three different samples, the accuracy in Δv^2 is (see chapter 3) $\pm 0.01 \cdot 10^6 \text{ m}^2\text{s}^{-2}$.

In figure 5.4 it is shown that the second curve is shifted with respect to the first one to longer times. During the second anneal at 600 K, the amount of free volume is decreased, as given in table 5.1, so the

kinetics of chemical ordering indeed slows down with decreasing free volume.

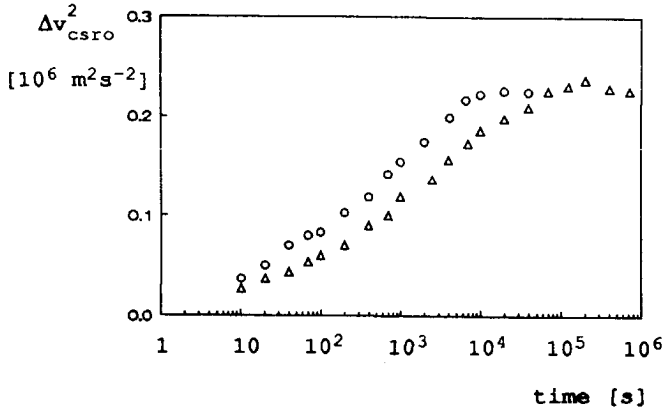


figure 5.4 The isothermal changes of v^2 at 550 K in $\text{Fe}_{40}\text{Ni}_{40}\text{B}_{20}$, after subtracting the contribution due to free volume annihilation. The symbols (o) and (Δ) represent the first resp. second anneal.

The relaxation time τ for an ordering process with an activation energy E can be represented by

$$\tau = v_d^{-1} c_d^{-1} \exp(E/RT) = v_d^{-1} c_d^{-1} \exp(E_0/RT_{\text{eff}}), \quad (5.2)$$

in which v_d is the Debye frequency. The second equality relates to eq. (2.23), with $T_{\text{eff}} = \frac{T}{1-\beta T}$. If during an annealing treatment c_d changes by a factor s , τ changes by a factor s^{-1} , which is visible on a logarithmic time scale (like in figure 5.4) by a shift of the curves over $\log(s^{-1})$. If the assumption $c_d = c_f$ is correct, the shift factor s between the two isotherms in figure 5.4 can be calculated by

$$s = \frac{\tau_2}{\tau_1} = \frac{c_{f1}}{c_{f2}} = \exp\left(\frac{1}{x_2} - \frac{1}{x_1}\right), \quad (5.3)$$

where the subscripts 1 and 2 denote the first and second isotherm at 550 K, respectively.

The calculated shift factor s is then 17.1. In figure 5.4, however, the observed shift factor is 4 ± 0.5 . So the observed shift factor is not in agreement with the predicted one.

This effect has been further investigated by varying the annealing time of the annealing treatment at 600 K between the two treatments at 550 K. In table 5.2 the observed (s_{obs}) and calculated shift factor (s_{calc}) are given for several annealing treatments at 600 K. The results give rise to the conclusion that the observed shift factor is about the square root of the expected one, which implies $c_d \propto \sqrt{c_f}$.

TABLE 5.2

Experimental and calculated shift factors between the two isothermals at 550 K as a function of the intermediate annealing time t_a at 600 K.

t_a [s]	s_{calc}	s_{obs}
1000	4.1	2
2000	6.7	2
7000	17.1	4

The validity of this result can be illustrated as follows. In equation (5.2) a relation between the relaxation time τ and the concentration of diffusion defects c_d is given. It follows from this equation that on a modified time scale $c_d \cdot t$ the curves will coincide. In figure 5.5 the observed change in v^2 is replotted in this way, where in figure 5.5.a $c_d = c_f$ is assumed and in figure 5.5.b $c_d = \sqrt{c_f}$. It is clearly demonstrated that in the latter case the curves indeed coincide.

According to the Primak approximation in the AES model, annealing during a time t at temperature T will give rise to equilibrium ordering of all processes with $\tau \leq t$. It follows from (5.2) that the spectrum is ordered up to an energy E_0 given by

$$E_0 = RT_{\text{eff}} \ln(v_d c_d t). \quad (5.4)$$

This equation was already presented in chapter 2 (eq. 2.23), with $v_0 = v_d c_d$. For as quenched measurements $v_0 = 6.6 \cdot 10^6 \text{ s}^{-1}$ was found and $x_0 = 0.07527$.

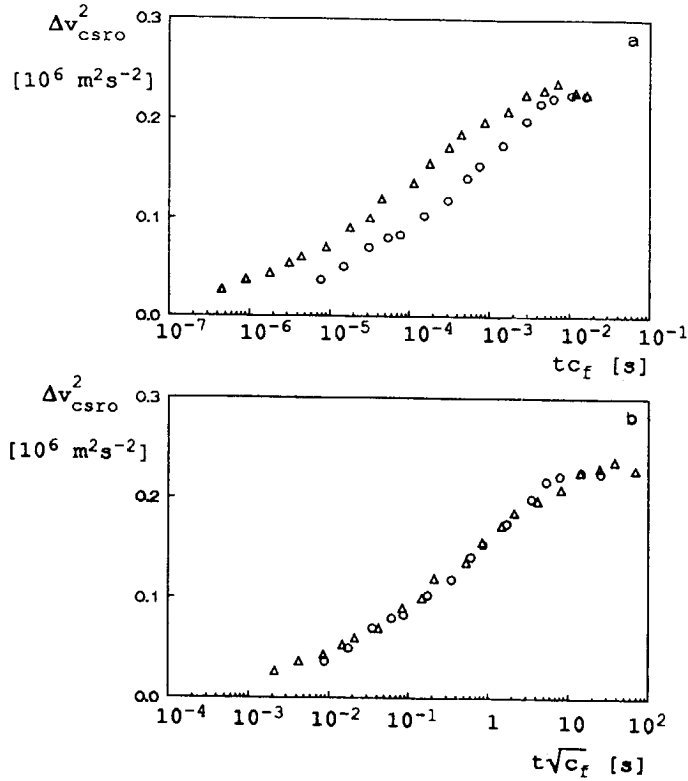


figure 5.5 The isotherms of figure 5.5, now plotted on the modified time scale $t c_f$ (a) and $t \sqrt{c_f}$ (b).

For v_d the value $5.1 \cdot 10^9 \text{ s}^{-1}$ follows, using $c_d = \sqrt{c_f} = \exp(-0.5/x)$. This value is smaller than the expected Debye frequency ($\sim 10^{13} \text{ s}^{-1}$). In the literature [16,17] it is suggested that low frequency factors mean that clusters of atoms are involved during chemical ordering, vibrating collectively.

Equation (5.4) can be replaced by

$$E_0 = RT_{\text{eff}} \left\{ -\frac{0.5}{x} + \ln(v_d t) \right\}. \quad (5.5)$$

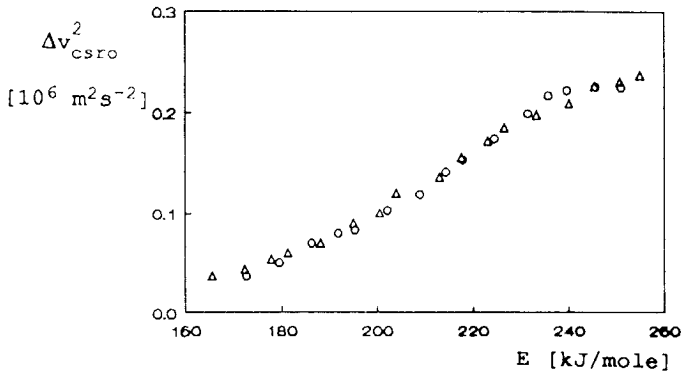


figure 5.6 The isotherms of figure 5.5, now plotted versus the activation energy calculated with eq. (5.5).

According to equation (5.5) the isotherms at 550 K should coincide when they are plotted versus the activation energy E_0 . Figure 5.6 shows the coincidence of the isotherms on an energy scale.

The findings about the slowing down of the ordering kinetics were verified by electrical resistivity measurements. The measurements were performed at the annealing temperature with the set-up presented in section 3.3.

In figure 5.7 the isothermal change of the electrical resistivity, corrected for changes due to the annihilation of free volume as described previously in chapter 4, is plotted. After preannealing at 600 K (250 seconds) the temperature was subsequently changed to 550 K (2), 600 K (3), 550 K (4) and 600 K (5). The change of the resistivity is ascribed to changes in chemical order. An increase in chemical order, due to a decrease in temperature, results in a decrease in electrical resistivity.

In figure 5.7 a slowing down of CSRO kinetics can be observed because the isotherms shift to longer times due to the annihilation of defects during the previous anneal.

In figure 5.8.a and 5.8.b the observed change of the electrical resistivity is replotted on a modified time scale $c_d \cdot t$ where in figure 5.8.a $c_d = c_f$ is assumed and in figure 5.8.b $c_d = \sqrt{c_f}$. It is seen that only in the latter case the required coincidence of the curves is obtained, confirming the relation $c_d \propto \sqrt{c_f}$.

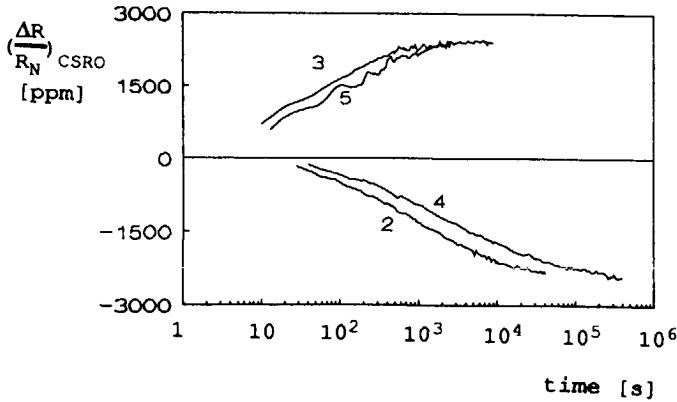


figure 5.7 Isothermal changes of the electrical resistance in $\text{Fe}_{40}\text{Ni}_{40}\text{B}_{20}$ during subsequently annealing at 550 K (2), 600 K (3), 550 K (4) and 600 K (5) after a preanneal at 600 K (not shown). The free volume contribution has been subtracted.

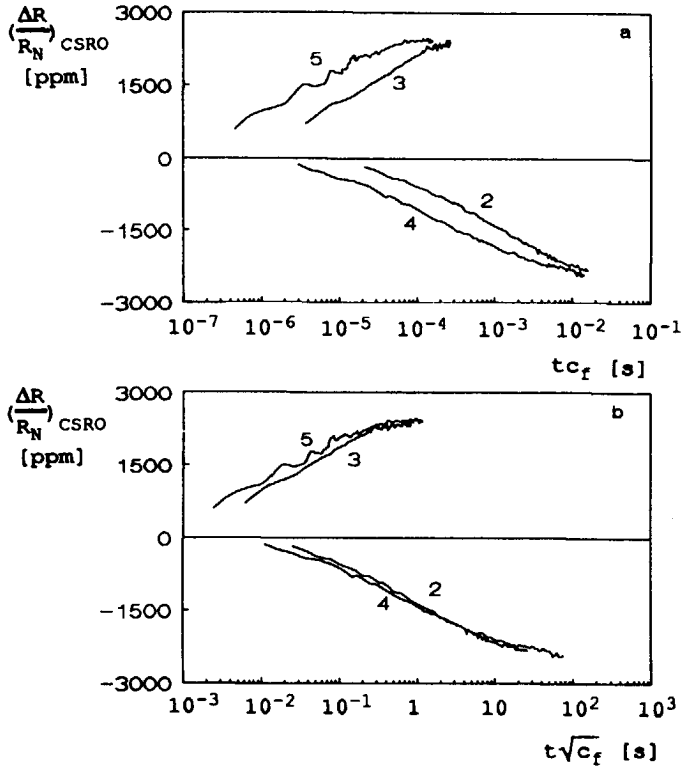


figure 5.8 The isotherms of figure 5.7, now plotted on the modified time scale $t \cdot c_f$ (a) and $t \sqrt{c_f}$ (b).

From the above presented results for both Young's modulus and electrical resistivity it can be concluded that diffusion defects and flow defects are not identical. It was found that the concentration of the two types of defects are related by $c_d \propto \sqrt{c_f}$.

5.2.1.b Stress induced ordering

When a stress is applied to a metallic glass specimen, after an instantaneous elastic strain a time dependent strain is observed. When this strain is proportional to the stress and reversible, it is called anelastic. In figure 5.9 this process is shown by a schematic picture. The initial part of the curve, before the strain becomes entirely plastic, is due to the anelastic relaxation whereas the instantaneous strain is elastic. The linear part is due to creep. The reversibility of both the elastic and anelastic strain is shown by the final part of figure 5.9, where a schematic curve is given when the stress is removed at $t = t_1$.

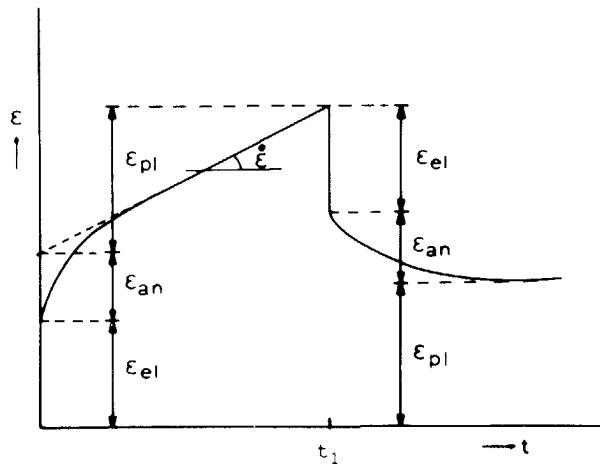


figure 5.9 Schematic deformation curve showing the elastic, anelastic and plastic components of the strain ϵ after loading at $t = 0$ and unloading at $t = t_1$.

The anelastic strain is caused by the fact that the atoms move to new, stress dependent equilibrium positions. This is assumed to be a diffusion process. If the migrating atoms make use of defects to move from one position to another, it is expected that the kinetics of stress

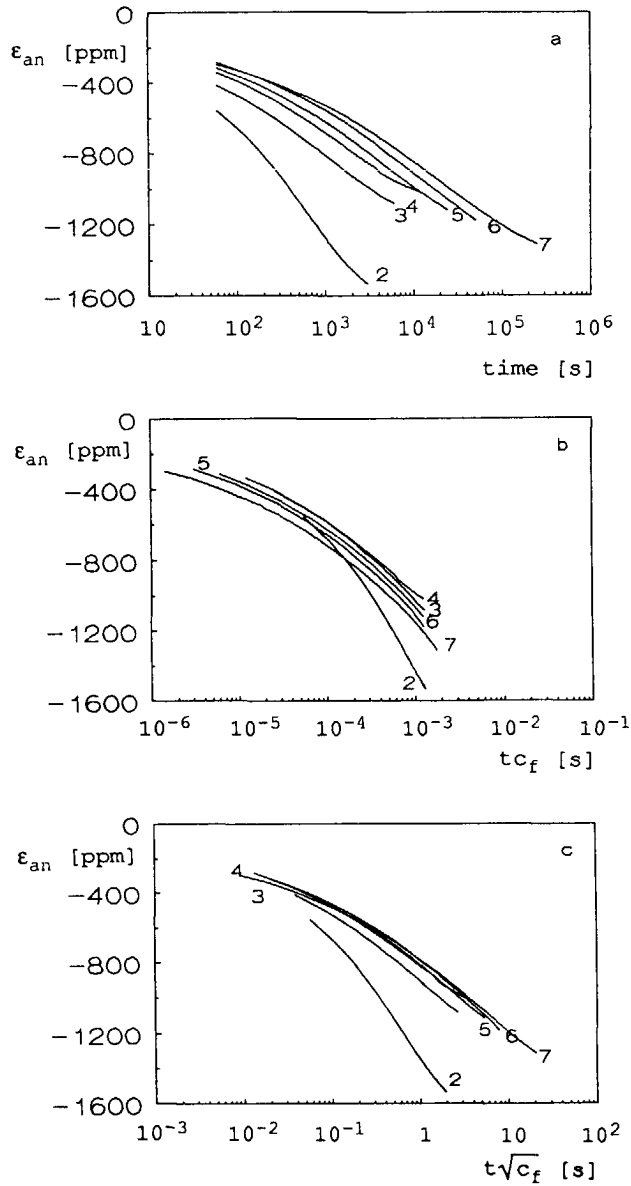


figure 5.10 Anelastic strain in $\text{Fe}_{40}\text{Ni}_{40}\text{B}_{20}$ during annealing at 578 K, plotted as a function of time t (a), $t c_f$ (b) and $t \sqrt{c_f}$ (c). The data are obtained from ref. [18].

induced ordering slows down when the concentration of defects decreases.

Leusink and van den Beukel [18] have reported anelastic relaxation experiments in amorphous $\text{Fe}_{40}\text{Ni}_{40}\text{B}_{20}$. They have studied the ordering kinetics during subsequent loading and unloading under isothermal conditions at temperatures between 550 and 600 K. They have concluded that the ordering kinetics slows down proportionally to c_f .

However, it turns out that the rather inaccurate elastic strain determination of Leusink *et al.* influences their conclusions. In their case it was impossible to observe the instantaneous elastic strain directly, because the first datapoint after applying or removing a stress was obtained after 60 seconds. During these 60 seconds not only the elastic strain but also a part of the anelastic strain evolves. Therefore, in order to correct the observed strain for the elastic contribution, they assumed the elastic strain to change linearly with the temperature and calculated it from a direct measurement of the elastic strain at 313 K.

The inaccuracy of the elastic strain was estimated at 50 ppm, and therefore they admitted a shift of ± 50 ppm along the strain axis to make the isotherms coincide. This latter assumption is very important for the final results, as can be seen in figure 5.10.

In figure 5.10 one of the experiments, presented by Leusink *et al.* [18] and named in their paper as C, is reanalysed, *not* allowing the isotherms to be shifted along the strain axis. In figure 5.10.a the measured anelastic strain is plotted versus time. The curves measured during loading are multiplied with -1. When the data of figure 5.10.a are plotted on the modified time scale $t \cdot c_d$, where $c_d = c_f$ (figure 5.10.b) or $c_d = \sqrt{c_f}$ (figure 5.10.c), it seems that the latter is the best approximation; nearly all curves coincide, only (2) and (3) fail to do so. This conclusion could not be drawn from all the experimental curves of Leusink *et al.*. In some cases this test proved indecisive.

In order to obtain more evidence for one of the relations between c_d and c_f , new experiments were performed. A description of the set-up is given in section 3.4. The difference with the set-up used by Leusink *et al.* is that two Keithley 195A multimeters were used for the registration of the in- and output of the Linear Variable Displacement Transducer (LVDT). With this new set-up, fast sampling is possible. This possibility was used to collect 275 data points during the first 50 seconds. Applying

or removing the stress took only a few seconds. In figure 5.11 a typical result is given for the first 60 seconds in an unloading experiment. Extrapolation of the data points leads to a value of -1810 ± 20 ppm for the elastic strain, an important improvement.

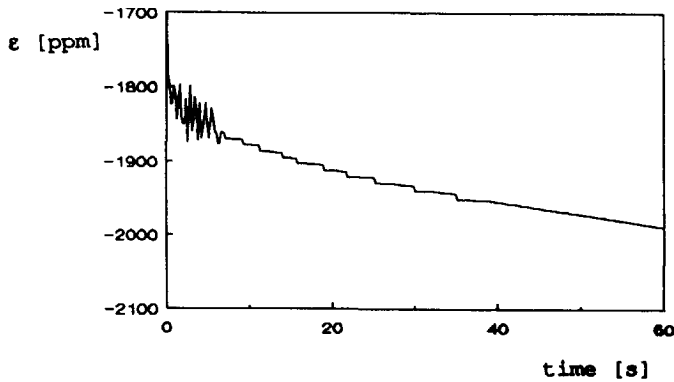


figure 5.11 Typical behaviour of the strain in $\text{Fe}_{40}\text{Ni}_{40}\text{B}_{20}$ during the first 60 seconds after removal of the stress.

During a loading experiment an important part of the observed length changes is due to creep (about 1000 ppm). The isotherms were corrected for creep but it is reasonable that these large corrections enhance the inaccuracy (about 100 ppm instead of 50 ppm). For the 3.2 MPa isotherms the creep contribution is limited to 20 ppm. This means that the accuracy in ϵ_{an} is 120 and 70 ppm for the loading and unloading isotherms, respectively.

In figure 5.12 the isothermal change of the anelastic strain is plotted during loading and unloading experiments at 578 K. After an unloaded preanneal at 578 K, which is sufficient to obtain CSRO equilibrium, the applied stress was cycled between 161.5 MPa and 3.2 MPa (resp. even and odd numbers). The isotherms were corrected for length changes due to creep, the annihilation of flow defects (for both see ref. [18]) and the elastic strain.

In table 5.3 the experimental details of the series of figure 5.12 are given. In this table the applied stress σ , the annealing time and temperature, the reduced free volume at the beginning of each cycle and

the observed elastic strain are given. The change in ϵ_{el} due to changes in Young's modulus is too small (2%) to be observed.

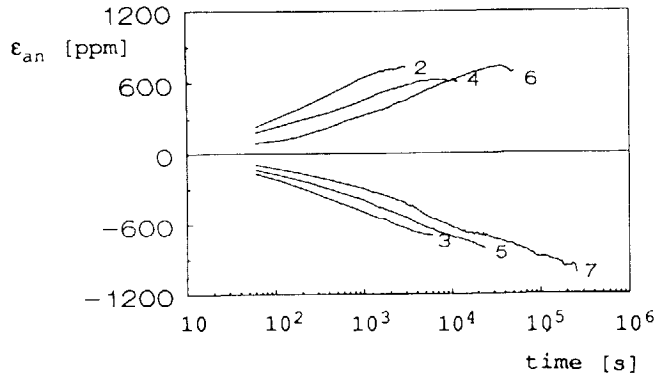


figure 5.12 Isothermal changes of the anelastic strain in $\text{Fe}_{40}\text{Ni}_{40}\text{B}_{20}$ due to cycling the applied stress between 161.5 MPa (even numbers) and 3.2 MPa (odd numbers).

TABLE 5.3

Experimental details of the anelastic strain experiment

number	treatment	T [K]	t [s]	σ [MPa]	x	ϵ_{el} [ppm]
1	preanneal	578	1200	3.2	0.07435	----
2	loaded	578	3000	161.5	0.07147	1810
3	unloaded	578	6000	3.2	0.06799	-1820
4	loaded	578	12000	161.5	0.06488	1810
5	unloaded	578	24000	3.2	0.06207	-1840
6	loaded	578	50400	161.5	0.05950	1810
7	unloaded	578	252000	3.2	0.05705	-1780

As predicted, the kinetics of ordering indeed slows down. This is visible in figure 5.12, where each isotherm is, with respect to the forgoing one, shifted along the time axis in the positive direction. This is in qualitative agreement with the experiments presented by Leusink *et al.* [18]. As pointed out earlier, a more quantitative test can be carried out by

plotting the anelastic strain versus $c_d \cdot t$. This has been done in figure 5.13, where $c_d = c_f$ (figure 5.13.a) and $c_d = \sqrt{c_f}$ (figure 5.13.b) are tried. It is demonstrated that only in the latter case the curves coincide within the experimental error.

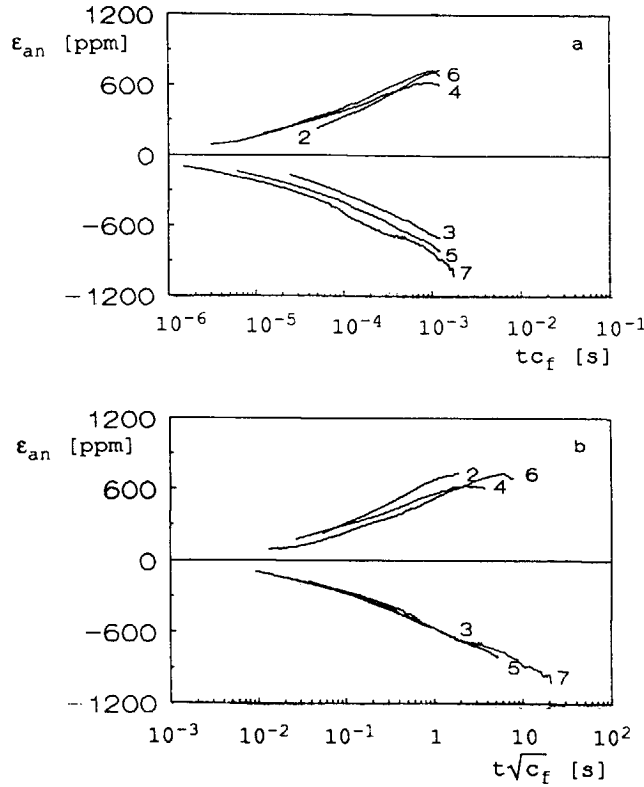


figure 5.13 The anelastic strain data from figure 5.13, now plotted on the modified time scale $t \cdot c_f$ (a) and $t \sqrt{c_f}$ (b).

5.2.2 Pd₄₀Ni₄₀P₂₀

PdNiP metallic glasses are known to be relatively stable [19]. It is possible to attain equilibrium during annealing at temperatures close to the glass transition temperature for both CSRO and TSRO. Therefore, reversible behaviour for both CSRO and TSRO has been reported for these metallic glasses (see chapter 6).

The equilibrium state in amorphous PdNiP is characterised by an amount of reduced free volume x_e . In the free volume theory it is suggested that x_e can be expressed by $x_e = (T - T_0)/B$ [20,21], where B and T_0 are constants. From an analysis of our PdNiP data $B = 6600$ K and $T_0 = 355$ K were found (see chapter 6).

In this section v^2 experiments will be presented to investigate the change in ordering kinetics due to changes in the amount of free volume in PdNiP. The as quenched samples were first equilibrated at 555 K (1), about 30 K below the glass transition temperature. Then the temperature was changed to 475 K (2) and the sample was annealed for a time sufficiently long to obtain equilibrium chemical order. Subsequently the sample was equilibrated at 575 K (3), which means that free volume will be *produced*. After attaining equilibrium at 575 K, the sample was again annealed at 475 K (4). During the whole experiment Young's modulus was measured as a function of the annealing time, as presented in figure 5.14.

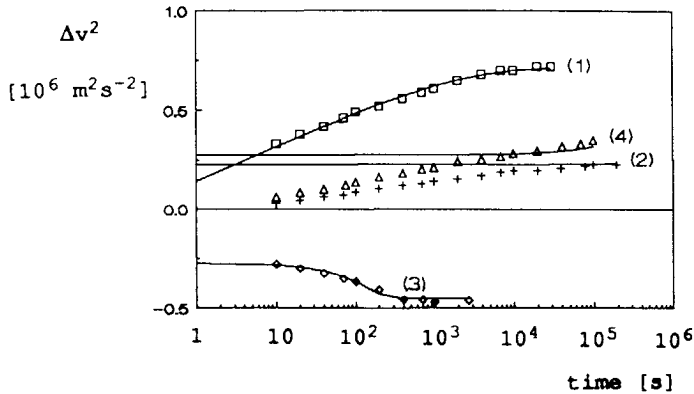


figure 5.14 Isothermal change of v^2 in $\text{Pd}_{40}\text{Ni}_{40}\text{P}_{20}$ during subsequently annealing at 555 K (\square), 475 K ($+$), 575 K (\diamond) and 475 K (\triangle).

All isotherms, with the exception of (3), show an increase in v^2 , due to chemical ordering and free volume annihilation. Isotherm (3) shows a decrease due to chemical disordering and the production of free volume. The solid lines in this figure describe the calculated effect of annihilation or production of free volume during the annealing treatments. The parameters used for these calculations will be presented in chapter 6.

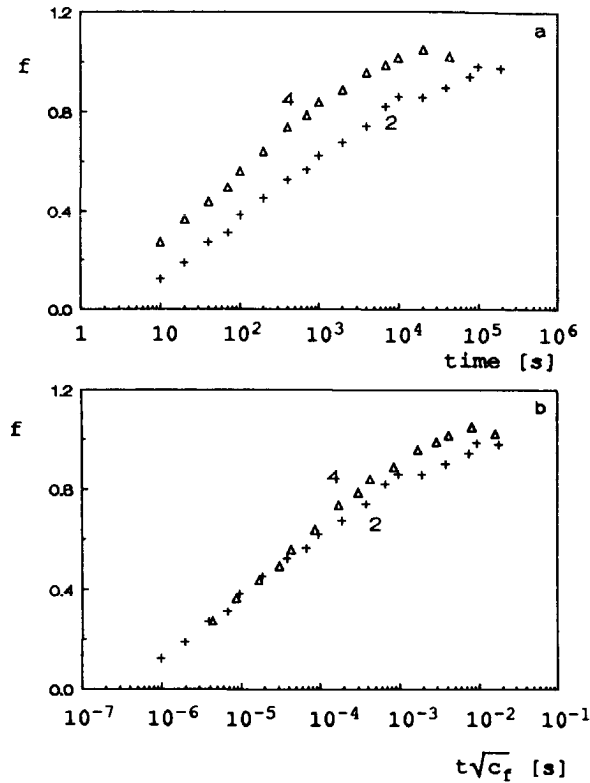


figure 5.15 Fractional isothermal change of v^2 , after subtracting the contribution due to free volume annihilation, during annealing at 475 K. The symbols (+) and (Δ) represent curve 2 and 4 of figure 5.14.

From the observed change in v^2 the CSRO contribution can be isolated, as described previously for $\text{Fe}_{40}\text{Ni}_{40}\text{B}_{20}$. Because of the different state of chemical order after the equilibration anneal, resp. at 555 K and 575 K, the change in v^2 due to chemical ordering is different for the two isotherms at 475 K. In figure 5.15.a the fractional change in v^2 is plotted versus the logarithm of time. It is clear that the fractional change of the modulus increases more rapidly, which means that ordering goes faster for the sample equilibrated at 575 K than for the samples, equilibrated at 555 K. This is due to the larger amount of free volume than in the 555 K sample. A remarkable difference with the

measurements on $\text{Fe}_{40}\text{Ni}_{40}\text{B}_{20}$ is that isotherm 4 in figure 5.15 was measured *after* isotherm 2. The faster kinetics of isotherm 4 indicate that indeed the amount of free volume has increased during the series of annealing treatments.

In figure 5.15.b the isotherms of figure 5.15.a are replotted on the modified time scale $t \cdot c_d$, where $c_d = \sqrt{c_f}$. Again this indicates that $c_d \propto \sqrt{c_f}$. Therefore, this result is in agreement with the data on $\text{Fe}_{40}\text{Ni}_{40}\text{B}_{20}$ discussed in section 5.2.1.

5.2.3 Scaling diffusion coefficient and viscosity

The behaviour of the diffusion coefficient D and the viscosity η during structural relaxation has been recently analysed by van den Beukel [13,22] in order to verify the validity of the Stokes-Einstein relation. The main results are summarized in this section.

Recently Horvath and Mehrer [23] presented very accurate measurements of ^{59}Fe tracer diffusion in $\text{Fe}_{40}\text{Ni}_{40}\text{B}_{20}$. During isothermal annealing they observed a continuous decrease of D due to structural relaxation. The reported error for the diffusion coefficient was 5%.

The most complete set of isothermal data reported were taken at 593 K. The data are given in table 5.4. Because the presented diffusion data are time averaged diffusion coefficients, $t_a/2$ is used for the time scale, with t_a the annealing time. In the same table the calculated value of η at 593 K, derived from viscosity measurements reported by van den Beukel *et al.* [12], is given. The estimated error for these viscosity values is about 5%.

For the viscosity and the diffusion coefficient the free volume theory [1] yields expressions of the form $\eta \propto (c_f k_f)^{-1}$ and $D \propto c_d k_d$ where $k_f \propto \exp(-E_f/RT)$ and $k_d \propto \exp(-E_d/RT)$. If the relation $c_d = c_f$ holds, it should be found that ηD is constant at constant temperature. If, like suggested in previous sections, $c_d \propto \sqrt{c_f}$, ηD^2 should be constant.

TABLE 5.4

Diffusion [23] and viscosity [12] data and the calculated ηD and ηD^2 .

$t_a/2$ [s]	D [$10^{-22} \text{m}^2 \text{s}^{-1}$]	η [10^{14}Nsm^{-2}]	ηD [10^{-8}N]	ηD^2 [$10^{-30} \text{Nm}^2 \text{s}^{-1}$]
1800	19.6	0.47	9.3	180.5
3600	14.0	0.90	12.6	176.4
7200	10.2	1.75	17.9	182.0
14400	7.3	3.46	25.2	184.4
27000	5.3	6.44	34.1	180.9

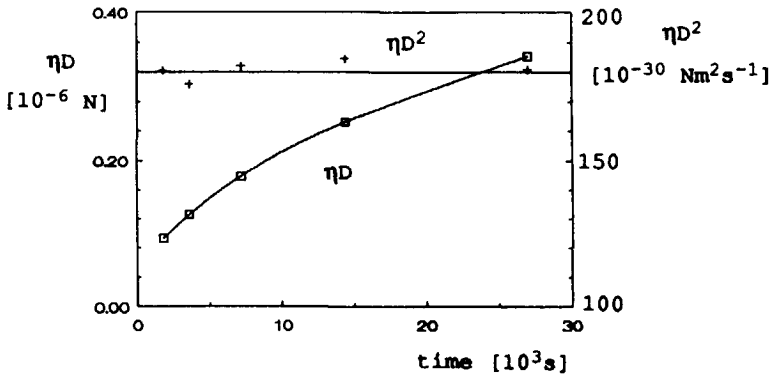


figure 5.16 ηD and ηD^2 for $\text{Fe}_{40}\text{Ni}_{40}\text{B}_{20}$ during annealing at 593 K, as a function of the annealing time.

In table 5.4 both products ηD and ηD^2 at 593 K, as presented by van den Beukel [13], are given. In figure 5.16 ηD and ηD^2 are both plotted versus the annealing time. Both table 5.4 and figure 5.16 show that ηD increases by a factor 3.5 during the annealing whereas ηD^2 remains, within the experimental accuracy, constant. This means that the Stokes-Einstein relation does not hold, but that

$$\eta D^2 = \text{constant.} \quad (5.6)$$

This is in agreement with our data on anelastic strain and changes in the electrical resistance and Young's modulus during chemical ordering, as discussed in the sections 5.2.1 and 5.2.2, which also strongly point to the relation $c_d \propto \sqrt{c_f}$.

These findings can be further verified on the diffusion data of Horvath and Mehrer at other temperatures. Since the free volume theory provides the time dependency of D during structural relaxation, it is possible to derive an analytical equation for the mean diffusion coefficient $\bar{D}(0, t_a)$ between $t=0$ and $t=t_a$:

$$\bar{D}(0, t_a) = \frac{\int_0^{t_a} D(t) dt}{t_a}. \quad (5.7)$$

$D(t)$ can be derived from equation (2.7), $D \propto c_d k_d$, with $k_d \propto \exp(-E_d/RT)$, and the expression $c_d \propto \sqrt{c_f}$. This yields

$$D(t) = \frac{D_0 \sqrt{c_{f0}} \exp(-E_d/RT)}{\sqrt{\{1 + C_0 c_{f0} t \exp(-E_f/RT)\}}}, \quad (5.8)$$

where D_0 is a constant. Then $\bar{D}(0, t_a)$ is given by

$$\bar{D}(0, t_a) = \frac{2A_0}{\alpha t_a} \{ \sqrt{1 + \alpha t_a} - 1 \}, \quad (5.9)$$

where $A_0 = D_0 \sqrt{c_{f0}} \exp(-E_d/RT)$ and $\alpha = C_0 c_{f0} \exp(-E_f/RT)$. This equation is exact, contrary to the approximated equation

$$\bar{D}(0, t_a) = \frac{D_0}{\sqrt{1 + \alpha t_a}} \quad (5.10)$$

used by van den Beukel [13]. Fitting equation (5.9) to two sets of isothermal diffusion data (593 and 613 K, without preannealing) yields $D_0 = 40585 \text{ m}^2\text{s}^{-1}$. Now the mean diffusion coefficient after every isothermal annealing treatment can be calculated for which $E_d = E_f$ is assumed. The results are plotted in figure 5.17. The calculated diffusion coefficients are presented by solid lines in the case of more than one point at one temperature, or by a symbol (+). The difference is about 10% on the average and in view of the accuracy of the diffusion measurements, this can be considered satisfactory.

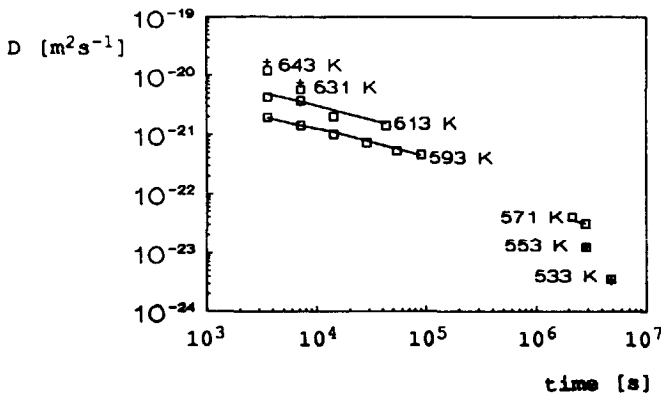


figure 5.17 The diffusion coefficient in $\text{Fe}_{40}\text{Ni}_{40}\text{B}_{20}$ during isothermal annealing at several temperatures. (\square) represents the data given in [23], the lines and (+) represent the diffusion coefficient, calculated with eq. (5.9).

5.3 Discussion

From the above presented results it can be concluded that diffusion is controlled by diffusion defects, the concentration of which is related to the concentration of flow defects by $c_d \propto \sqrt{c_f}$. This means that diffusion defects differ from flow defects but their concentrations are related. The concentration of flow defects for as quenched $\text{Fe}_{40}\text{Ni}_{40}\text{B}_{20}$ samples is $1.7 \cdot 10^{-6}$. The relation between the concentration of both types of defects gives rise to the idea that also the kinetics of annihilation of both defects must be comparable. The second order kinetics for c_f implies third order kinetics for c_d .

An interesting question is: what makes a defect a flow or diffusion defect? The relation between flow and diffusion defect concentrations suggests that they are closely related. A simple picture for diffusion defects and flow defects might be that the critical free volume needed for diffusion is smaller than that for flow and that, for instance, a cluster of diffusion defects makes a flow defect.

Defects in amorphous materials have also been a subject of computer physicists. Srolovitz *et al.* [24] constructed a computer model of an amorphous pure metal and they defined defects as regions in which the stress and symmetry parameter deviates significantly from its average

value. Two types of defects could be classified: (i) positive (p-type defects) and negative (n-type defects) local density fluctuations (fluctuations from the average density of $\pm 10\%$ were found); and (ii) regions of high shear stresses and deviations from spherical symmetry (τ -type defects). Defects of pairs of p-type and n-type defects separated by regions of large shear stresses were also common. About 5% of the atoms in the model contributed to p- and n-type defects, divided equally for both types, and 6% of the atoms satisfied the conditions for τ -type defects.

It is tempting to identify the diffusion resp. flow defects with the p and n resp. τ defects. Both p and n defects act as diffusion defects and when the concentrations of both defects are equal, $c_p = c_n = 1/2 c_d$. The probability of finding a p-n pair is then proportional to $c_p c_n \propto c_d^2$. If most of the τ defects are related to a p-n pair, the concentration $c_\tau = c_f \propto c_d^2$.

The change in defect concentration during structural relaxation can be caused by a recombination of p- and n-type defects. During this recombination also the concentration of τ defects decreases. However, in this picture the second order kinetics of flow defect annihilation is not clear.

Another problem in this interpretation is the concentration of defects, which was found to be much larger than is expected from our analysis. This can be due to the definition of the defects, used by the Srolovitz *et al.*

Recently Limoge and Brebec [26] presented the 'Diffusional Creep' model to describe atomic migration in amorphous materials. The presented mechanism is comparable to Nabarro-Herring [27,28] or Coble [29] creep in crystalline materials. The authors postulate the existence of local highly ordered non-crystalline 'grains' of size d , which grow in time according to $d^2 = d_0^2(1 + \kappa t)$, where d_0 is the initial 'grain size' and κ is a constant ('grain-boundary' mobility). The viscosity is then given by

$$\eta = \frac{kTd^2}{\beta D_{\text{eff}}\Omega}, \quad (5.11)$$

where β is a constant (related to the number of nearest neighbours) and $D_{\text{eff}} = D_{\text{vol}} + \frac{\delta}{d} D_{\text{gb}}$ with D_{vol} and D_{gb} resp. the volume and grain boundary diffusion coefficient and δ the width of the grain boundary ($\sim 5 \text{ \AA}$).

The presented model describes the change of the diffusion coefficient during annealing well. For small grains the diffusion

coefficient will change by the changing contribution of D_{gb} . At large values of d the diffusion coefficient will saturate to D_{vol} and become constant, as observed in the experiments. In the free volume theory the latter phenomenon is ignored because a constant diffusion coefficient is observed after long annealing times where crystallisation possibly influences the results.

The behaviour of the viscosity can also be described by this model. A linear increase with time is found for large grains. It also explains the change in activation energy for viscosity from 250 to 304 kJ/mole as observed in isoconfigurational experiments. For very small grains the viscosity is inversely proportional to D_{gb} , the activation energy of which is assumed to be 250 kJ/mole. For large grains the viscosity mainly depends on D_{vol} , with an assumed activation energy of 304 kJ/mole. The behaviour of η versus $1/T$ for large grains can also be described by this model when the activation energy for grain growth is the same as the one for D_{gb} .

This diffusional creep model has also some negative marks. Van den Beukel *et al.* [12] have reported isoconfigurational viscosity changes in $Fe_{40}Ni_{40}B_{20}$. These viscosities can be used to calculate the grain sizes during each isoconfigurational run. This has been performed, using equation (5.8) to calculate the diffusion coefficient in eq. (5.11). The kinetics of grain growth can thus be obtained for the isothermal runs between the isoconfigurational cycles, resulting in an activation energy for grain growth of 75 kJ/mole instead of the 250 kJ/mole predicted by the model.

Further, the activation energy for diffusion of Fe in amorphous $Fe_{40}Ni_{40}B_{20}$ was observed to be 231 kJ/mole [23] and not 304 kJ/mole suggested for the activation energy of D_{vol} for large grains.

For small grains, a non-linear dependence of time for the viscosity is expected from formula (5.11). In that case $\eta \sim d^3 \sim (1 + kt)^{3/2}$. This is not observed in the experiments.

Limoge *et al.* suggest in their paper that D_{eff} for $Fe_{40}Ni_{40}B_{20}$ is given by Horvath and Mehrer [23]. This means that when ηD , as given in table 5.4, is plotted versus the annealing time, a straight line should be observed, because d^2 is linear with time. In figure 5.16 it is shown that this is not the case.

A fundamental question in the 'Diffusional Creep' model is what is meant by a "grain" in the amorphous structure. In another paper [30],

Limoge *et al.* have suggested that grains in amorphous materials should be considered as ordered non-crystalline regions and the zones between these regions behave like grain boundaries in crystals. An alternative possibility, as reported for instance by Piller and Haasen [31], is phase separation in the amorphous structure. These precipitates could act as "grains".

5.4 Conclusions

In this chapter it is shown that the kinetics of ordering, which is a diffusion process, slows down when the concentration of flow defects c_f decreases. The rate of chemical ordering and stress induced ordering is controlled by diffusion defects, the concentration of which, c_d , is proportional to $\sqrt{c_f}$. It is demonstrated that diffusion and viscosity scale as $\eta D^2 = \text{constant}$ at constant temperature, which is in agreement with the relation between the concentration of diffusion defects and flow defects.

References

- 1 F. Spaepen, Physics of Defects, in Les Houches Lectures XXXV, eds. J.J. Poirier and M. Kleman, North Holland, Amsterdam 1981, p. 136.
- 2 D. Akhtar, B. Cantor and R.W. Cahn, *Acta Metall.* **30**, 1571 (1982).
- 3 J. Horvath, K. Pfahler, W. Ulfert, W. Frank and H. Kronmuller, *Mat. Sci. Forum* **15-18**, 523 (1987).
- 4 K. Pfahler, J. Horvath, W. Frank and H. Mehrer in *Proc. 5th Int. Conf. on Rapidly Quenched Metals*, Würzburg, 1984, eds. S. Steeb and H. Warlimont, North-Holland Physics Publishing, Amsterdam 1985, p. 755.
- 5 J. Horvath, K. Freitag and H. Mehrer in *Proc. 5th Int. Conf. on Rapidly Quenched Metals*, Würzburg, 1984, eds. S. Steeb and H. Warlimont, North-Holland Physics Publishing, Amsterdam 1985, p. 751.
- 6 R.W. Cahn, J.E. Evetts, J. Patterson, R.E. Somekh and C. Kenway Jackson, *J. Mat. Sci.* **15**, 702 (1980).
- 7 P. Valenta, K. Maier, H. Kronmuller and K. Freitag, *Phys. Stat. Sol. (b)* **106**, 129 (1981).
- 8 P. Valenta, K. Maier, H. Kronmuller and K. Freitag, *Phys. Stat. Sol. (b)* **105**, 537 (1981).

- 9 A.L. Greer, C.-J. Lin and F. Spaepen in Proc. 4th Int. Conf. on Rapidly Quenched Metals, Sendai, 1981, eds. T. Masumoto and K. Suzuki, Japan Inst. Met., Sendai, 1982, p. 567.
- 10 H.S. Chen, L.C. Kimerling, J.M. Poate and W.L. Brown, Appl. Phys. Lett. 32, 461 (1978).
- 11 J. Bøttiger, K. Dyrbye, K. Pampus, B. Thorp and P.H. Wiene, Phys. Rev. B 37, 9951 (1988).
- 12 A. van den Beukel, E. Huizer, A.L. Mulder and S. van der Zwaag, Acta Metall. 34, 483 (1986).
- 13 A. van den Beukel, Isr. Journ. Techn. 24, 101 (1989).
- 14 C.A. Volkert and F. Spaepen, Scripta Metall. et Mater. 24, 463 (1990).
- 15 A. van den Beukel, S. van der Zwaag and A.L. Mulder, Acta Metall. 32, 1895 (1984).
- 16 G. Hygate and M.R.J. Gibbs, J. Phys.: Condens. Matter 2, 1425 (1990).
- 17 G. Riontino and M. Baricco, Phil. Mag. B 61, 715 (1990).
- 18 G.J. Leusink and A. van den Beukel, Acta Metall. 36, 3019 (1988).
- 19 H.W. Kui, A.L. Greer and D. Turnbull, Appl. Phys. Lett. 45, 615 (1984).
- 20 M.H. Cohen and D. Turnbull, J. Chem. Phys. 31, 1164 (1959).
- 21 F. Spaepen, Acta Metall. 25, 407 (1977).
- 22 A. van den Beukel, Scripta Metall. 22, 877 (1988).
- 23 J. Horvath and H. Mehrer, Cryst. Latt. Def. and Amorph. Mat. 13, 1 (1986).
- 24 D. Srolovitz, K. Maeda, V. Vitek and T. Egami, Phil. Mag. A 44, 847 (1981).
- 25 K. Maeda and S. Takeuchi, J. Phys F: Metal Phys. 8, L283 (1978).
- 26 Y. Limoge and G. Brebec, Acta Metall. 36, 665 (1988).
- 27 F.R.N. Nabarro, Rep. Conf. on Strength of Solids, Phys. Soc. London (1948), p. 75.
- 28 C. Herring, J. Appl. Phys. 21, 437 (1950).
- 29 R.L. Coble, J. Appl. Phys. 34, 1679 (1963).
- 30 Y. Limoge, G. Brebec and Y. Adda in DIMETA-82: Diffusion in Metals and Alloys, Proc. Int. Conf., Tihany, 1982, eds. F.J. Kedves and D.L. Beke, Diffusion and Defects Monographs Series 7, 285 (1983).
- 31 J. Piller and P. Haasen, Acta Metall. 30, 1 (1982).

CHAPTER 6

STRUCTURAL RELAXATION IN AMORPHOUS $\text{Pd}_{40}\text{Ni}_{40}\text{P}_{20}$

6.1 Introduction

Due to the very fast cooling during the production process metallic glasses are normally very far from the metastable equilibrium state (chapter 2). During annealing at temperatures at which the atomic mobility is fast enough, the glass will relax towards equilibrium. However, in most of the metallic glasses crystallisation interferes with this relaxation process before equilibrium is reached.

A criterion for the stability of the metallic glasses is the difference between the glass transition temperature (T_g) and melting temperature (T_m) [1]. A large difference between these two temperatures means that the metallic glass is relatively stable and has the possibility to reach equilibrium.

At the moment one group of metallic glasses is known for which it is possible to reach the equilibrium glassy state before the metallic glass crystallises. This group contains alloys in which palladium is the main element. For these alloys the difference between T_g and the crystallisation temperature T_x during a linear heating experiment is often over 40 K [2], demonstrating the resistance against crystallisation.

In the past few years viscosity measurements on $\text{Pd}_{77.5}\text{Cu}_6\text{Si}_{16.5}$ [3] and $\text{Pd}_{40}\text{Ni}_{40}\text{P}_{19}\text{Si}_1$ [4] metallic glasses near the glass transition temperature have been reported. The results for both alloys could be interpreted by the assumption that equilibrium was reached. The most convincing experiments have been reported by Volkert and Spaepen [4]. They have measured the viscosity in $\text{Pd}_{40}\text{Ni}_{40}\text{P}_{19}\text{Si}_1$ during annealing at 573 K after preannealing at resp. 563 K and 593 K. The reported glass transition temperature for this metallic glass was 575 K. Their results are plotted in figure 6.1, in which also the viscosity for an as quenched sample is given. In this figure it is clearly demonstrated that a constant viscosity for all samples was reached after about 6 hours annealing, which means that the metallic glass remained in equilibrium at 573 K for at least 4 hours.

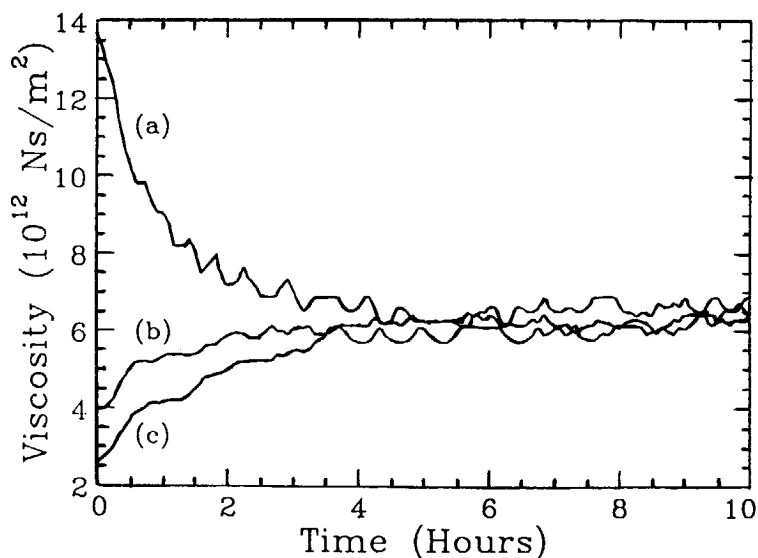


figure 6.1 Change of the viscosity of $\text{Pd}_{40}\text{Ni}_{40}\text{P}_{19}\text{Si}_1$ during annealing at 573 K for (a) a sample equilibrated at 563 K, (b) a sample equilibrated at 593 K and (c) an as quenched sample [4].

In this chapter structural relaxation data on amorphous $\text{Pd}_{40}\text{Ni}_{40}\text{P}_{20}$, obtained by Young's modulus measurements, will be presented. The results will be analysed in terms of the mixed model presented in chapter 2. The stability of the metallic glass used for this study is demonstrated in figure 6.2. In this figure the change of the internal energy, as measured by DSC, is shown. The difference between T_g and T_x is about 40 K, which suggests a strong resistance against crystallisation.

6.2 Kinetics of defect annihilation and production

In previous work on $\text{Fe}_{40}\text{Ni}_{40}\text{B}_{20}$, e.g. [5], as summarised in chapter 2, it was demonstrated that structural relaxation can be separated into two processes. One of these processes is the annihilation of flow defects.

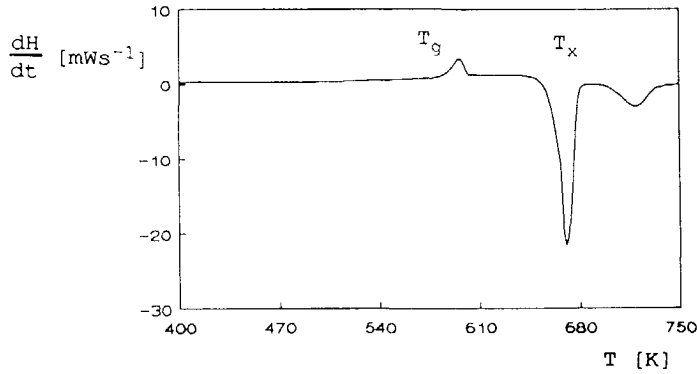


figure 6.2 DSC experiment for a $\text{Pd}_{40}\text{Ni}_{40}\text{P}_{20}$ metallic glass. The heating rate was 20 K/min.

In the free volume model the viscosity η is related to the concentration of flow defects c_f by $\eta \propto (c_f k_f)^{-1}$, with k_f a temperature dependent rate constant. Since the viscosity for an as quenched metallic glass increases linearly with time during annealing if the glass is far from equilibrium, the kinetics of flow defect annihilation is given by a second order rate equation:

$$\frac{dc_f}{dt} = -k_f c_f^2. \quad (2.6)$$

In this equation $c_f = \exp(-1/x)$, where x is the reduced free volume, and k_f is a constant ($= C_0 \exp(-E_f/RT)$, where C_0 is a constant and E_f is the activation energy for flow defect annihilation).

Eq. (2.6) says that for very long annealing times c_f will become zero. However, since the system in equilibrium has a finite viscosity η_{eq} , the concentration of flow defects must reach an equilibrium value not equal to zero. Therefore eq. (2.6) should be changed in order to account for the equilibrium concentration $c_{f,eq}$.

Previously it was found that the equilibrium viscosity, η_{eq} , depends on the annealing temperature [4]. Fulcher [6] and Vogel [7] have empirically established that the temperature dependence of the equilibrium viscosity can be described by

$$\eta_{eq} = \eta_0 \exp\left(\frac{B}{T - T_0}\right), \quad (2.9)$$

where η_0 , B and T_0 are constants. Interpretation of equilibrium viscosity in terms of the equilibrium concentration of flow defects results in

$$c_{f,eq} = \exp\left(-\frac{B}{T-T_0}\right). \quad (2.10)$$

The change in concentration of flow defects can be considered as a competition between production and annihilation. The annihilation of flow defects can be established experimentally far from equilibrium, which led to the second order kinetics of eq. (2.6). The production, on the other hand, has never been measured far from equilibrium, which leaves several possibilities for the overall equation for dc_f/dt . We will now discuss three of these possibilities.

If production occurs at random positions in the amorphous material the rate of change of the concentration of flow defects is given by

$$\frac{dc_f}{dt} = -k_f c_f^2 + k_p P, \quad (6.1)$$

where P is a constant and k_p is the rate constant for production. When equilibrium is attained the net change in c_f is zero, and c_f equals $c_{f,eq}$, which leads to

$$\frac{dc_f}{dt} = -k_f(c_f^2 - c_{f,eq}^2). \quad (6.2)$$

The dependence of c_f on the annealing time then becomes, with $c_{f,0}$ is c_f at $t=0$:

$$c_f(t) = c_{f,eq} \left\{ \frac{c_{f,0} + c_{f,eq} + (c_{f,0} - c_{f,eq}) \exp(-2c_{f,eq} k_f t)}{c_{f,0} + c_{f,eq} - (c_{f,0} - c_{f,eq}) \exp(-2c_{f,eq} k_f t)} \right\}, \quad (6.3)$$

if $c_{f,0}$ is larger than $c_{f,eq}$, and

$$c_f(t) = -c_{f,eq} \left\{ \frac{c_{f,eq} - c_{f,0} - (c_{f,0} + c_{f,eq}) \exp(2c_{f,eq} k_f t)}{c_{f,eq} - c_{f,0} + (c_{f,0} + c_{f,eq}) \exp(2c_{f,eq} k_f t)} \right\} \quad (6.4)$$

if $c_{f,0}$ is smaller than $c_{f,eq}$.

Another possibility is that the production of flow defects occurs at flow defects, in which case the rate of change of the flow defect concentration is described by

$$\frac{dc_f}{dt} = -k_f c_f^2 + k_p c_f S. \quad (6.5)$$

In this case S is equal to $(k_f/k_p)c_{f,eq}$, as can be derived under the same conditions as previously for P , and

$$\frac{dc_f}{dt} = -k_f c_f (c_f - c_{f,eq}). \quad (6.6)$$

This means that

$$c_f(t) = \frac{c_{f,eq} c_{f,0}}{c_{f,0} - (c_{f,0} - c_{f,eq}) \exp(-c_{f,eq} k_f t)}. \quad (6.7)$$

Tsao and Spaepen [3] described an annihilation and production mechanism in which the number of sites at which annihilation or production of flow defects occurs, depends on the excess number of defects, $(c_f - c_{f,eq})$. The rate equation for annihilation or production of flow defects is then given by

$$\frac{dc_f}{dt} = -k_f |c_f - c_{f,eq}| (c_f - c_{f,eq}) \quad (6.8)$$

or

$$c_f = c_{f,eq} + \frac{c_{f,0} - c_{f,eq}}{1 + |c_{f,0} - c_{f,eq}| k_f t}. \quad (6.9)$$

The above presented equations will be used to describe the part of the structural relaxation due to changes in the flow defect concentration in amorphous $\text{Pd}_{40}\text{Ni}_{40}\text{P}_{20}$. The first aim is to describe structural relaxation in $\text{Pd}_{40}\text{Ni}_{40}\text{P}_{20}$ by the mixed model of chapter 2. Moreover, it will be tried to discriminate between the three presented equations that describe the annihilation and production of flow defects.

Tsao and Spaepen [3] and Volkert and Spaepen [4] have tried to describe the effect of the concentration of flow defects on the viscosity for $\text{Pd}_{77.5}\text{Cu}_6\text{Si}_{16.5}$ and $\text{Pd}_{40}\text{Ni}_{40}\text{P}_{19}\text{Si}_1$ metallic glasses, respectively. Tsao and Spaepen [3] concluded that the annihilation of flow defects can be rather well described with eq. (6.8). The production

of flow defects could be described with the same equation. However, they also used the unimolecular equation, $dc_f/dt = -k_f(c_f - c_{f,eq})$, to fit the data. They concluded that the best fit of the production data was obtained with this latter equation. The quality of the fit to equation (6.6) was intermediate between that of the other two equations. Therefore, they concluded that it is unlikely that fitting all data sets to equation (6.6) yields significant new information.

6.3 Experimental results

6.3.1 As quenched samples

Young's modulus measurements were performed with the pulse-echo method. In this method the longitudinal wave velocity v is measured, which is related to Young's modulus by $E = \rho v^2$ and ρ is the density. A description of the set-up is given in section 3.2.

The as quenched v^2 for $\text{Pd}_{40}\text{Ni}_{40}\text{P}_{20}$ was observed to be about $10.1 \cdot 10^6 \text{ m}^2\text{s}^{-2}$. If the reported density ρ for $\text{Pd}_{40}\text{Ni}_{40}\text{P}_{20}$ is used (9400 kgm^{-3}) [8,9], Young's modulus will be about 95 GPa. This is in reasonable agreement with the reported modulus for this metallic glass (98.1 GPa) [10].

In figure 6.3 the isothermal change in v^2 is plotted versus the annealing time for several annealing temperatures between 400 K and 575 K. In figure 6.3.a the low temperature isotherms are plotted. In all isotherms a continuous increase in v^2 is observed, due to both Chemical Short Range Ordering (CSRO) and Topological Short Range Ordering (TSRO). For the high temperature isotherms, as plotted in figure 6.3.b, Δv^2 becomes constant for the isotherms close to T_g (585 K), indicating that metastable equilibrium is attained. These equilibria depend on the annealing temperature.

In the isotherms in figure 6.3 no indication for a transition between CSRO and TSRO could be observed. In order to obtain information about the transition point between CSRO and TSRO, cycling experiments at lower annealing temperatures were performed to study reversible CSRO. After preannealing at 450 K during a time t_p , the temperature was changed to 480 K and the change in v^2 was measured. In figure 6.4 Δv^2 is plotted versus the annealing time for several values of t_p . For all samples v^2 decreases due to chemical disordering through

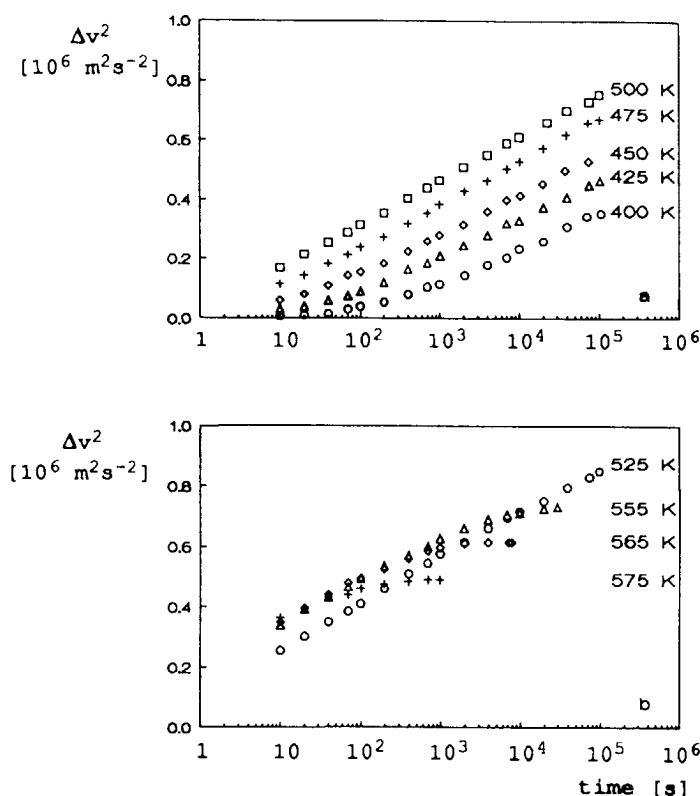


figure 6.3 Change of Young's modulus (represented by changes in v^2) for the as quenched samples during isothermal annealing at temperatures between (a) 400 K and 500 K, and (b) 525 K and 575 K.

processes that are fast enough to establish complete ordering during the preanneal. At longer times v^2 starts to increase due to chemical ordering of the slower processes and subsequent annihilation of free volume.

If the preannealing time is sufficiently long to attain equilibrium chemical order, the minimum value of Δv^2 will not change if a larger t_p is chosen. In figure 6.5 the minimum values of Δv^2 from figure 6.4 are plotted versus the preannealing time. It is shown that Δv^2 becomes constant after about 40000 seconds at 450 K. This means that after this annealing time CSRO is completed at 450 K.

From these experiments we have decided to fit the free volume effect on v^2 for the high temperature isotherms (525 K - 575 K).

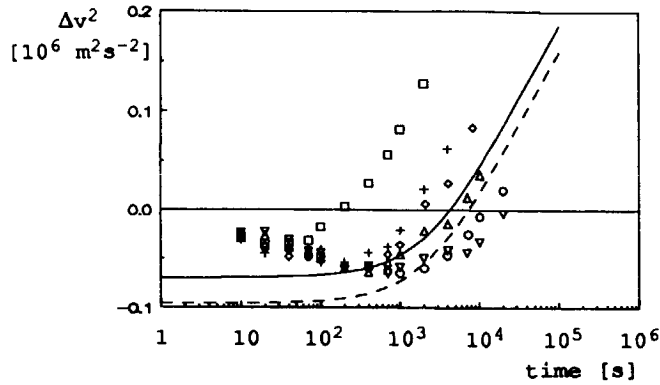


figure 6.4 Change of Young's modulus during isothermal annealing at 480 K after preannealing at 450 K during 1380 s. (\square), 10^4 s. (+), $2 \cdot 10^4$ s. (\diamond), $4 \cdot 10^4$ s. (Δ), 10^5 s. (o) and $2.5 \cdot 10^5$ s. (∇). For the solid and dashed line: see the text.

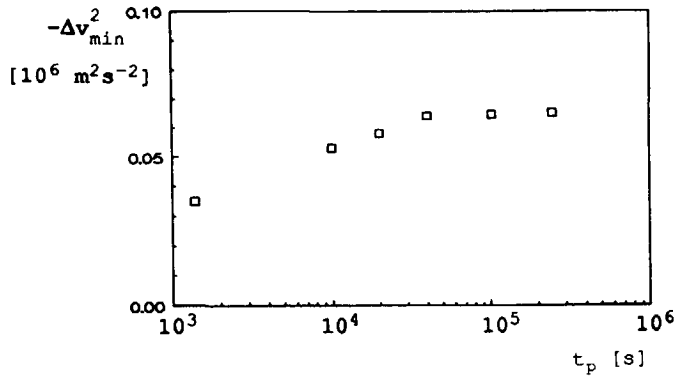


figure 6.5 The Δv^2 values of the minima in figure 6.4 plotted versus the preannealing time.

According to the time needed for complete order at 480 K and 450 K (1000 and 40000 seconds, respectively) CSRO will be completed within 10 seconds at these higher temperatures.

The equations (6.3), (6.7) and (6.9) in combination with (2.10) were fitted to the isotherms presented in figure 6.3.b. A least squares method was used to find the parameters E_f , C_0 , x_0 , B and T_0 , describing the TSRO part of the isotherms. It was assumed that $\Delta v^2 = A_E \Delta x$ [5] and A_E is a constant. For these fits the change in v^2 due to CSRO between the as quenched and equilibrium ordered state for each annealing temperature was taken as:

$$\Delta v_{CSRO}^2 = A \left(\frac{1}{T} - \frac{1}{T_f} \right), \quad (6.10)$$

where A is a constant and T_f is called the fictive temperature, representing the CSRO state of the as quenched specimen.

For the fits with the equations (6.7) and (6.9) the values of C_0 , B and T_0 were taken from Duine [11] from viscosity data in the same glass. For the fit with eq. (6.3) all parameters were varied. The parameters obtained from the fit are given in table 6.1. In this same table the parameter for goodness of fit, $D^2/(N-m)$, is also given. N is the number of data points, m is the number of fit parameters and D^2 is given by

$$D^2 = \sum_{i=1}^N \frac{(y_i - y(x_i; a_1, \dots, a_m))^2}{\sigma_i^2} \quad (6.11)$$

where y_i is the i^{th} data point, σ_i^2 is the variance in the i^{th} data point and $y(x_i; a_1, \dots, a_m)$ is the value according to the fit, with a_k the k^{th} fit parameter. For a perfect fit the expectation value for $D^2/(N-m)$ equals 1. Eq. (6.9) yields the best fit, which is in accordance with Duine's viscosity data, analysed with eqs. (6.7) and (6.9) [11] and with eq. (6.3) [12]. However, the difference between the three equations is rather small, which does not allow an unambiguous discrimination between the equations.

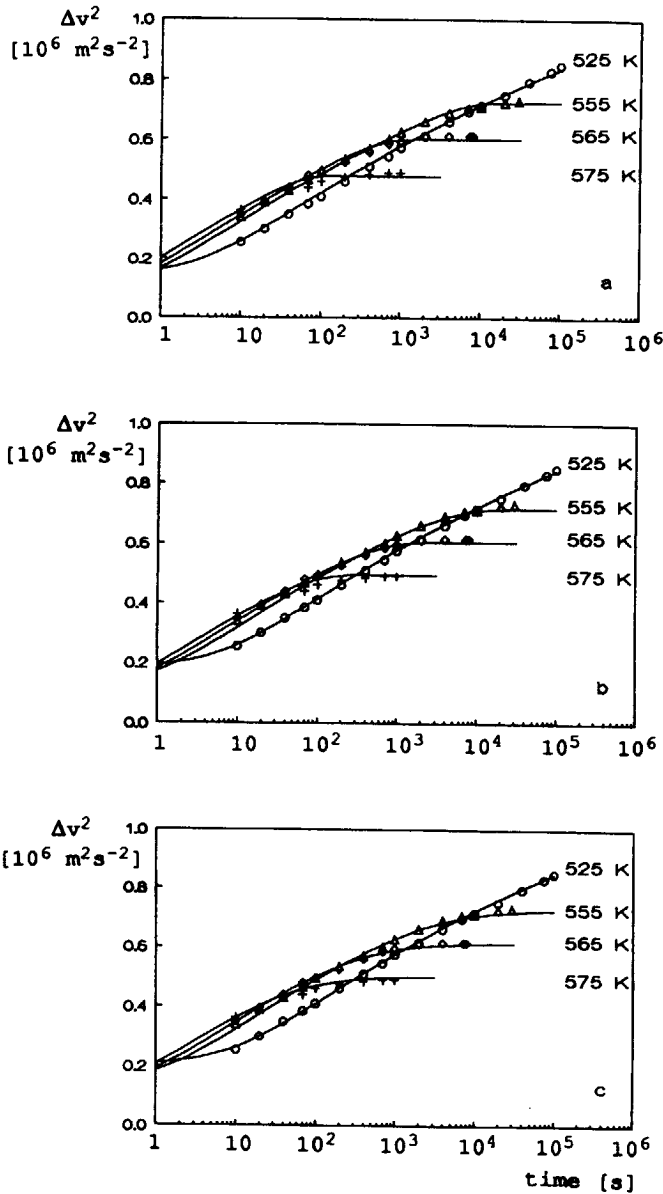


figure 6.6 Change of Young's modulus for as quenched samples during isothermal annealing between 525 K and 575 K. The solid lines represents model calculations, using (a) eq. (6.3), (b) eq. (6.7) and (c) eq. (6.9) and the corresponding parameters from table 6.1.

TABLE 6.1

Parameters obtained from the fits of the free volume annihilation equations to the high temperature isotherms of figure 6.3.b.

eq.	A	T_f	B	T_0	E_f	C_0	x_0	A_E	$\frac{D^2}{N \cdot m}$
	10^6 Km^2s^{-2}	K	K	K	kJ/mole	s^{-1}		10^6 m^2s^{-2}	
6.3	689	587	6354	376	157	$2.44 \cdot 10^{26}$	0.0384	-64.55	1.63
6.7	689	608	6600	355	158	$3.41 \cdot 10^{25}$	0.0407	-58.47	1.47
6.9	689	620	6267	361	169	$1.83 \cdot 10^{26}$	0.0415	-56.62	0.93

The value for A in eq. (6.10) is obtained from a cycling experiment which will be described in section 6.3.3 (figure 6.12). In this cycling experiment the temperature has been cycled over a wide range of temperatures (100 K). For one isotherm (isotherm 6) an initial decrease in v^2 has been measured, due to disordering, whereafter v^2 increases due to free volume annihilation. The minimum observed in this experiment gives rise to $A = 689 \cdot 10^6 \text{ Km}^2/\text{s}^2$.

The constant A can also be obtained from cycling experiments like the one presented in figure 6.4. From the minimum in Δv^2 a value for A can be obtained using the preannealing temperature for T_f . For the experiments in figure 6.4 a value for A of about $500 \cdot 10^6 \text{ Km}^2/\text{s}^2$ is obtained.

This observation means that the minimum in Δv^2 observed in figure 6.4 is too small. This can be explained by the idea that TSRO starts before CSRO is completed, resulting in a smaller effect in Δv^2 . In figure 6.4, the solid and the dashed line represent the calculated change in free volume for the sample preannealed during 40000 seconds, calculated with eq. (6.9). These lines start at a level determined by eq. (6.10) and the values $500 \cdot 10^6 \text{ Km}^2/\text{s}^2$ and $689 \cdot 10^6 \text{ Km}^2/\text{s}^2$ for the solid and the dashed line, respectively. It is shown that the data points are between these two lines and both lines describe the data equally well.

In figure 6.6 the results of the fits are shown. In these figures the solid lines represent the change in v^2 due to annihilation of flow

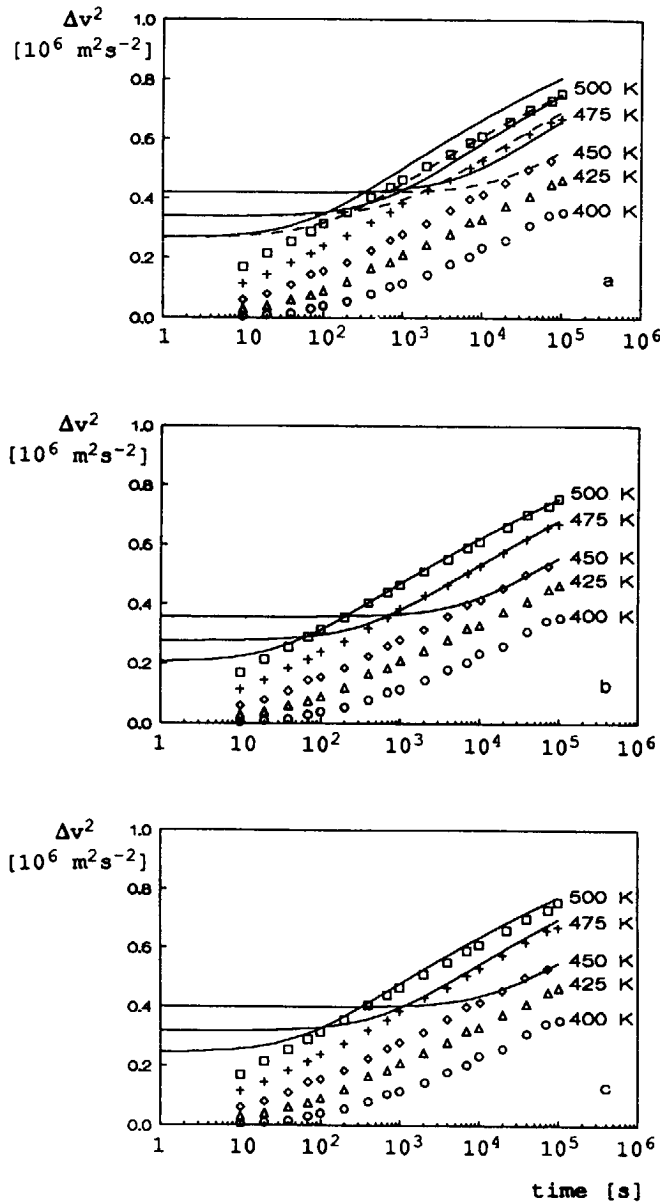


figure 6.7 Change of Young's modulus for as quenched samples during isothermal annealing between 400 K and 500 K. The lines represents model calculations, using (a) eq. (6.9), (b) eq. (6.3) and (c) eq. (6.7) and the corresponding parameters. For the difference between the solid and dashed line in (a): see text.

defects, calculated with eq. (6.3) (a), (6.7) (b) and (6.9) (c) and the corresponding parameters from table 6.1.

The parameters obtained from the fit were used to describe also the low temperature isotherms. In figure 6.7.a the low temperature isotherms of figure 6.3.a are plotted with the calculated solid lines resulting from eq. (6.9) and the corresponding parameters from table 6.1.

It turns out that the changes in v^2 , calculated with the parameters from table 6.1, are too large. This can be explained by the suggestion that the fictive temperature for CSRO or the frozen in free volume for these samples differs from those for the high temperature samples. The samples for the low temperature isotherms were taken from another part of the ribbon than the high temperature samples. Consequently, the frozen-in configuration might not be the same due to *e.g.* changes in the cooling rate. Effects of this kind have been reported in the literature. For instance, recently, the magnetic properties in an amorphous Co-based ribbon were found to vary along the first 80-100 meter [13] possibly due to variations in the cooling conditions during the first seconds of the quenching, resulting in a change of the frozen-in free volume or the fictive temperature.

For the analysis presented in this chapter the fictive temperature was kept constant and x_0 was adapted to the data points. We will come back to this choice in the discussion. The x_0 values used for the dashed lines in figure 6.7.a were 0.0405 (500 K and 475 K) and 0.0395 (450 K). The dashed line for the 450 K isotherm fits the data after about 40000 seconds, in accordance with the cycling experiments of figure 6.4.

In figure 6.7.b and 6.7.c a similar procedure was followed for eq. (6.3) and (6.7), respectively. The new x_0 values for eq. (6.3) were 0.0375 for the isotherms at 500 K and 475 K and 0.036 for the isotherms at 450 K, for eq. (6.7) the new x_0 values were 0.0395 and 0.038 respectively.

In order to test the reproducibility of the samples, a sample was taken from the part of the ribbon from which the low temperature samples had been taken, and measured at 575 K. In figure 6.8 the resulting isotherm (2) is shown together with the 575 K isotherm (1) of figure 6.3. The solid lines were calculated with eq. (6.9) and the parameters of table 6.1, but x_0 values of 0.0400 and 0.0415,

respectively. It is seen that for a good fit of the new sample indeed a lower value of x_0 is required, in agreement with what was found in figure 6.7.

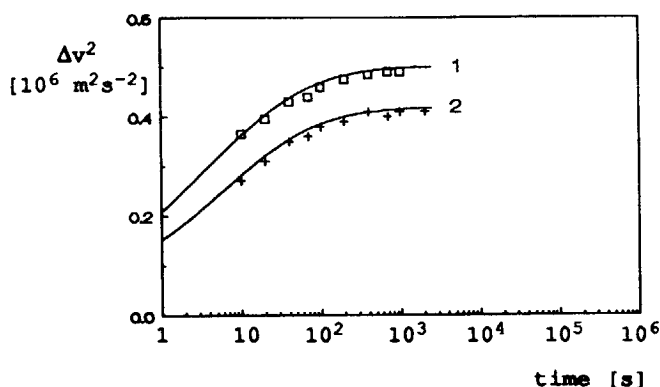


figure 6.8 Change of Young's modulus for two as quenched samples during isothermal annealing at 575 K. The sample for isotherm 2 is taken from the part of the ribbon where the low temperature as quenched samples were taken from; isotherm 1 is the same as in figure 6.3.b. The solid lines represent model calculations with eq. (6.9).

6.3.2 DSC experiments

In figure 6.2 a DSC experiment was shown where the glass transition is observed as a small endothermic peak. Recently van den Beukel and Sietsma [14] have demonstrated that the glass transition can be described as a free volume related kinetic phenomenon.

During warming up the metallic glass relaxes towards equilibrium; this means that the free volume continuously decreases, approaching its equilibrium value. This process results in the production of heat (exothermic). At a certain temperature the amount of free volume reaches the equilibrium value. Since the temperature continuously increases, from this point on the actual amount of free volume is smaller than the equilibrium value. Now the amount of free volume must increase towards equilibrium. The observed endothermic peak at the glass transition temperature is the result of the ever faster kinetics of

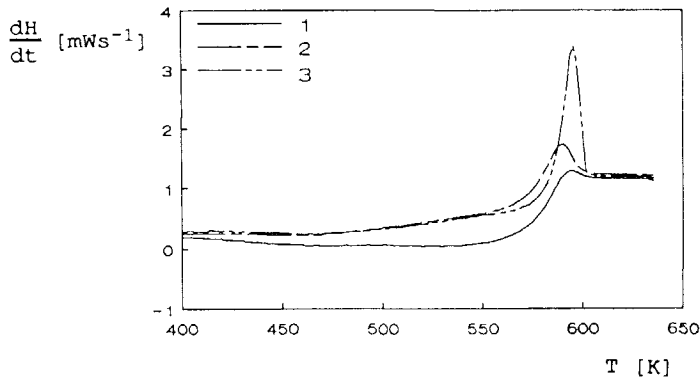


figure 6.9 Change of the internal energy for a $\text{Pd}_{40}\text{Ni}_{40}\text{P}_{20}$ metallic glass during a DSC experiment with a heating rate of 20 K/min: (1) an as quenched sample, (2) a sample preannealed during 3600 seconds at 540 K, and (3) a sample preannealed during 72000 seconds at 540 K.

production of free volume, until the production can keep up with the heating rate.

In figure 6.9 three DSC traces are shown, one for an as quenched sample and two for samples preannealed at 540 K during resp. 3600 and 72000 seconds. The samples were heated until they were completely crystalline (not shown in figure 6.9). After a first scan the samples were cooled down to room temperature and warmed up again. Since this second scan was performed with crystalline samples, no effects were measured. The second scan was subtracted from the first scan, correcting the first scan for instrumental effects. Therefore all effects shown in figure 6.9 are due to changes in the amorphous material. The endothermic peak at T_g increases strongly when the preannealing time increases. Furthermore it is found that the maximum of the endothermic peak (at 593 K for the as quenched sample) shifts to a lower temperature for the sample with $t_p=3600$ s (589 K) and back to a higher temperature for the sample with $t_p=72000$ s (595 K).

Since the nature of the glass transition is known, one can perform simulations using the free volume model to calculate the glass transition. Van den Beukel and Sietsma [14] have performed simulation

experiments to calculate DSC experiments after preannealing. They have used eq. (6.6), $dc_f/dt = -k_f c_f (c_f - c_{f,eq})$, and eq. (6.8), $dc_f/dt = -k_f |c_f - c_{f,eq}| (c_f - c_{f,eq})$, to calculate the change in free volume during a DSC experiment with and without preannealing. They concluded that only equation (6.6) describes the observed phenomena well. Eq. (6.8) shows a continuous decrease of T_g with increasing preannealing time.

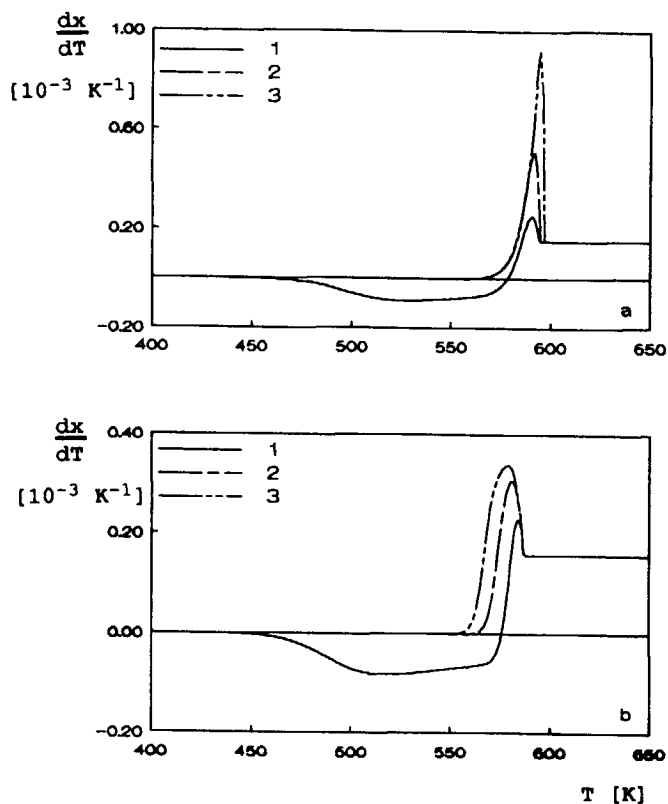


figure 6.10 Simulation of the DSC experiments presented in figure 6.9 with (a) eq. (6.6) and (b) eq. (6.2).

In figure 6.10.a the calculated DSC traces are shown for the experiments presented in figure 6.9. These traces were calculated with eq. (6.6) and the corresponding parameters from table 6.1. Although the agreement is not quantitative, the tendency of the peak shifts after preannealing is present. Also the temperature values of the maxima are

reasonable (591 K, 592 K and 596 K for as quenched, preannealed during 3600 seconds and 72000 seconds, respectively).

In figure 6.10.b simulations of the DSC experiments from figure 6.9 with eq. (6.2), $dc_f/dt = -k_f(c_f^2 - c_{f,eq}^2)$, and the corresponding parameters from table 6.1 are shown. This figure clearly demonstrates that eq. (6.2) fails in describing the DSC experiment, because T_g decreases continuously with increasing preannealing time.

Since the glass transition is determined by the production of free volume, one can conclude from these experiments and simulations that only eq. (6.6) describes the production of free volume rather well. In section 6.3 it was concluded that eq. (6.9) gives the best description of the annihilation of free volume. However, the differences between the three given equations were small for the v^2 measurements.

Since the equations were derived to describe both annihilation and production of flow defects, we must conclude that eq. (6.6) describes these two processes. In the following sections only this equation and the corresponding parameters from table 6.1 will be used.

6.3.3 Cycling experiments

In section 6.3.1 it was shown that metastable equilibrium is attained at higher temperatures. This equilibrium state of order depended on the annealing temperature and gave rise to a temperature dependent change in v^2 . Since equilibrium was reached for both CSRO and TSRO, reversible behaviour for both processes is expected during cycling experiments. If the temperature is changed to a new temperature T_a after attaining metastable equilibrium at the preannealing temperature T_p , the metallic glass will try to attain a new, metastable, equilibrium order.

In figure 6.11 the first set of cycling experiments is presented. After a preanneal at 565 K (1), the temperature was changed to 575 K (2) and Young's modulus was measured during annealing. After the preanneal both CSRO and TSRO are in equilibrium at the value corresponding to a temperature of 565 K. During annealing at 575 K chemical disordering gives rise to a decrease of v^2 , which is very fast, and so does the increase of the amount of free volume, since $c_{f,eq}$ at 575 K is larger than $c_{f,eq}$ at 565 K.

After attaining equilibrium the temperature was changed to 555 K (3) and Young's modulus was measured again until equilibrium was reached. Chemical ordering and flow defect annihilation occurred, both giving rise to an increase in v^2 .

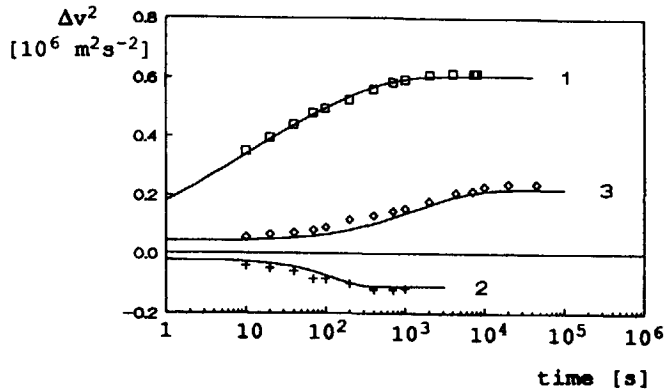


figure 6.11 Cycling experiments with a sample equilibrated at 565 K (1). The sample is subsequently annealed at 575 K (2) and 555 K (3), respectively. The solid lines in this figure are model calculations with eq. (6.7).

In figure 6.11 the solid lines represent the changes in Δv^2 due to changes in Δx as calculated with eq. (6.7) and the corresponding parameters from table 6.1. The contribution due to CSRO has been calculated with eq. (6.10), inserting the preceding temperature for T_f . The model equations describe the changes in v^2 rather well.

In figure 6.12.a the second set of cycling experiments is presented. After a first preanneal at 575 K (1), the temperature was cycled between 565 K (2), 475 K (3), 575 K (4), 475 K (5) and 555 K (6). In a schematic drawing the change in reduced free volume during these annealing treatments is given in figure 6.12.b. In this figure it is shown that both production (4) and annihilation (1,2,3,5,6) of free volume was studied during this experiment. The solid lines in figure 6.12.a represent the calculated changes due to free volume changes as described previously. The agreement with the data points is again satisfactory.

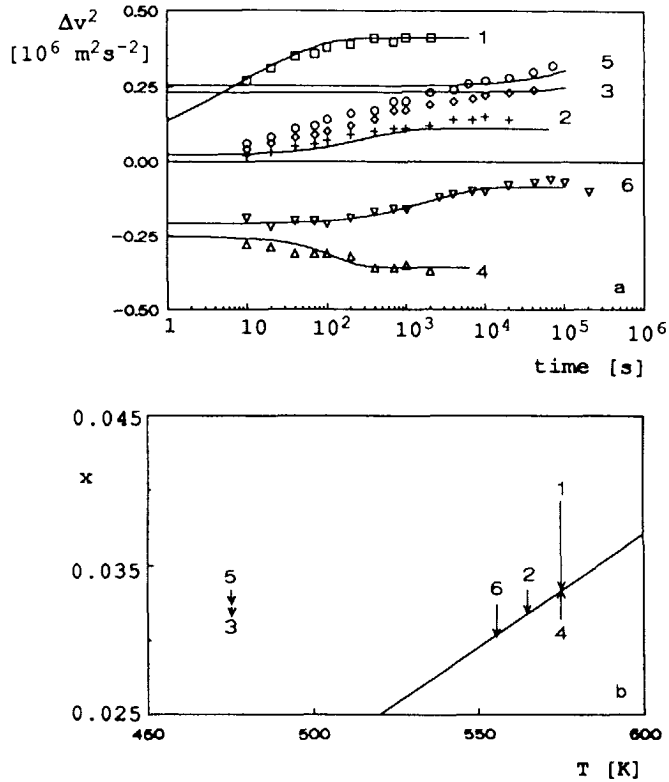


figure 6.12 a Cycling experiments with a sample equilibrated at 575 K (1). The sample is subsequently annealed at 565 K (2), 475 K (3), 575 K (4), 475 K (5) and 555 K (6), respectively. The solid lines in this figure are model calculations with eq. (6.7).

b Schematic presentation of the change in reduced free volume during the cycling experiment presented in figure 6.12.a. The metastable equilibrium is given by the thick solid line

c (next page) Fractional changes in v^2 for the pre-TSRO part of the 475 K isotherms plotted versus the annealing time.

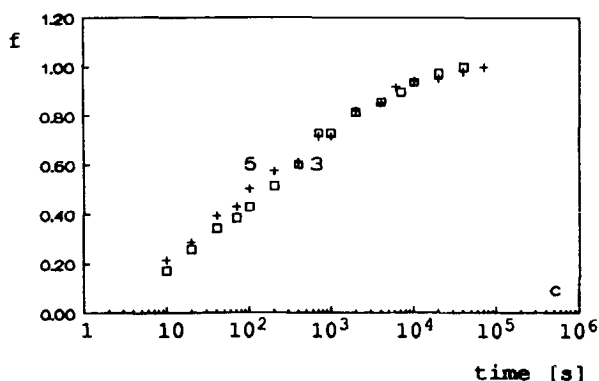


figure 6.12.c

In this experiment also the change in orderings kinetics, as described in chapter 5, was studied. In figure 6.12.a two isotherms at 475 K after preannealing at resp. 565 K (3) and 575 K (5) are plotted. Plotting the fractional changes in v^2 , due to CSRO, for the isotherms at 475 K versus the logarithm of time (fig 6.12.c), isotherm (3) is slightly slower than (5). Inserting B and T_0 for eq. (6.7) from table 6.1 in eq. (2.10) yields $\sqrt{c_{f,e}(575 \text{ K})}/\sqrt{c_{f,e}(565 \text{ K})} = 2$. The shift factor between the two isotherms of figure 6.12.c can unfortunately not be determined very accurately, mainly because the total contribution of CSRO to isotherm (5) is not reproduced well by the model calculations (see figure 6.12.a).

6.3.4 Chemical Short Range Ordering

It was demonstrated in the previous sections that the change in v^2 in as quenched $\text{Pd}_{40}\text{Ni}_{40}\text{P}_{20}$ ascribed to changes in free volume can be described with eq. (6.6), assuming that Δv^2 is linear with Δx .

The remaining part of the isotherms is due to Chemical Short Range Ordering (CSRO). At high temperatures CSRO takes place within 10 seconds, so its kinetics cannot be measured. In figure 6.13 the CSRO part for the low temperature isotherms (400-500 K) is plotted versus the annealing time. The isotherms for 425 K and 400 K do not saturate because annealing during 10^5 seconds at these temperatures was not sufficient to reach complete CSRO. The other isotherms do saturate after a period that depends on the temperature.

We are now able to study the kinetics of CSRO in more detail. Both the time range in which CSRO takes place (about 4 decades) and the occurrence of the cross over effect (fig. 6.4) indicate that CSRO in $\text{Pd}_{40}\text{Ni}_{40}\text{P}_{20}$ is governed by a spectrum of activation energies, analogous

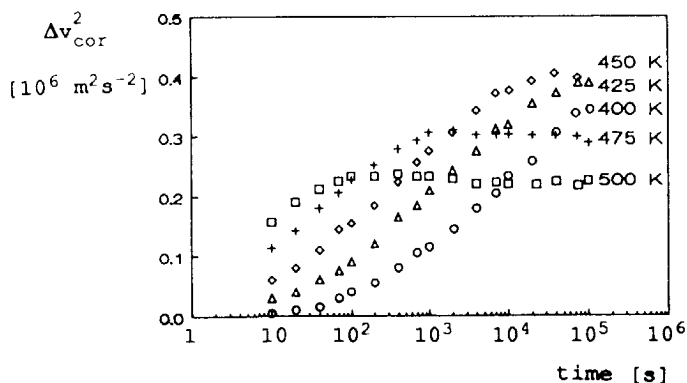


figure 6.13 Change in Young's modulus due to CSRO for the low temperature isotherms, plotted versus the annealing time.

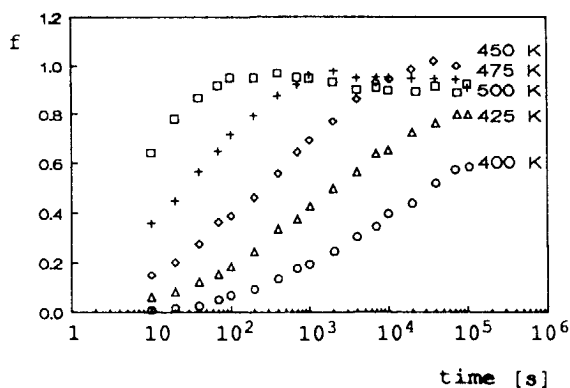


figure 6.14 Fractional change in Young's modulus due to CSRO, as a function of time at the temperatures indicated.

to what was found previously for $\text{Fe}_{40}\text{Ni}_{40}\text{B}_{20}$ [15]. In the analysis on $\text{Fe}_{40}\text{Ni}_{40}\text{B}_{20}$ van den Beukel used a box distribution for the activation energy spectrum (AES), which was a good approximation.

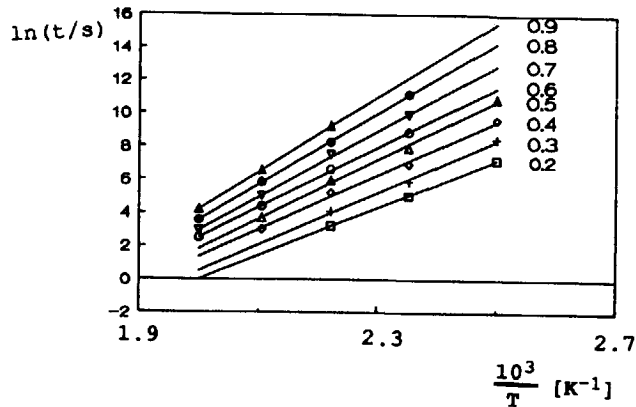


figure 6.15 $\ln(t)$ versus $1/T$ for horizontal intersections in figure 6.14 at the values of f indicated.

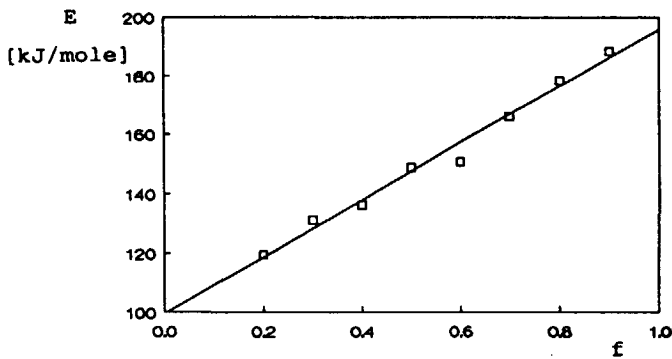


figure 6.16 The activation energy E versus the ordered fraction f , as derived from figure 6.15. The solid line is a least squares fit.

In figure 6.14 the CSRO part of the isotherms, presented in figure 6.13, has been replotted on the reduced scale $f = \Delta v^2 / \Delta v_{\text{CSRO}}^2$. The calculated value for Δv_{CSRO}^2 (eq. (6.10)) has been used. Horizontal intersections in figure 6.14 result in (T, t) data pairs for each fractional change of v^2 .

If a fractional change in v^2 is connected with a fraction of the AES, a plot of $\ln(t)$ versus $1/T$ for each f should yield a straight line [15], with slope $E(f)/R$ and intercept $-\ln(v_0)$, with v_0 a frequency factor. This has been done for f between 0.2 to 0.9 and the result is shown in figure 6.15. The activation energies and v_0 obtained from least squares fits are presented in table 6.2.

TABLE 6.2

Activation energies and frequency factors
derived from figure 6.15.

f	v_0	$E(f)$
	s^{-1}	kJ/mole
0.2	$3.1 \cdot 10^{12}$	119
0.3	$3.1 \cdot 10^{13}$	131
0.4	$4.6 \cdot 10^{13}$	136
0.5	$5.8 \cdot 10^{14}$	149
0.6	$4.7 \cdot 10^{14}$	151
0.7	$1.2 \cdot 10^{16}$	166
0.8	$1.2 \cdot 10^{17}$	178
0.9	$7.5 \cdot 10^{17}$	188

The slope of the lines increases with increasing f , which means that the activation energy increases when CSRO proceeds. This is demonstrated in figure 6.16 where the activation energy $E(f)$ is plotted versus f . $E(f)$ is linear with f , which implies that the AES is block shaped.

The activation energies lie between 100 and 195 kJ/mole. $E_{\text{max}} = 195 \text{ kJ/mole}$ is an unexpected result because it is 37 kJ/mole higher than the activation energy for TSRO. For $\text{Fe}_{40}\text{Ni}_{40}\text{B}_{20}$ the

maximum activation energy for CSRO about equals the activation energy for TSRO [5].

From table 6.2 it is also observed that v_0 increases from 10^{12} to 10^{18} s^{-1} . This observation agrees with the analysis of structural relaxation data in amorphous $Fe_{40}Ni_{40}B_{20}$ [5,15], where also an increase in v_0 has been found. Van den Beukel [5,15] suggested, after Berry [16], a relation between v_0 and E

$$v_0 = v'_0 \exp(\beta E/R) \quad (2.22)$$

where β and v'_0 are constants. If $\ln(v_0)$ is plotted versus $E(f)$ a straight line is observed, as shown in figure 6.17. A least squares fit results in

$$\beta = 1.5 \cdot 10^{-3} \text{ K}^{-1}$$

$$v'_0 = 1226 \text{ s}^{-1}.$$

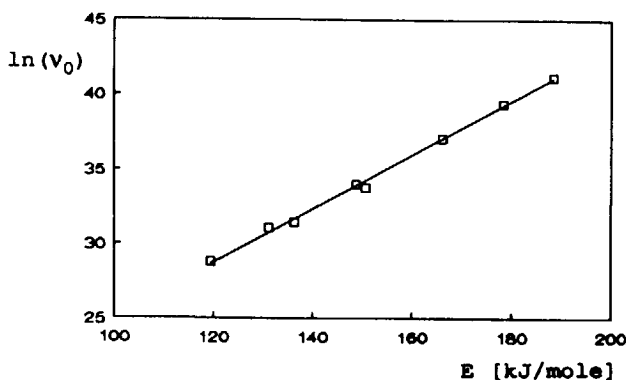


figure 6.17 The frequency factors v_0 versus the activation energy as determined from figure 6.15.

According to the Primak approximation (section 2.2.2), annealing during a time t_p at a temperature T_p results in ordering of a part of the spectrum with activation energies lower than E , where E follows from

$$E = \frac{RT_p}{(1-\beta T_p)} \ln(v'_0 t_p). \quad (2.23)$$

If the sample is subsequently annealed at a temperature T , the same activation energy will be reached after a time

$$t = \frac{1}{v_0} \exp\left(\frac{T_p(1-\beta T)}{T(1-\beta T_p)} \ln(v_0' t_p)\right). \quad (6.12)$$

In figure 6.4 isotherms were plotted for samples annealed at 480 K after preannealing at 450 K for several annealing times t_p . In figure 6.18 some of these isotherms are replotted. The arrows in this figure indicate the time, calculated with eq. (6.12), after which the minima are expected. The agreement between the calculated and the actual times is not perfect. However, using $1.6 \cdot 10^3 \text{ K}^{-1}$ for β , which is not an unreasonable value with respect to the accuracy, yields a perfect agreement between the calculated and the observed minima.

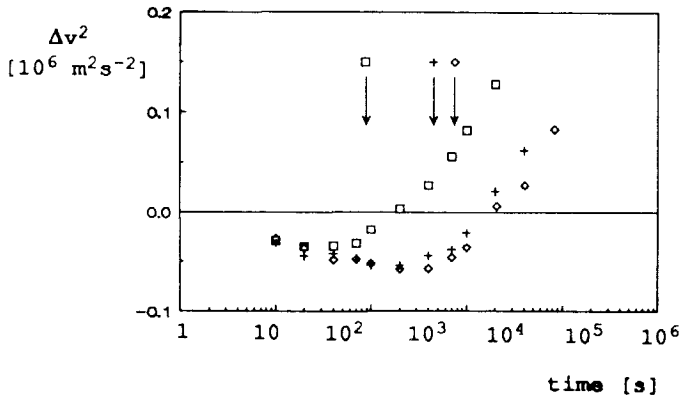


figure 6.18 Change in Young's modulus during isothermal annealing at 480 K after preannealing at 450 K during the time indicated. The arrows indicate the time, according to eq. (6.12), at which a minimum should be observed.

6.4 Discussion

In this chapter a description of structural relaxation in amorphous $\text{Pd}_{40}\text{Ni}_{40}\text{P}_{20}$ was given in terms of the mixed model. For the free volume contribution three simple equations for the description of annihilation

and production of free volume were tested. Since equilibrium is actually a state in which production and annihilation have the same rate, there can be no difference in the equation for $dc_f/dt > 0$ and $dc_f/dt < 0$. Therefore, one equation should be used to describe both processes. The most pronounced difference between the three equations was found in the description of the glass transition, which supports $dc_f/dt = -k_f c_f (c_f - c_{f,eq})$. Young's modulus measurements cannot discriminate between the three equations.

The CSRO part of the isotherms has been described by the AES model, assuming a box distribution for the spectrum of activation energies. The analysis yielded a consistent set of parameters.

In chapter 4 strong evidence has been found that structural relaxation in $\text{Fe}_{40}\text{Ni}_{40}\text{B}_{20}$ could not be described by CSRO and TSRO only. Before the onset of TSRO another irreversible contribution was found. The processes that evolve prior to CSRO are irreversible and so is part of the processes in the activation energy range between 170 and 250 kJ/mole, where the reversible processes occur.

An indication for irreversible processes preceding CSRO can be obtained by plotting the changes in the observed property after a preannealing treatment versus the activation energy, calculated with (2.23). For $\text{Fe}_{40}\text{Ni}_{40}\text{B}_{20}$ it was found that the reversible changes in a physical property like Young's modulus or the electrical resistivity starts at an activation energy of 170 kJ/mole, whereas relaxation in as quenched $\text{Fe}_{40}\text{Ni}_{40}\text{B}_{20}$ starts at 130 kJ/mole. Extrapolation of the data of figure 6.4 to $\Delta v^2 = 0$ yields a value for the time corresponding to an activation energy $E = 100$ kJ/mole (eq. (2.23)), which means that the spectra of the as quenched samples and preannealed samples start at the same activation energy.

However, this observation cannot completely exclude the possibility that the pre-TSRO part contains irreversible processes. The fictive temperature could be lower than reported in section 6.3.1, where in our fits the pre-TSRO part is completely ascribed to CSRO.

If this observation is characteristic for Pd-containing metallic glasses, it seems in agreement with positron annihilation experiments on a PdSi metallic glass [17]. In these experiments no decrease in positron lifetime was observed preceding the changes due to CSRO (compare with the behaviour of $\text{Fe}_{40}\text{Ni}_{40}\text{B}_{20}$ as described in chapter 4,

figure 4.2). This means that no irreversible processes preceded the reversible ones.

It was not possible to give a good description of the whole set of as quenched isotherms with a single set of parameters. The measurements indicated differences between the as quenched conditions of different samples. We accounted for these differences by adapting the initial free volume x_0 . We chose for x_0 instead of T_f because upon changing the quenching rate the changes in T_f are (partly) compensated by the free volume dependency of the ordering kinetics (chapter 5).

Since the kinetics of TSRO in $\text{Pd}_{40}\text{Ni}_{40}\text{P}_{20}$ is now known, the quenched-in amount of free volume can be calculated. Two linear cooling rates were chosen, 1000 K/s and 180 K/s. These cooling rates resulted in a reduced free volume of 0.0403 and 0.0385, respectively. This is roughly the range within which we had to vary x_0 in order to fit all the as quenched isotherms (section 6.3.1). The difference in quenching rate of more than a factor 5, necessary to cover the x_0 values resulting from the analysis, seems too large to be realistic. This indicates that both x_0 and T_f vary, and in our analysis we attributed the entire effect to a variation of x_0 . The actual differences in x_0 will therefore be smaller, leading to a smaller variation of the quenching rate.

The activation energy for flow defect annihilation and production (158 kJ/mole) is comparable to activation energies reported for other Pd containing metallic glasses. Cost *et al.* [18] reported an activation energy of 160 kJ/mole for a PdGe metallic glass, Taub and Spaepen [19] found an activation energy of 160 kJ/mole from their viscosity data on PdSi and van den Beukel [20] used 170 kJ/mole in an analysis of electrical resistivity data on the same metallic glass.

For CSRO a spectrum of frequency factors between 10^{12} and 10^{18} s^{-1} has been found which could be described by:

$$v_0 = v'_0 \exp(\beta E/R) \quad (2.22)$$

and v'_0 being 1226 s^{-1} . The frequency v'_0 depends on the concentration of diffusion defects [15]:

$$v_0' = v_d c_d. \quad (6.13)$$

When the initial concentration of diffusion defects ($c_d = \exp(-0.5/x_0)$, see chapter 5, and $x_0 = 0.0405$) is inserted in eq. (6.13), v_d is equal to $2.8 \cdot 10^8 \text{ s}^{-1}$. This value is considerably smaller than the Debye frequency ($\approx 10^{13} \text{ s}^{-1}$), but comparable to the observation in $\text{Fe}_{40}\text{Ni}_{40}\text{B}_{20}$, where a frequency factor of $5.1 \cdot 10^9 \text{ s}^{-1}$ was obtained.

The reported frequency factor C_0 for TSRO ($3.4 \cdot 10^{25} \text{ s}^{-1}$) is high in comparison with the expected Debye frequency v_d . In a similar way as done for v_0 , C_0 can be expressed as [15]:

$$C_0 = \beta' v_d \exp(\beta E_f / R) \quad (6.14)$$

where β' is a constant of order unity. Inserting the parameters C_0 , β and E_f obtained from the analysis, $v_d = 1.0 \cdot 10^{13} \text{ s}^{-1}$ which is a reasonable value.

Comins *et al.* [21] have tried to measure reversible changes in Young's modulus due to reversible relaxation in slowly cooled (1 K/s) amorphous $\text{Pd}_{40}\text{Ni}_{40}\text{P}_{20}$. Cycling experiments were performed between 493 K and 523 K, measuring Young's modulus *in situ*. No reversible changes were observed. However, according to our observations small reversible changes should have been found in these experiments. These changes should occur in the initial part of the isothermal annealing treatments and also during the non-isothermal part.

The as quenched velocity for their samples was about 4900 m/s and the density of the material was 9405 kgm^{-3} . This results in a modulus ($E = \rho v^2$) of about 228 GPa. This is about 2.5 times the as quenched Young's modulus for a rapidly quenched sample ($\pm 94 \text{ GPa}$) [10]. This difference cannot be explained in terms of the state of chemical order and free volume.

From the work of Comins *et al.* one can conclude that slowly cooled PdNiP has significantly different properties in comparison to the rapidly quenched material. Also the behaviour during structural relaxation is different from what is calculated with parameters for rapidly quenched $\text{Pd}_{40}\text{Ni}_{40}\text{P}_{20}$.

6.5 Conclusions

In this chapter experiments to study structural relaxation in amorphous $\text{Pd}_{40}\text{Ni}_{40}\text{P}_{20}$ have been reported. It was found that the stability of the metallic glass was sufficient to attain equilibrium for both CSRO and TSRO.

The data have been analysed in terms of the mixed model, previously used for structural relaxation in amorphous $\text{Fe}_{40}\text{Ni}_{40}\text{B}_{20}$. The kinetics of annihilation and production of flow defects (TSRO) can be described with the free volume model. Three equations were derived from which one, eq. (6.7), described the data rather well. The parameters obtained from least squares fits on the high temperature as quenched isotherms (table 6.1) gave reasonable values, which could be used to describe almost the whole set of measurements.

CSRO was described with the formalism of the AES model. The parameters (section 6.6) described the CSRO part well.

The mixed model and the corresponding parameters consistently describe both qualitatively and quantitatively the whole set of experimental data. However, due to the change in quenching conditions both T_f and x_0 must be varied somewhat to describe the whole set of data more precisely.

References

- 1 H.S. Chen, Mater. Sci. Eng. 23, 151 (1976).
- 2 A. J. Drehman and A.L. Greer, Acta Metall. 32, 323 (1984).
- 3 S.S. Tsao and F. Spaepen, Acta Metall. 33, 881 (1985).
- 4 C.A. Volkert and F. Spaepen, in Proc. 6th Int. Conf. on Rapidly Quenched Metals, Montreal, 1987, R.W. Cochrane and J.O. Ström-Olsen eds., Mat. Sci. Eng. 97, 449 (1988).
- 5 A. van den Beukel, Rapidly Quenched Materials, P.W. Lee and A.S. Carbonera eds., San Diego, 1986, p. 193.
- 6 G. Fulcher, J. Amer. Ceram. Soc. 6, 339 (1925).
- 7 H. Vogel, Z. Phys. 22, 645 (1921).

- 8 H.S. Chen, J.T. Krause and E. Coleman, J. Non-Cryst. Sol. 18, 157 (1975).
- 9 L. A. Davis, in Metallic Glasses, Proc. Sem. on Metallic Glasses, 1976, H.J. Leamy and J.J. Gilman eds., ASM, Ohio, 1978, p. 190.
- 10 L.A. Davis, C.-P. Chou, L.E. Tanner and R. Ray, Scripta Metall. 10, 937 (1976).
- 11 P.A. Duine, M.Sc. Thesis, Lab. of Mater. Sci., Delft University of Technology, 1990 (in Dutch).
- 12 P.A. Duine, private communication.
- 13 B. Albert, C. Hargitai, C. Kopasz, I. Nagy, S. Nemeth and T. Tarnoczi, in Proc. 7th Int. Conf. on Rapidly Quenched Materials, Stockholm, 1990, in press.
- 14 A. van den Beukel and J. Sietsma, Acta Metall. Mater. 38, 383 (1990).
- 15 A. van den Beukel, J. Non-Cryst. Sol. 83, 134 (1986).
- 16 B.S. Berry, Scripta Metall. 16, 1407 (1982).
- 17 S. Tanigawa, K. Shima. and T. Masumoto in Proc. 4th Int. Conf. on Rapidly Quenched Metals, Sendai, 1981, eds. T. Masumoto and K. Suzuki, Japan Inst. Met., Sendai, 1982., p. 501.
- 18 J.R. Cost, J.T. Stanley and B.J. Thijsse, Proc. 6th Int. Conf. on Rapidly Quenched Metals, Montreal, 1987, R.W. Cochrane and J.O. Ström-Olsen eds., Mat. Sci. Eng. 97, 523 (1988).
- 19 A.I. Taub and F. Spaepen, Acta Metall. 28, 1781 (1980).
- 20 A. van den Beukel, Scripta Metall. 20, 783 (1986).
- 21 J.D. Comins, J.E. Macdonald, M.R.J. Gibbs and G.A. Saunders, J. Phys. F: Met. Phys. 17, 19 (1987).

SUMMARY

Amorphous metals or metallic glasses are metallic alloys in the solid state without (translational) long range order. Metallic glasses can be produced by rapid quenching from the melt. When the obtained product is annealed at temperatures between 400 and 600 K atomic rearrangements in the amorphous state occur, which process is generally called structural relaxation. Structural relaxation must be clearly distinguished from crystallisation. This thesis deals with the kinetics of structural relaxation in amorphous $\text{Fe}_{40}\text{Ni}_{40}\text{B}_{20}$ and $\text{Pd}_{40}\text{Ni}_{40}\text{P}_{20}$.

In *chapter 2* several models for the kinetics of structural relaxation are described, of which the most important (for this thesis) is the mixed model, developed by van den Beukel and coworkers. In this mixed model structural relaxation is considered to consist of two sub-processes: Chemical Short Range Ordering (CSRO) and Topological Short Range Ordering (TSRO). For CSRO (chemical ordering of the local surroundings of an atom) the Activation Energy Spectrum model, introduced by Gibbs and coworkers, is used. The kinetics of TSRO (annihilation of defects) is described by the free volume model. The effectiveness of this mixed model is demonstrated by experimental data on the structural relaxation in amorphous $\text{Fe}_{40}\text{Ni}_{40}\text{B}_{20}$.

In *chapter 3* the set-ups for the various experimental techniques which were used for the measurements (Young's modulus, electrical resistivity, Differential Scanning Calorimetry (DSC) and anelastic strain) are described.

In previously presented data on structural relaxation in amorphous $\text{Fe}_{40}\text{Ni}_{40}\text{B}_{20}$ the transition from CSRO to TSRO was never directly visible. In *chapter 4* a successful attempt to observe this transition is described. In positron lifetime experiments a maximum is observed at the CSRO-TSRO transition. During TSRO the positron lifetime decreases, while in the CSRO part the lifetime increases after an initial decrease. These results indicate that the processes preceding TSRO (pre-TSRO) are probably not only CSRO but maybe involve another type of process.

This pre-TSRO part has been studied further with the help of electrical resistivity measurements on $\text{Fe}_{40}\text{Ni}_{40}\text{B}_{20}$. Measurements were performed at the annealing temperature, at room temperature and in liquid nitrogen. It was found that in the pre-TSRO part irreversible processes occur prior to and concurrent with the reversible CSRO. The

initial decrease in positron lifetime, as mentioned previously, may also be due to these irreversible processes.

In *chapter 5* the effect of defects on the kinetics of chemical ordering in, mainly, amorphous $\text{Fe}_{40}\text{Ni}_{40}\text{B}_{20}$ has been studied. It is generally assumed that these defects control both diffusion and viscous flow. Since CSRO is considered to be a diffusion process, one expects an effect of the concentration of defects on the CSRO kinetics. Young's modulus, electrical resistivity and anelastic strain measurements were performed to study this phenomenon. In the first two experiments temperature cycling was applied to study the reversible effect, for anelastic strain measurements stress cycling was performed. In the latter experiment the local order changes as a result of a mechanical stress, and the term *stress induced ordering*, is used to indicate this type of ordering.

All experiments clearly show that the ordering kinetics slows down when the concentration of defects decreases. However, the rate is not controlled by flow defects, the concentration of which (c_f) determines the viscosity of a metallic glass, but by diffusion defects, the concentration of which is nearly proportional to $\sqrt{c_f}$.

This result has been verified with the help of diffusion and viscosity data. In the free volume theory it is assumed that the diffusion coefficient D ($\propto c_f$) and the viscosity η ($\propto c_f^{-1}$) scale as the well known Stokes-Einstein relation for liquids: $\eta D = \text{constant}$ at constant temperature. However, from experimental data for η and D for $\text{Fe}_{40}\text{Ni}_{40}\text{B}_{20}$, we find that the Stokes-Einstein relation does not hold, but that $\eta D^2 = \text{constant}$, which is in agreement with the relation between diffusion defects and flow defects mentioned in the previous paragraph.

In the last chapter, *chapter 6*, structural relaxation in amorphous $\text{Pd}_{40}\text{Ni}_{40}\text{P}_{20}$ has been described in terms of the mixed model. Since $\text{Pd}_{40}\text{Ni}_{40}\text{P}_{20}$ is a rather stable glass, it is possible to bring this metallic glass in equilibrium for both CSRO and TSRO.

If this metallic glass can reach equilibrium for both CSRO and TSRO, it is expected that both exhibit reversible behaviour. This has been proven by performing cycling experiments.

Since no theoretical description for the kinetics of TSRO in the vicinity of equilibrium is available, three possible equations to describe the kinetics of TSRO are proposed, which were used to fit the Young's modulus data. The obtained parameters were used to describe the glass

transition, as observed in a DSC experiment. On the basis of the experimental data a choice for one of the three proposed equations could be made. The kinetics of CSRO is rather well described by the AES model.

Samenvatting

Een amorf metaal, ook wel metallisch glas genoemd, is een materiaal zonder lange afstands translatiesymmetrie. Dit betekent dat, in tegenstelling tot in een kristal, er geen periodieke rangschikking van atomen aanwezig is. Het ontbreken van de translatiesymmetrie is te zien in een röntgendiffractie opname, waar een continue intensiteitsverdeling wordt gevonden, terwijl een kristal scherpe pieken geeft.

Warmtebehandelingen van een amorf metaal tussen 400 en 600 K veroorzaken een verandering van een groot aantal fysische eigenschappen. Deze veranderingen worden toegeschreven aan atomaire herrangschikkingen in de amorse structuur en dit proces, niet te verwarren met kristallisatie, wordt in het algemeen aangeduid als *struktuurrelaxatie*.

In dit proefschrift staan experimenten beschreven die tot doel hebben inzicht te krijgen in de kinetiek van structuurrelaxatie. In deze experimenten worden veranderingen van fysische eigenschappen zoals elektrische weerstand, elasticiteitsmodulus en anelastische rek gemeten en de snelheid (kinetiek) van verandering wordt gerelateerd aan de snelheid van structuurrelaxatie.

In *hoofdstuk 1* wordt een korte inleiding gegeven over metallische glazen. In *hoofdstuk 2* wordt nader ingegaan op een aantal in de literatuur verschenen modellen welke de kinetiek van structuurrelaxatie beschrijven. Achtereenvolgens wordt het vrij volume model (sectie 2.2.1), het activeringsenergie spectrum (AES) model (sectie 2.2.2) en het gemengde model (sectie 2.2.3) behandeld. Het laatste model is opgesteld door van den Beukel en medewerkers en gaat er van uit dat er twee soorten processen tijdens structuurrelaxatie plaatsvinden.

Ten eerste is dat *Chemische korte afstands ordening* (CSRO), waarvan de kinetiek kan worden beschreven met het AES model. Deze processen brengen veranderingen teweeg in de chemische samenstelling van de directe omgeving van de atomen. Het tweede soort processen is de *Topologische korte afstands ordening* (TSRO); de kinetiek wordt beschreven door het vrij volume model. Tijdens TSRO neemt de dichtheid van het materiaal toe met het verdwijnen van het extra ingevroren volume, het vrij volume. TSRO is daarom te vergelijken met het verdwijnen van overmaat vacatures in een snel afgekoeld kristallijn materiaal.

De bruikbaarheid van het gemengde model is aangetoond aan de hand van structuurrelaxatie in amorf $\text{Fe}_{40}\text{Ni}_{40}\text{B}_{20}$. Het is mogelijk om met een set parameters de kinetiek van structuurrelaxatie te beschrijven. In het laatste deel van hoofdstuk 2 wordt uiteengezet dat structuurrelaxatie niet uitsluitend met TSRO en CSRO te beschrijven is maar dat er een derde, niet reversibel proces moet worden aangenomen welke ongeveer gelijk met het reversibele CSRO plaatsvindt.

In *hoofdstuk 3* worden de verschillende opstellingen beschreven die gebruikt zijn tijdens het onderzoek (Elasticiteitsmodulus, elektrische weerstand, calorimetrie (DSC) en anelastische rek).

In eerder gedane structuurrelaxatiemetingen in amorf $\text{Fe}_{40}\text{Ni}_{40}\text{B}_{20}$ werd nooit een duidelijke overgang van CSRO naar TSRO waargenomen. In een poging deze overgang wel waar te nemen zijn metingen verricht aan de levensduur van positronen. De resultaten zijn vermeld in het eerste deel van *hoofdstuk 4*. Gebleken is dat bij de overgang CSRO-TSRO een maximum wordt waargenomen. TSRO heeft een daling van de levensduur tot gevolg, terwijl in het pre-TSRO gebied eerst een daling en daarna een stijging van de levensduur is gemeten.

Het pre-TSRO gebied is onderwerp van studie in de rest van hoofdstuk 4. Hiervoor werd de verandering van de elektrische weerstand gemeten, zowel op de gloeitemperatuur als op kamertemperatuur en in vloeibare stikstof. Er is gevonden dat het pre-TSRO gebied bestaat uit reversibele en irreversibele processen. De reversibele processen vormen de eerder genoemde CSRO, de aard van de irreversibele processen is niet bekend. Er wordt verder geconcludeerd dat de initiële daling in de positron levensduur wordt veroorzaakt door de irreversibele processen.

In *hoofdstuk 5* wordt de invloed van het aanwezige vrij volume op de reversibele ordening beschreven. Aangenomen wordt dat deze reversibele ordening diffusie gestuurd is en dat het extra volume dat in het materiaal aanwezig is hiervoor gebruikt wordt. Om de invloed van dit vrij volume op de ordeningskinetiek te bestuderen zijn temperatuurwisselings experimenten of anelastische rek experimenten gedaan. Bij de temperatuurwisselings experimenten werd gekeken hoeveel langzamer de reversibele component van een fysische eigenschap verandert tijdens het gloeien op een bepaalde temperatuur t.o.v. een eerdere gloeibehandeling op die temperatuur. Tussen deze twee gloeibehandelingen werd dan een gloeibehandeling op een andere, hogere temperatuur uitgevoerd die ervoor zorgde dat het vrij volume in het

materiaal afnam. Gebleken is dat de ordeningskinetiek ook inderdaad afneemt naarmate het vrij volume afneemt.

Nu wordt er in het vrij volume model aangenomen dat zowel diffusie als vloeï gecontroleerd worden door zogenaamde vloeidefecten. De concentratie van deze vloeidefecten wordt bepaald door de hoeveelheid vrij volume. De concentratie vloeidefecten c_f als functie van de tijd tijdens een warmtebehandeling is te berekenen met het vrij volume model. Indien diffusie door vloeidefecten zou worden gecontroleerd, dan zou de gemeten vertraging evenredig moeten zijn met c_f . Uit de experimenten blijkt echter dat de ordeningssnelheid niet evenredig is met c_f maar met $\sqrt{c_f}$.

Dit resultaat is getest met behulp van diffusie- en viscositeits gegevens. In het vrij volume model wordt er van uitgegaan dat de diffusiecoëfficiënt D ($\propto c_f$) en viscositeit η ($\propto c_f^{-1}$) bij constante temperatuur gehoorzamen aan de zogenaamde Stokes-Einstein relatie, $\eta D = \text{constant}$. Als echter deze relatie wordt getest met behulp van viscositeit en diffusie gegevens, dan blijkt dat deze niet te voldoen aan deze relatie, maar wel aan $\eta D^2 = \text{constant}$. Dit is in overeenstemming met de eerder gevonden relatie tussen de concentratie vloeidefecten en de ordeningssnelheid.

In *hoofdstuk 6*, tenslotte, wordt de kinetiek van structuurrelaxatie in amorf $\text{Pd}_{40}\text{Ni}_{40}\text{P}_{20}$ besproken aan de hand van elasticiteitsmodulus metingen. Dit metallische glas is stabielier dan het eerder gebruikte $\text{Fe}_{40}\text{Ni}_{40}\text{B}_{20}$, waardoor het mogelijk is om het in evenwicht te brengen tijdens warmtebehandelingen. Dit betekent dat zowel CSRO als TSRO in evenwicht kunnen worden gebracht.

De vergelijking die de verandering van het vrij volume beschrijft tijdens een gloeibehandeling voorzagt niet in het feit dat het vrij volume naar evenwicht gaat. In dit proefschrift worden drie vergelijkingen voorgesteld die wel rekening houden met het evenwicht. Deze vergelijkingen worden gefit aan de experimentele data, resulterende in een aantal waarden voor de fitparameters. Deze waarden voor de fitparameters zijn gebruikt om de glasovergang, zoals deze wordt waargenomen tijdens een DSC experiment, te beschrijven. Hieruit kon worden geconcludeerd dat de vergelijking $dc_f/dt = -k_r c_f (c_f - c_{f,eq})$ de gehele dataset het beste beschrijft. Voor de CSRO bijdrage werd het AES model gebruikt om de kinetiek te beschrijven.

SAMENVATTING

Door middel van temperatuurwisselingsexperimenten is de reversibiliteit van zowel CSRO als TSRO getest.

CURRICULUM VITAE

De schrijver van dit proefschrift werd geboren op 4 april 1963 te Goor. De middelbare school, ongedeeld Atheneum, werd gevolgd aan het Twickel College te Hengelo, waar in 1981 het diploma werd gehaald. Na een jaar te hebben gestudeerd aan de HTS/SVL te Hengelo (analisten opleiding) werd in 1982 begonnen met een studie Scheikunde aan de Rijksuniversiteit Utrecht. Het afstudeeronderzoek werd gedaan in de vakgroep Anorganische Chemie, sectie Katalyse van Prof. ir. J.W. Geus. Onderzoek werd verricht naar de activiteit en selectiviteit van FeCu op SiO_2 katalysatoren in de Fischer-Tropsch synthese. In juni 1986 werd het doctoraal diploma gehaald.

Van Augustus 1986 tot November 1990 was de schrijver in dienst van de Technische Universiteit Delft, in de groep Fysische Materiaalkunde. De resultaten van het aldaar verrichtte onderzoek staan beschreven in dit proefschrift.

DANKWOORD

Graag zou ik van de gelegenheid gebruik willen maken om een aantal mensen met name te noemen die hebben bijgedragen tot het tot stand komen van dit proefschrift.

Allereerst ben ik mijn promotor prof. dr. ir. A. van den Beukel zeer erkentelijk voor de mogelijkheid die hij mij gegeven heeft om het onderzoek beschreven in dit proefschrift uit te voeren. Zijn brede kennis en enthousiaste benadering van het onderzoek en de verkregen resultaten hebben altijd stimulerend gewerkt.

Door zijn "dagelijkse" begeleiding heeft Jilt Sietsma een niet onbelangrijke bijdrage geleverd. Diskussies naar aanleiding van recente resultaten leidden meestal tot op zijn minst ideeën voor verder onderzoek of tot mogelijke verklaringen van de resultaten.

Erik Huizer wil ik bedanken voor het inwijden op het gebied van metallische glazen en het inwerken op de apparatuur.

Johan de Vries wil ik bedanken voor het uitvoeren van de positron levensduur metingen.

Onderzoek doen is tegenwoordig bijna niet meer mogelijk zonder goede technische ondersteuning. Ab de Koster en de heer H. Weerheijm waren in staat om snel eventuele problemen op te lossen en gaven vaak suggesties om opstellingen te verbeteren.

De heren P. de Ruiter en H. Kleinjan wil ik bedanken voor de bereidheid de $\text{Pd}_{40}\text{Ni}_{40}\text{P}_{20}$ legering te flitsgieten.

Mijn (ex)- collega's en (ex)- studenten van de vakgroep FCM wil ik bedanken voor de prettige werksfeer en stimulerende discussies. Het was bijzonder aangenaam dat deze discussies soms werden gevoerd in minder wetenschappelijke locaties in de stad.

Tevens wil ik ook het overige personeel van het laboratorium voor Materiaalkunde bedanken voor de prettige jaren die ik hier mocht hebben.

Mijn ouders wil ik bedanken voor hun belangstelling en steun tijdens mijn studie en promotie. De familie Slag dank ik voor de gastvrijheid tijdens mijn studie in Utrecht. Tenslotte wil ik jouw Anja bedanken voor je begrip en geduld.